Real-time studies of coupled molecular switches in photoresponsive materials

Dissertation

zur Erlangung des akademischen Grades

doctor rerum naturalium
(Dr. rer. nat.)
im Fach Physik
Spezialisierung Experimentalphysik

eingereicht an der
Mathematisch-Naturwissenschaftlichen Fakultät
der Humboldt-Universität zu Berlin

von
Herrn M.Sc. Christopher Weber

Präsident der Humboldt-Universität zu Berlin:
Prof. Dr. Jan-Hendrik Olbertz

Dekan der Mathematisch-Naturwissenschaftlichen Fakultät:
Prof. Dr. Elmar Kulke

Gutachter/innen:

1. *Prof. Dr. Stefan Kowarik*
2. *Prof. Dr. Petra Tegeder*
3. *Priv.-Doz. Dr. Andreas Opitz*

Tag der mündlichen Prüfung: 11.12.2015

Abstract

Synthetic molecular switches, such as azobenzenes, diarylethenes, fulgides, stilbenes or spiropyrans, have been intensively investigated in recent times because of their possible use in data storage, self-healing materials, molecular electronics, energy and information storage and optomechanics. One of the biggest challenges in the research field of molecular switches is the translation of the photoresponse of isolated molecules into a controlled photoresponse of well-defined supramolecular systems, such as organic thin films or functional nanostructures.
The main focus of this thesis lies on the photoisomerization of multi-azobenzene compounds in different structural environments. Incorporation of molecular switches, for example azobenzene, into supramolecular assemblies can lead to emergent phenomena like cooperative switching behavior. Cooperative switching means that the energetic landscape and thus also the isomerization kinetics of a single molecular switch is influenced by the isomeric state of adjacent switches. However, it has proven difficult to establish cooperative switching behavior or even switching functionality at all in ordered ensembles of molecular switches on surfaces due to steric hindrance or delocalisation of excited states. Therefore, understanding the prerequisites for switching functionality and cooperative behavior of molecular switches in supramolecular assemblies is a crucial step towards the development of devices that make use of concerted motion of molecular switches. In this thesis, we[1] show that multi-azobenzene compounds with alkyl side-chains can be used as building blocks for a large variety of photoresponsive supramolecular structures. Both for the molecular packing structure and the photoresponse of the material, the interaction between the alkyl side-chains in particular plays a crucial role.

First, layered thin films of azobenzene main chain polymers with alkyl side chains are investigated. Using atomic force microscopy (AFM) and X-ray scattering, we find that the azobenzene polymers form molecular zippers. We use a novel combination of real-time optical spectroscopy and real-time X-ray scattering to monitor both the photoisomerization process of the azobenzene chromophores and the structural photoresponse of the molecular crystals. Our measurements indicate that photoisomerization of about 20 % of the azobenzenes triggers a structural transition of the alkyl side chains from a crystalline (closed zippers) to a disordered state (open zippers).

The second multi-azobenzene compound we study is an azobenzene trimer with

[1] Although this doctoral thesis is written by a single author and all the experiments and analyses presented here were performed by this author, the chosen form of writing employs the use of first person plural throughout the work as it is common practice in scientific publications.

alkyl side chains. These smaller molecules form highly ordered molecular crystals on silicon surfaces, as found with AFM and X-ray scattering techniques. By monitoring the photoresponse of the system with real-time optical spectroscopy and real-time X-ray scattering, we find that the crystal structure can be switched off and on with light partially reversible via a cascadic process.

After that, we study the isomerization kinetics of azobenzene oligomers that form nanofibers in solution as found with AFM. Interestingly, we find that the photoisomerization becomes slower at higher temperatures which clearly indicates an unexpected and non-Arrhenius-type thermal behavior. Also, we find that the photoisomerization rate depends on the fraction of switched azobenzenes in the nanofibers, which shows that the azobenzenes in the nanofibers switch cooperatively.

The results of this thesis demonstrate the great potential of multi-azobenzene compounds with alkyl side chains for the construction of structurally well-defined photoresponsive materials. The results of this thesis yield unprecedented insight into the relation between the photoisomerization of isolated azobenzenes and the photoresponse of supramolecular systems, which will ultimately help to build novel and optimized stimuli-responsive materials.

Kurzfassung

Künstliche molekulare Schalter, wie beispielsweise Azobenzole, Diarylethene, Fulgide, Stilbene oder Spiropyrane wurden in den letzten Jahren intensiv erforscht, da sie zur Datenspeicherung, in selbstheilenden Materialien, molekularer Elektronik, Energiespeichern und mikromechanischen Anwendungen eingesetzt werden können. Eine der größten Herausforderungen im Forschungsfeld der molekularen Schalter ist die Frage, wie die Photoreaktion isolierter Moleküle in eine kontrollierte Photoreaktion wohldefinierter supramolekularer Systeme, wie z.B. organischer Dünnfilme oder 3D Nanostrukturen, übersetzt werden kann. Die Integration molekularer Schalter, beispielsweise von Azobenzolen, in supramolekulare Anordnungen kann zu emergenten Phänomenen wie kooperativem Schaltverhalten führen. Kooperatives Schalten bedeutet, dass die energetische Landschaft und daher auch die Isomerisationskinetik eines einzelnen molekularen Schalters von den isomerischen Zuständen benachbarter Schalter beeinflusst wird. Kooperatives Schaltverhalten, oder überhaupt Schaltbarkeit in geordneten Ensembles molekularer Schalter auf Oberflächen bewusst zu erzeugen hat sich allerdings aufgrund von sterischer Behinderung oder Delokalisierung angeregter Zustände als schwierig herausgestellt. Deshalb wäre ein besseres Verständnis der Voraussetzungen für Schaltbarkeit und kooperatives Verhalten molekularer Schalter in supramolekularen Systemen ein großer Schritt in Hinblick auf die Entwicklung von Bauelementen, die auf der gemeinsamen Bewegung molekularer Schalter basieren. In der vorliegenden Arbeit wird gezeigt, dass Multi-Azobenzolverbindungen mit Alkyl-Seitenketten dazu benutzt werden können, eine vielfältige Auswahl von photoreaktiven supramolekularen Strukturen herzustellen. Sowohl für die molekulare Struktur als auch für den Schaltvorgang kommt insbesondere der Wechselwirkung der Seitenketten miteinander eine entscheidende Rolle zu. Der erste Teil dieser Arbeit behandelt dünne Schichtsysteme aus Azobenzol Hauptkettenpolymeren mit Alkyl-Seitenketten. Mittels AFM und Röntgenstreuung findet man, dass die Azobenzolpolymere molekulare Reißverschlüsse bilden. Es wird eine neuartige Kombination aus optischer Spektroskopie und Röntgenstreuung in Echtzeit eingesetzt, um den Photoisomerisationsprozess der Azobenzole und die strukturelle Photoreaktion der Molekülkristalle zu verfolgen. Unsere Messungen zeigen, dass die Photoisomerisation von ungefähr 20 % der Azobenzole im Film einen strukturellen Übergang der Alkyl-Seitenketten von einer kristallinen (geschlossene Reißverschlüsse) hin zu einer ungeordneten Phase (geöffnete Reißverschlüsse) bewirkt.

Die zweite Multi-Azobenzolverbindung, die in der vorliegenden Arbeit untersucht wird, ist ein mit Alkyl-Seitenketten ausgestattetes Azobenzol-Trimer. Die-

se kleineren Moleküle bilden hochgeordnete molekulare Kristalle auf Siliziumoberflächen, wie mit AFM und Röntgenstreuung herausgefunden wurde. Durch das Verfolgen der Photoreaktion des Systems mit optischer Spektroskopie und Röntgenstreuung in Echtzeit findet man heraus, dass die Kristallstruktur im Rahmen einer kaskadenartigen Reaktion teilweise reversibel mit Licht ein- und ausgeschaltet werden kann.

Im Anschluss daran wird die Isomerisationskinetik von Oligomeren mit Azobenzol-Hauptketten studiert, die in Lösung Nanofasern bilden. Es ist ein interessantes Resultat, dass die Photoisomerisierung mit zunehmender Temperatur langsamer wird, was auf ein unerwartetes und nicht Arrhenius-typisches thermisches Verhalten schließen lässt. Ein weiteres Ergebnis ist, dass die Photoisomerisierungsrate in Nanofasern von der Konzentration geschalteter Azobenzol abhängt, was zeigt, dass die Azobenzole in den Nanofasern kooperativ schalten.

Die Ergebnisse dieser Arbeit zeigen das große Potential von Multi-Azobenzolverbindungen mit Alkyl-Seitenketten für die Konstruktion photoreaktiver Materialien mit wohldefinierter Struktur auf. Die in dieser Arbeit erzielten Resultate gewähren neue Einblicke in das Verhältnis zwischen der Photoisomerisierung einzelner Azobenzole und der Photoreaktion supramolekularer Systeme, was dabei helfen wird, neuartige und optimierte stimulireaktive Materialien zu entwickeln.

Contents

1 From molecular switches to molecular machines

In 1959, physicist Richard Feynman who later won the Nobel Prize gave a lecture at a meeting of the American Physical Society, titled as "There's Plenty of Room at the Bottom". [1] In this lecture, he presented his concept of a future that is characterized by the ubiquity of very small machines. In Feynman's vision, these molecular machines were able to perform chemical synthesis by mechanical manipulation. They could also act as surgical robots within our own body. In particular, he was interested in the possibility to enhance the performance of computers by increasing the density of computer circuitry. This thought was later brought to fame by Gordon E. Moore, co-founder of the Intel Corporation, who in 1965 predicted a doubling of components per integrated circuit every year. Of course, there is an ultimate limit to Moore's law. Eventually the transistors will reach the limits of miniaturization when they reach the size of single atoms, beyond which lies the even stranger world of quantum physics. Feynman knew that the new world at the nanoscale he envisioned would be governed by different physical laws than our macroscopic world. While the influence of gravity would become negligible, other forces, such as Van der Waals attraction would play a dominating role in many processes. To study these atomic and molecular machines, completely new microscopes would be needed with a much better resolution than the scanning electron microscopes that were available then.

Today, many of Feynman's original ideas have been realized. Very important in that context were the invention of the scanning tunneling microscope in 1981 and the invention of the atomic force microscope in 1986, which made it possible to image and manipulate individual atoms and molecules. Now, about thirty years later, there is a very broad research field called nanotechnology that deals with the manipulation of atomic and molecular matter.

In the last decade, a lot of efforts have been made towards the development of synthetic molecular machines. Molecular switches, *i.e.* molecules that change their structural, electronic and optical properties in response to external stimuli such

as light, heat or electric current, can be used as building blocks for molecular machines. [2,3] The human eye is a prominent example for the use of molecular switches by nature. The transduction of visual information from the eye into the brain is controlled by the light-induced *cis-trans* isomerization of the molecular switch retinal. Synthetic molecular switches, such as azobenzene, diarylethenes, fulgides, stilbenes or spiropyrans, have been intensively investigated in recent times because of their possible use in data storage [4], self-healing materials [5], molecular electronics [6], energy storage [7] and micromechanics [8–12]. In contrast to other stimuli like temperature, electric fields or solution composition, light possesses many advantages as a primary energy source, in particular its fast, clean, precise and remotely controlled application. [13]

Probably the most extensively studied molecular switch is azobenzene. [14] Azobenzene was first described in 1834 by Eilhard Mitscherlich and synthesized by Alfred Nobel in 1856. Because diazenes like azobenzenes are strong optical absorbers, they are commonly used as dyes for industrial purposes. The photochromic nature of azobenzene has been known for many decades [15]. Azobenzene derivatives can be switched reversibly between the thermodynamically stable *E*-configuration and the metastable *Z*-configuration with UV light or visible light, respectively. Integrating molecular switches into well-defined hierarchical assemblies such as liquid-crystal networks, 2D lattices or linear fiber structures allows one to amplify nanoscale molecular motions into macroscopic changes of material properties. [16–19]

The interaction between chromophores is important, in particular for systems where a high molecular packing density is crucial for device performance. [20, 21] In information or energy storage, the storage capacity is ultimately limited by the density of storing units. Also, in optomechanical applications, *e.g.*, for artificial muscles, a higher density of switches corresponds to larger potential forces generated by a single muscle strand. In these systems, steric interaction and excitonic coupling between adjacent molecular switches can lead to cooperative switching, that is, the chromophores do not switch independently of each other. [22,23] Whereas too strong steric, excitonic and electronic interactions can suppress the photoresponse in some cases [24, 25], positive cooperativity can be used to optimize the photoresponse of materials, *e.g.*, by supporting switching cascades. [26–29] In biological systems, cooperativity is commonly used to accelerate specific processes and to increase or amplify the outcome of reactions. [30] In synthetic systems, possible applications range from sensing devices where cooperativity could be used to amplify detection signals and thus to increase the sensitivity, to artificial muscles, where cooperativity could accelerate the contraction or expansion process. However, there are only very

few reports of cooperative switching, yet. [29, 31] One problem faced so far is that it has proven difficult to integrate molecular switches into hierarchical structures with improved functionality because it is hard to find switches that can be switched reliably in environments with strong intermolecular coupling.
Azobenzene derivatives in particular are promising candidates to be used as building blocks for cooperatively switching multicomponent molecular systems. This is because the isomerization from the stretched out E-isomer to the compact Z-isomer is accompanied by significant changes of geometry and dipole moment, which makes it more likely that neighboring chromophores will interact during the isomerization through steric or electronic coupling.
In this thesis, we use combined real-time optical spectroscopy and real-time X-ray diffraction to monitor the isomerization of azobenzene in the solid state and to study the dependence of isomerization kinetics on the microenviroment. In particular, we study the influence of alkyl side-chains on the switching process of azobenzene polymers, oligomers and trimers in organic thin films and in nanostructures. The combination of these complementary techniques is especially powerful for this purpose because X-ray diffraction is sensitive to optically induced structural changes, whereas optical spectroscopy allows one to follow the conversion of one azobenzene isomer into the other. The comparison between X-ray and optical data makes it possible to unravel the relation between light-induced structural changes and the isomerization process, bridging the gap between macroscopic effects and their molecular origin.
In summary, this thesis addresses the following questions about molecular switches:

- How is the photoresponse of supramolecular systems and materials related to the photoresponse of single isolated molecular switches?
- In which way is positive cooperativity in ensembles of molecular switches related to the supramolecular structure?

In particular, three azobenzene based systems have been investigated in full detail in this work: (i) Thin multilayer films of azobenzene main chain polymers with alkyl side-chains on mica (ii) crystallites of azobenzene-trimers on silicon, and (iii) nanoaggregates of azobenzene oligomers with alkyl side-chains on silicon. In the first system, the $E \rightarrow Z$ isomerization of azobenzene triggers a structural transition of the alkyl side-chains from a crystalline to a disordered phase. In the second system, the photoisomerization of azobenzene trimers triggers a structural phase transition of a highly crystalline material and the photoisomerization proceeds through the crystal in a cascadic scenario. And in the third system, the isomerization kinetics of azobenzene chromophores is controlled by the isomeric state of other azobenzenes in

their microenvironment, which is characteristic for cooperative switching behavior.

The results of this thesis are of fundamental interest for the development of nanomaterials based on molecular switches in a solid state environment.

Organization of this thesis

This thesis is organized as follows: after the introduction, we give an overview over the materials that are investigated in this thesis in chapter 2. First, a short summary of the properties of organic compounds and molecular switches in particular is given, followed by a more detailed description of the molecular switch azobenzene.

Chapter 3 deals with the experimental techniques that are used in this thesis, namely X-ray scattering, differential reflectance spectroscopy and atomic force microscopy.

The experimental results part of this thesis starts with chapter 4, where we study the photoresponse of azobenzene main chain polymers with alkyl side-chains.

Next, we study the switching process of azobenzene trimers in highly crystalline thin films in chapter 5.

In chapter 6, we show that azobenzene oligomers with alkyl side-chains exhibit cooperative switching behavior when integrated into nanofibers.

After that, a summary (chapter 7) of the previous chapters is given in which the main results of this thesis are presented in a condensed form .

The results of chapters 4,5 and 6 and parts of the appendix have been published or are to be published soon (see publication list).

2 Materials

In this chapter, we introduce the molecular systems that are investigated in this thesis. First, an overview over the research field of molecular switches and azobenzene in particular is given, where the respective topics of current interest are presented, alongside a range of open questions. After that, a short overview of the substrates that have been used in this thesis is given.

Organic compounds and materials form the basis of life. In fact, the division of matter into organic and inorganic compounds goes back to the alchemistic theory of vitalism. For many centuries, alchemists believed that living organisms in contrast to inorganic matter possessed a so called "life-force" (*vis vitalis*). Nowadays, this division of matter into organic and inorganic compounds is somewhat arbitrary, because there is no clear definition of organic matter anymore. Usually, by speaking of organic matter, one means molecules with many carbon atoms and/or carbon-hydrogen bonds.
It is no coincidence that carbon based materials form the basis of life. Having four valence bonds allows a carbon atom to form several different bonding patterns, single, double, triple bonds and conjugated systems with delocalized electrons. As a result, organic compounds are extremely diverse and flexible in their application. Using nature as a model, a lot of efforts have been made towards the synthesis of synthetic organic materials during the last century. Today, organic chemistry, polymer chemistry and medicinal chemistry are among the biggest industries in all highly developed countries. Polymers make up about the largest revenue segment of the chemical industry. Typical markets for polymeric materials (mainly plastics and fibers) are packaging, construction, clothing, transportation, toys etc. The most common polymer product is polyethylene (PE), which is a mixture of long hydrocarbon chains (see Figure 2.1).

In more recent times, a new class of functional polymers has been developed. Functional polymers combine the advantages of polymeric materials such as their toughness, viscoelasticity, ease of processing and low cost with advanced optical or electronic properties. Functional polymers range from biomimetic materials and

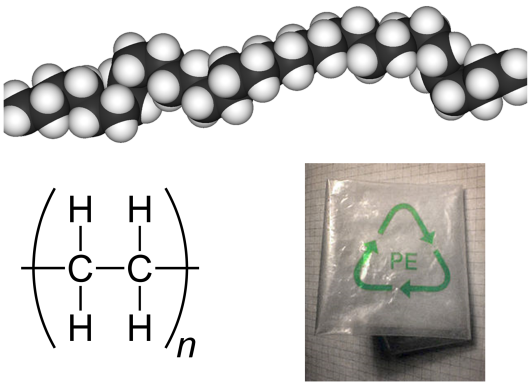

Figure 2.1: Chemical structure of polyethylene (PE) (taken with permission from ref. [32])

semiconducting polymers up to responsive polymers, whose optical and electronic properties can be controlled via external stimuli. [33] Among the devices that have been fabricated using functional semiconducting polymers are field-effect transistors (FETs) [34], light-emitting diodes (LEDs) [35, 36] and solar-cells [37]. Stimuli-responsive polymers, also known as smart polymers, are already used industrially for the production of hydrogels, biodegradable packaging and in biomedical engineering. One fascinating ability of smart polymers is their strong response, that is already small stimuli can trigger macroscopic changes of materials. The reason for this lies in the inherent nature of polymers, because the strength of the response of a polymer to an external stimulus is the composite of the response of the individual monomers. Stimuli-responsive polymers can be synthesized by incorporating so called *molecular switches* in the side chains or the main chain of a polymer.

2.1 Molecular switches

Molecular switches are molecules that have two or more (meta-)stable states (isomers) with different physical properties. [2, 13] The isomers can have a different molecular structure, a different color, dipole-moment or different electronic properties. The transition between the different isomers can be induced via external stimuli, such as light, heat or electric current. In the case of photochromism, the isomerization can be induced by light and changes the color of the material. In terms of their geometric reconfiguration during isomerization two classes of photochromic switches can be distinguished: (i) Switches that undergo a *trans/cis* isomerization, *e.g.*, stilbenes and azobenzenes, and (ii) switches undergoing a ring opening/closure reaction, *e.g.*, Diarylethenes and Fulgides. Another distinction can be made between

switches that are thermally reversible (T-type) and switches that have two thermodynamically stable isomers, that is, they can not themally revert to the initial isomer even at elevated temperatures (P-type). [38]

Due to its easy handling and wide distribution in the chemical industry, in particular in dyes, azobenzene has become probably the most extensively investigated molecular switch. Figure 2.2 shows the chemical structure and a sketch of the potential energetic diagram of azobenzene. Azobenzene consists of two phenyl rings that are connected via a double bonded nitrogen bridge (azo-group). The photochromic nature of azobenzene has already been noticed almost a century ago, although the understanding of the photochemical background lacked behind. [15, 39]

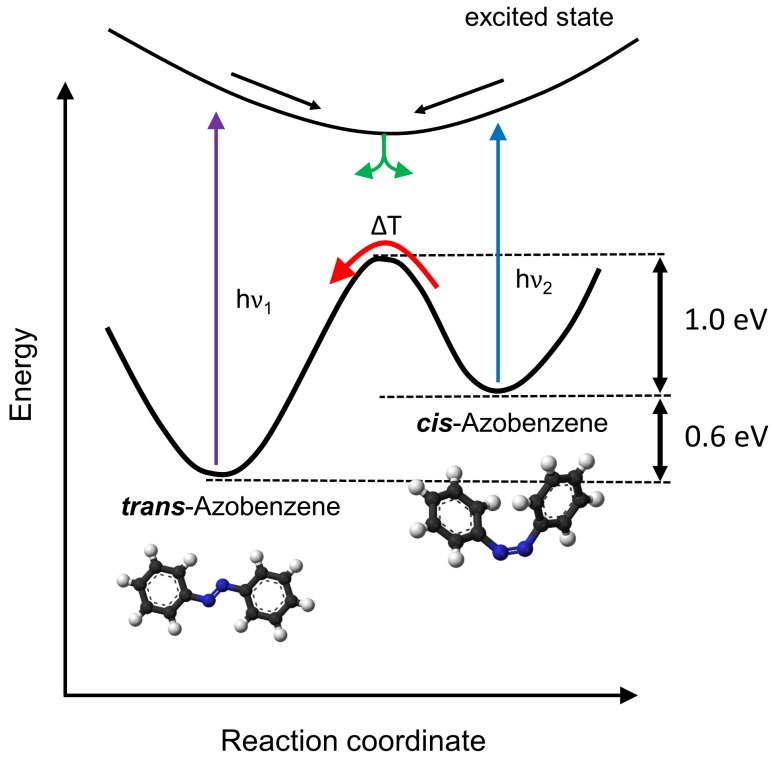

Figure 2.2: Sketch of the energy surface of the ground state and a schematic excited state of azobenzene.

Azobenzene in its thermodynamically stable *trans*-configuration is a planar molecule with a vanishing static dipole moment. *Trans*-Azobenzene has a weak symmetry forbidden absorption band (ε_{max} = 405 l mol^{-1} cm^{-1} as measured in n-hexane) in the visible region between 2.5 eV and 3.1 eV, corresponding to a $n \rightarrow \pi^*$ excitation. Here, the $n \rightarrow \pi^*$ excitation denotes an electron transition from a non-bonding molecular orbital located at the azo group to a more delocalized π^*-orbital.

In the UV-region at around 3.9 eV, *trans*-azobenzene has a strong absorption band

(ε_{max} = 23000 l mol^{-1} cm^{-1} in n-hexane) that corresponds to a $\pi \rightarrow \pi^*$ excitation. Another $\pi \rightarrow \pi^*$ absorption band is located at around 5.4 eV (ε_{max} = 14400 l mol^{-1} cm^{-1} in n-hexane). See also Figure 2.3 for the absorption spectrum of the two azobenzene isomers.

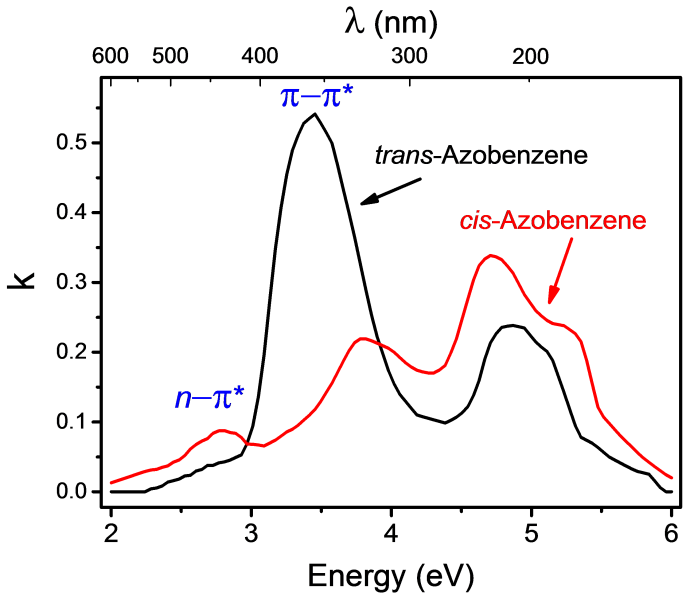

Figure 2.3: Typical absorption spectra of *trans*- and *cis*-azobenzene.

The *trans*-isomer of azobenzene can be switched to the thermodynamically metastable *cis*-isomer via optical excitation. Note that in the case of (multi-)azobenzene compounds with a more complex structure, where the usage of the terms *trans* and *cis* might be misleading, the *trans* and *cis*-isomers are usually denoted as *E*- and *Z*-isomers, following a more general nomenclature.

- *E* ('*Entgegen*') - The higher priority substituents (*e.g.*, the two benzene rings) are on different sides of the double bond (*e.g.*, the azo-group).

- *Z* ('*Zusammen*') - The higher priority substituents are on the same side of the double bond.

The rules for determining priorities are known as Cahn-Ingold-Prelog (CIP) rules. Figure 2.2 illustrates the photoisomerization process in an energetic diagram. Starting from the S_0 ground state of the *trans*-isomer, photoabsorption of UV-light causes the azobenzene to enter an excited state, in which the transition along the reaction coordinate is facilitated with respect to the ground state where an energetic barrier separates the *trans*- and *cis*-isomers. Typically, as reaction coordinate a geometric parameter is used, such as the angle between two specific covalent bonds.

The photon energy that is required for the excitation from the *trans* ground state to the corresponding excited state differs for different azobenzene derivatives depending on side groups, surrounding solvent etc. However, the maximum of the *trans-cis* absorption cross-section of *trans*-azobenzene typically lies in the region of UV-light (between 3 and 4 eV).

The *cis*-configuration of azobenzene is three-dimensional with the planes of the phenyl rings rotated by 60° with respect to each other. The ground state energy of the *cis*-configuration lies about 0.6 eV higher than the ground state energy of the *trans*-configuration. Due to its asymmetry, the *cis*-isomer has a static dipole moment of about 3 Debye perpendicular to the molecular axis. [40, 41] In contrast to *trans*-azobenzene, *cis*-azobenzene has an allowed $n \rightarrow \pi^*$ band at around 2.8 eV ($\varepsilon_{\max} = 1250$ l mol^{-1} cm^{-1} in n-hexane). *cis*-Azobenzene also has a $\pi \rightarrow \pi^*$ absorption band at around 4.5 eV ($\varepsilon_{\max} = 5000$ l mol^{-1} cm^{-1} in n-hexane).

Despite the fact that the isomerization process of azobenzene has been investigated theoretically and experimentally and extensively debated for more than 50 years, there is still an ongoing debate about the exact isomerization pathway of the *trans-cis* photoisomerization. [42–56] The photoisomerization of azobenzene is a rapid process occurring on the timescale of picoseconds. [57] The first process that has been proposed involves a rotation of one of the phenyl rings around the azo-group. In order to enable this rotation process, the double bond between the central nitrogen atoms is broken due to the optical excitation of an electron from a π-bonding to a π^*-antibonding orbital. [45] The second proposed photoisomerization mechanism is characterized by an inversion of one of the phenyl rings that is induced by an optical excitation of an electron from the nitrogen lone pair leading to a (n,π^*) state.
The isomerization needs some extra volume that is different for the two mechanisms. The inversion needs less free volume (≈ 0.12 nm^3) than the rotation (ca. 0.25 nm^3). [14] This comes into play if azobenzenes are integrated into densely packed arrays, *e.g.*, in thin solid films or self-assembled monolayers. More recently, both as a result of more powerful computational methods and advanced measurement techniques, mixed mechanisms such as the concerted inversion occuring on the $S_1(n\pi^*)$ surface or the inversion-assisted rotation have been proposed. [51, 58–61]

The *cis-trans* back-reaction can be induced either thermally or by irradiation with light having a different photon energy. The thermal stability of the *cis*-isomer is determined by an energetic barrier in the ground state (activation energy). The energetic barrier separating the *cis*- and *trans*-isomer is typically in the order of 1 eV, as determined by experiments in solution and quantum-chemical calculations. [62, 63] The speed of the thermal *cis-trans* conversion of molecular ensembles varies greatly

depending on the exact type of azobenzene molecule, ranging from seconds for pseudostilbenes to hours for azobenzene-type molecules. [64] Apart from thermal relaxation, the *cis-trans* isomerization can also be induced by excitation of an electron from the nitrogen lone pair on the nπ^* surface.

Apart from chemically attached substituents, the kinetics of the photoisomerization process also depends on the microenvironment. In the liquid phase, the surrounding solvent influences both the absorption spectrum and the isomerization kinetics of azobenzene. [59, 63] In the solid phase, another effect comes into play, that has been noticed already in the early 1970s. Then, it was observed that for the case of azobenzene-containing polymers the photochemical *trans-cis* isomerization is slowed down at temperatures below the glass transition temperatures of the polymers by a factor of 3. [65] The conclusion was that the relative quantum yield of the azobenzene photoisomerization depends on the microenvironment that can be described in terms such as the free volume. [66–69]

During the last decades, a lot of successful research efforts have been made towards the development of photoactive materials by incorporating azobenzene either in the side chains or the main chain of polymers and in liquid-crystal networks (LCNs). [67, 70, 71] In 1987, Eich et al. published a paper that is now among the

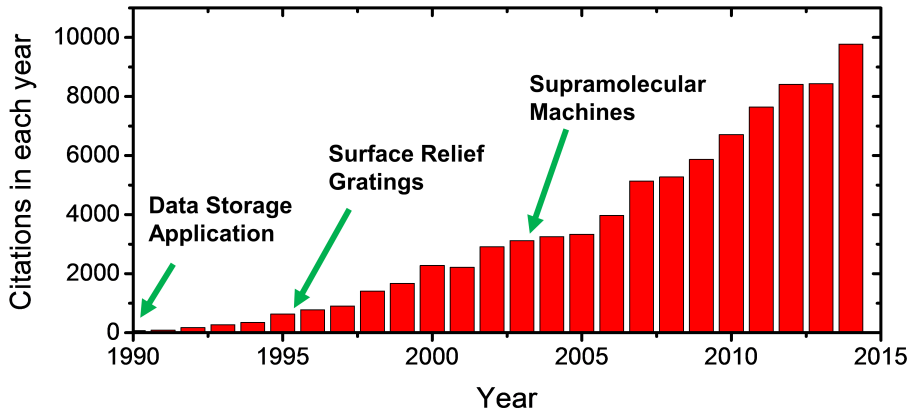

Figure 2.4: Citations in each year for the keywords 'azobenzene polymer', according to the Web of Knowledge (*Thomson Reuters*).

most cited scientific publications about azobenzene. [72] They discovered that liquid crystalline polymers with azobenzene chromophores incorporated in the side-chains can be used for optical data storage via optically induced birefringence. As a result, the research field of photoresponsive azobenzene polymers grew with hundreds of publications during the following years. The research field of azobenzene polymers received a second wave of attention after the discovery of light-induced surface relief grating (SRG) formation in the late 1990s. [73–84].

In 2003, Ikeda and coworkers showed that it is possible to convert light efficiently into mechanical work. They demonstrated that a macroscopic film of an azobenzene containing LCN could be bent in a controlled and reversible way with linearly polarized light. [85] In the following years, they used this principle to build many different light-driven motors. [86–89] Without a doubt, all these experimental findings are very impressive on their own, but, in many cases, the fundamental understanding of the molecular processes that were responsible for the observed photoresponsive effects lacked behind. For example, about 20 years after the discovery of light-induced surface relief gratings, the physical origin of their formation is still not fully understood. [84]
Figure 2.4 shows the citations in each year for the keywords 'azobenzene polymer'. Starting in the early 1980s, the number of citations has grown in almost every year. Also note that around the year 2006, the research field has received a new wave of attention, probably influenced by the exciting findings of Tomiki Ikeda and his coworkers. Over the last decade, the number of citations per year in the field of azobenzene polymers has more than doubled and reached nearly 10000 citations in the year 2014, showing the huge interest in the field.

For most applications with industrial and technological relevance, a higher packing density of molecular switches is desirable. In recent years, azobenzene has been integrated into densely packed and structurally well defined assemblies. Consequently, the influence of the microenvironment on the switching process became increasingly important. It was found that both the interaction with a surface [62, 90–103] and the intermolecular coupling [24, 25, 104–106] influences or even suppresses the isomerization of azobenzene and other switches. Decoupling of the photochromic units from the substrate and from adjacent photochromes can be achieved using bulky spacers [107, 108], legs [90, 97, 108–111], molecular platforms [112–115] or self-assembled monolayers (SAMs) as linkers [22, 104, 105, 116–119]. See also ref. [120] for an overview over the different approaches to immobilize azobenzenes onto surfaces. However, intermolecular coupling of molecular switches or electronic coupling to the substrate can also support the switching. In 2009, Wolf et. al showed that the azobenzene derivative tetra-*tert*-butyl-azobenzene (TBA) can be switched in direct contact to a Au(111) surface by some substrate mediated excitation process. They found that the switching mechanism involves a charge transfer process, in which photogenerated holes in the gold surface cause a transient positive ion formation and thereby enable the azobenzenes to switch.
In 2007, Pace et al. reported cooperative switching of azobenzene chromophores in a 2D crystalline domain, where the isomerization of individual azobenzene units is

suppressed for sterical reasons. [22] Cooperative switching effects are not limited to supramolecular aggregates like, *e.g.*, SAMs but have also been observed for individual molecules in the case of multi-azobenzene compounds. [31, 121, 122] In 2012, Hecht and coworkers managed to synthesize foldamers with two azobenzenes incorporated in the backbone. It was shown that the helix-coil transition of the foldamers, triggered by the isomerization of one azobenzene, facilitates the photoisomerization process of the second azobenzene due to $\pi - \pi$ stacking.
A rather new research area deals with the photochemistry and photophysics of polymers with azobenzene in the main chain. In contrast to polymers with azobenzene in the side chains, where the conversion of light into mechanical work is mediated by a phase transition, main-chain azobenzene polymers show a direct photoresponse that typically leads to larger geometric changes of the single polymers. The reason for this is that the light-induced deformation of a main-chain azobenzene polymer is a result of the deformations of the individual monomers. Experiments performed in 2002 by Hugel et al. showed that isolated azobenzene polymers with azobenzene incorporated in the main chain can be used as artificial light-driven muscles that can create forces of several hundred pN. [123–125] One of the fundamental challenges in the research field of main-chain azobenzene polymers is that the azobenzene chromophores have to be electronically decoupled along the polymer main chain. Recently, Bléger et al. showed that electronic decoupling can be achieved by introducting large dihedral angles between the azobenzene groups along the polymeric chain. [126] As a demonstration, they synthesized a new class of azobenzene main chain polymers that undergo a rod-coil transition upon UV-irradiation. [127]. Future photoactuation devices could, *e.g.*, be used to directly convert sunlight into mechanical work, circumventing the need to store the solar energy in energy-rich fuels. [128] Photoactuation devices based on azobenzene can not only be used for energy conversion but also for energy storage in the form of thermal solar fuels, as Kucharski et al. demonstrated in 2014. [7] Every light-induced *trans-cis* isomerization of an azobenzene chromophore will store a certain amount of energy that equals the difference between the energy levels of *trans*- and *cis*-azobenzene (typically 0.6 eV for an isolated azobenzene molecule). The stored energy can be released by heating the thermal solar fuel which will convert the *cis*-azobenzenes back to *trans*.

2.2 N-alkanes

All of the multi-azobenzene compounds that are investigated in this thesis are equipped with alkyl side chains. Despite their simple chemical structure, linear alka-

nes (n-alkanes) show a rich and complex phase behavior in the solid state. Rotator phases have been found, [129,130] *i.e.* in which n-alkanes with certain chain-lengths undergo first-order phase transitions upon heating. Another example is the odd-even effect [131,132] where monolayers of n-alkanes adsorb in specific geometries on substrates and have different boiling points depending on whether they have an odd or even number of carbon chain-segments. N-alkanes can be regarded as multifunctional tools for molecular design and material science. Attached to more complex molecules alkyl chains will often govern the molecular packing structure and thus also the macroscopic properties of materials. For example it has been shown that alkyl chains attached to molecular switches make it possible to immobilize molecular switches on surfaces. [120] N-alkanes can also be used as flexible alkyl side chains for polymers. It has been shown that the attachment of alkyl side chains to polymers drastically changes the structural, electronic and thermodynamical behavior of a polymeric thin film. [133–136] In particular, the influence of chain-length on molecular structure and other physical properties has been investigated for many systems based on hydrocarbon chains. [137–144]

2.3 Substrates

Native silicon oxide

Si(100) wafers, covered with native oxide (*Si-mat*), have been used as substrates both for azobenzene trimers in chapter 5 and azobenzene oligomers in chapter 6. Before the deposition process, the silicon wafers were cleaned with acetone, isopropanol and ultra-pure water in an ultrasonic bath.

Mica

The multilayer thin films of azobenzene main-chain polymers that are investigated in chapter 4 of this thesis have been prepared on muscovite mica via spin-coating. Muscovite mica ($KAI_3Si_3O_{12}H_2$) is a mineral that can be found in granites, pegmatites, gneisses and schists or as a secondary mineral. In nature, it is often found in large, transparent and highly elastic sheets with a size of up to several m^2. The physical reason for this is that mica has a almost perfect basal cleavage. [145] This makes it also a very good substrate for atomic force microscopy studies where an atomically flat surface is desirable. [146] The mica substrates that have been used in this thesis were purchased from *Plano GmbH*.

3 Techniques

Understanding switching of molecular ensembles demands a combination of spectroscopic and structural measurement techniques. The combination of real space techniques, *e.g.*, microscopy with reciprocal space methods such as X-ray scattering allows to determine the structural properties of a sample from macroscopic scales down to the atomic level (see Figure 3.1).

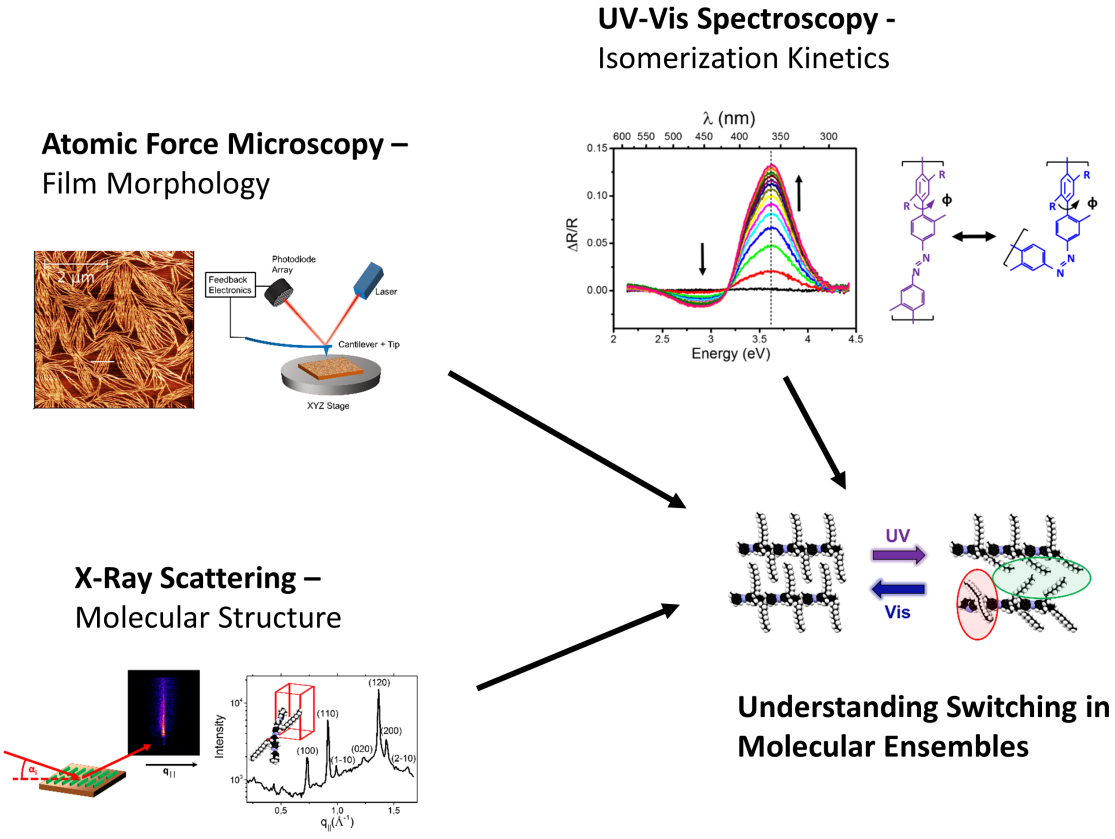

Figure 3.1: Overview over the experimental techniques used in this thesis.

This chapter is organized as follows: Firstly, atomic force microscopy (AFM) is introduced as a real-space method to image thin film morphology and topography. Afterwards, a short introduction into X-ray scattering is given, including a section about the interaction of X-rays with matter and sections about the measurement techniques of X-ray reflectivity (XRR) and grazing incidence X-ray diffraction

(GIXD). Next, differential reflectance spectroscopy (DRS) is introduced as a technique to study the optical absorbance of thin films and to monitor the photoisomerization of molecular switches. Finally, a brief description of spin coating is given which was used to prepare the samples that were studied in this thesis.

3.1 Atomic force microscopy (AFM)

The technique of atomic force microscopy (AFM) that allows one to visualize surfaces on atomic scale was developed at the IBM Research Laboratory in San Jose and introduced to the scientific community in 1986 by Binnig, Quate and Gerber. [147] Whereas the resolution of far field techniques such as optical or electron microscopy

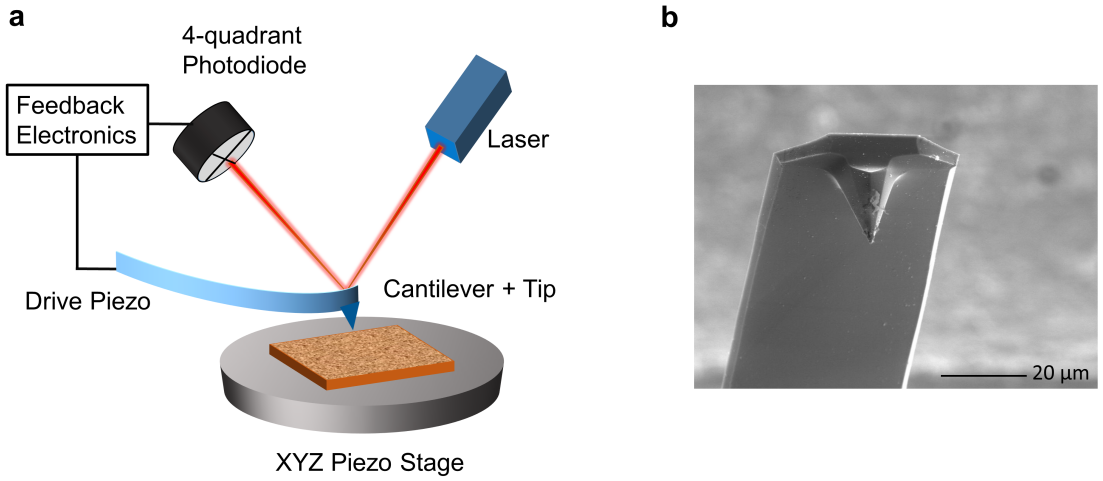

Figure 3.2: Principle of Atomic Force Microscopy (AFM). (a) Illustration of the setup and the working principle of AFM and (b) image of a cantilever with a Tip (taken with permission from ref. [148]).

is limited to one half of the wavelength that is used, AFM allows for a much better spatial resolution. AFM, also known as Scanning Force Microscopy (SFM), is well suited for the characterization of thin film morphologies and surface topographies since it provides an excellent resolution both in the z-direction (< 1 nm) and in the lateral direction (typically < 10 nm, depending on the tip geometry). The basic working principle of AFM is shown in Figure 3.2. The typical setup consists of a spring-like cantilever that is attached to a piezoelectric drive element which oscillates the cantilever at a specific frequency. At the other end of the cantilever is a sharp tip, pointing towards the surface of the sample. The scanning is either performed with a XYZ piezo-stage under the sample holder or by scanning the cantilever tip across the fixed sample.

Due to the interaction with the sample surface, the scanning tip experiences a specific

deflection at every spot of the sample. The change of the motion of the cantilever is monitored with the help of a laser beam that is reflected on the cantilever and detected by a four quadrant photodiode array. The vertical deflection can be calculated by comparing the amount of electrical signal generated in the top and bottom halves of the photodiode.

$$\text{Vertical Deflection} \Leftrightarrow \frac{\text{Signal}_{\text{top}} - \text{Signal}_{\text{bottom}}}{\text{Signal}_{\text{top}} + \text{Signal}_{\text{bottom}}} \tag{3.1}$$

In the same way, one can measure the lateral twisting of the cantilever by comparing the amount of signal generated in the right and left halves of the photodiode which can be used for measurements in friction mode that give lateral force images. Since the deflection of the cantilever is highly sensitive to the interaction between the surface and the scanning tip, this technique allows one to map the surface topography very efficiently.

3.1.1 Operating modes

The tip-surface interaction is governed by different forces, depending on the tip-surface distance. Very close to the surface, Coulomb interactions predominate, while for slightly larger tip-surface distances attractive van der Waals forces predominate. An AFM machine can be operated in different ways. They can be categorized as contact modes (constant height mode or constant force mode) and non-contact modes (tapping mode or acoustic mode). In contact mode (constant height or constant force), the AFM tip is lowered until it is in the repulsive regime of the sample surface. The tip-surface distance is typically smaller than 0.5 nm. The overlapping orbitals of tip- and surface electrons lead to a repulsive force and consequently a deflection of the cantilever. In the constant height scanning mode, the height of the AFM tip is kept constant and the deflection of the cantilever only depends on the height of the surface. In the constant force mode, the force between the AFM tip and the surface is kept constant, requiring that the tip-surface distance is continually readjusted. While contact mode is well suited for very smooth surfaces, the strong tip-surface interaction can lead to fast deterioration of the AFM tip for rougher or harder samples and also to sample damage.
In contrast, non-contact modes are well suited for harder surfaces because the tip does not touch the surface during measurements. Furthermore, scanning a sample in non-contact mode usually is more gentle to the sample than scanning in contact mode which can be important for dynamic measurements, where it has to be excluded that the sample morphology is influenced in any way by the AFM tip. In

non-contact mode the AFM tip is oscillating at its resonance frequency. Attractive forces between the tip and the surface lead to a lower oscillation frequency while repulsive forces lead to a higher oscillation frequency of the cantilever (see Figure 3.3). In the absence of a surface, the oscillation of the free cantilever would be

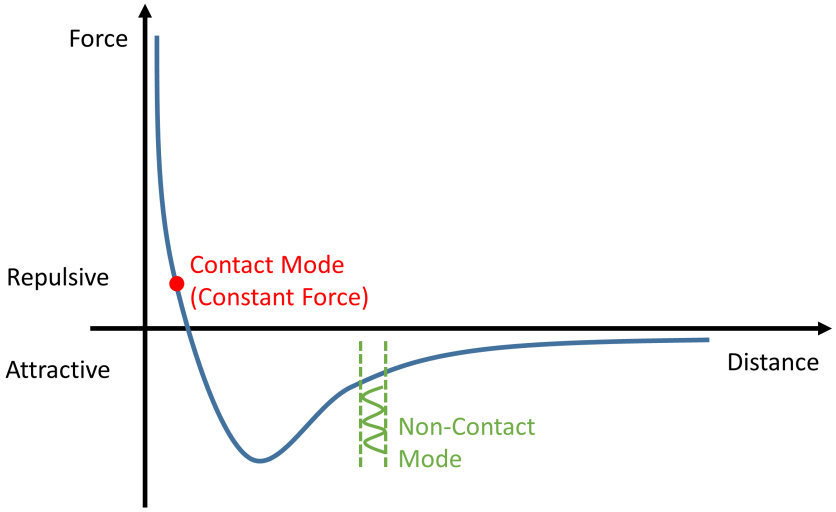

Figure 3.3: Overview of different operating modes corresponding to different regimes in the force potential.

described by a harmonic potential

$$V^{Spring} = \frac{1}{2}kz^2 \tag{3.2}$$

with k being the spring constant of the cantilever and z being the vertical deflection of the tip. In the presence of a surface, the oscillation of the cantilever is disturbed. The disturbance can be described via an additional harmonic potential with a different spring constant k_s. The resonance frequency then becomes

$$f = f_0 + \Delta f = \frac{1}{2\pi}\sqrt{\frac{k \pm k_s}{m}}. \tag{3.3}$$

Here, f_0 is the resonance frequency and m is the mass of the free cantilever. Note that the additional harmonic potential can lead to an attractive or a repulsive force between the surface and the tip. As a consequence, k_s will be added (repulsive force) to the spring constant of the free cantilever k or subtracted (attractive force) from it. In tapping mode, the following three types of data can be collected:

- Height data: The height of the sample can be measured via the z-position of the XYZ piezo stage on which the sample is mounted or alternatively, via the

z-position of the AFM tip. Height images show the local sample topography.

- Phase data: The offset (angle) in the phase between the input drive signal corresponding to the piezo driving the cantilever oscillation and the phase of the cantilever response signal as measured with the photodiode array. Phase images contain information about the local elasticity of a sample.
- Amplitude data: One can monitor the amplitude of the cantilever oscillation. For this, it is important that the laser spot on the photodiode is large enough to irradiate both halves of the photodiode. Amplitude images can show outlines of surface features very well.

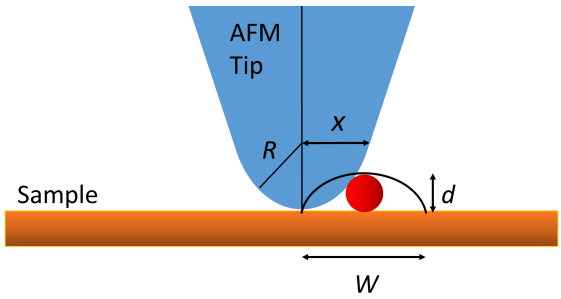

Figure 3.4: Broadening of the observed lateral width of sample features due to the finite AFM tip radius.

It is important to note that the observed lateral width of a feature can be larger than the actual width of the sample feature due to the finite radius of the AFM radius limiting the lateral resolution (see Figure 3.4). For obvious geometrical reasons, the tip radius R, the observed width of the feature $W = 2x$ and the actual width of the sample feature d are related via

$$\frac{W}{2} = R^2 - (R - d)^2 \tag{3.4}$$

For $R \gg d$, one can approximate the observed width of the feature W as

$$W = \sqrt{8dR}. \tag{3.5}$$

For, *e.g.*, $R = 10$ nm and $d = 5$ nm, the observed width is $W = 20$ nm.
All AFM images presented in this thesis have been recorded in tapping mode using a *JPK NanoWizard II ®*.

3.2 X-ray scattering

The term *X-rays* describes a form of high energy electromagnetic radiation with wavelengths ranging from 10^{-11} m to 10^{-8} m corresponding to energies in the range 0.1 keV to 100 keV. For X-ray scattering, typically hard X-rays with photon energies above 5 keV are used because of their ability to penetrate air.

X-rays can be generated in several different ways. A simple X-ray source consists of hot cathode inside a vacuum tube. With a high voltage the electrons are accelerated to high velocity. When the accelerated electrons hit the anode, typically a metal target, X-rays are created by two different processes. Characteristic X-ray emission is specific for the target element. It is emitted when outer-shell electrons fill a vacancy in the inner shell that was produced by the collision of accelerated electrons with the target material. The second radiation type is *Bremsstrahlung* which is given off when the high velocity electrons are decelerated in the electric field of the nuclei of the target atoms. In contrast to characteristic X-ray emission, the *Bremsstrahlung* has a continuous spectrum. The most common target material

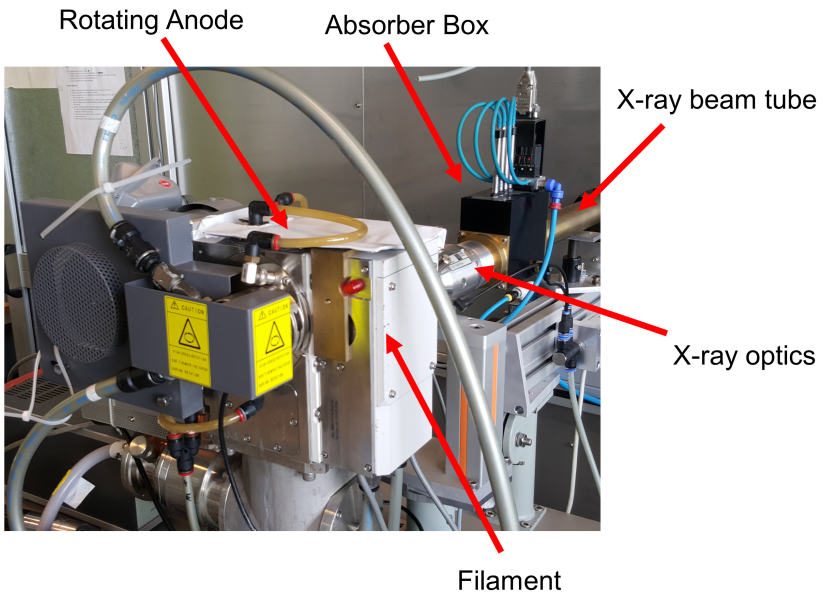

Figure 3.5: Rotating anode X-ray tube.

for X-ray crystallography is copper whose strongest characteristic X-ray emission line corresponds to a photon energy of 8.05 eV (Cu $K_{\alpha 1}$). The X-ray photon flux can be significantly increased by using a rotating anode tube instead of a static X-ray tube (see Fig. 3.5). Most of the X-ray scattering data presented in this thesis has been measured with a system consisting of a rotating copper anode (Rigaku)

and a Göbel mirror. A Göbel mirror consists of multilayers with laterally graded thickness that can be used to focus or collimate an X-ray beam because, for a single photon energy, only X-rays with a certain angle of incidence (corresponding to the multilayer Bragg peak) with respect to the mirror are reflected. X-ray radiation with

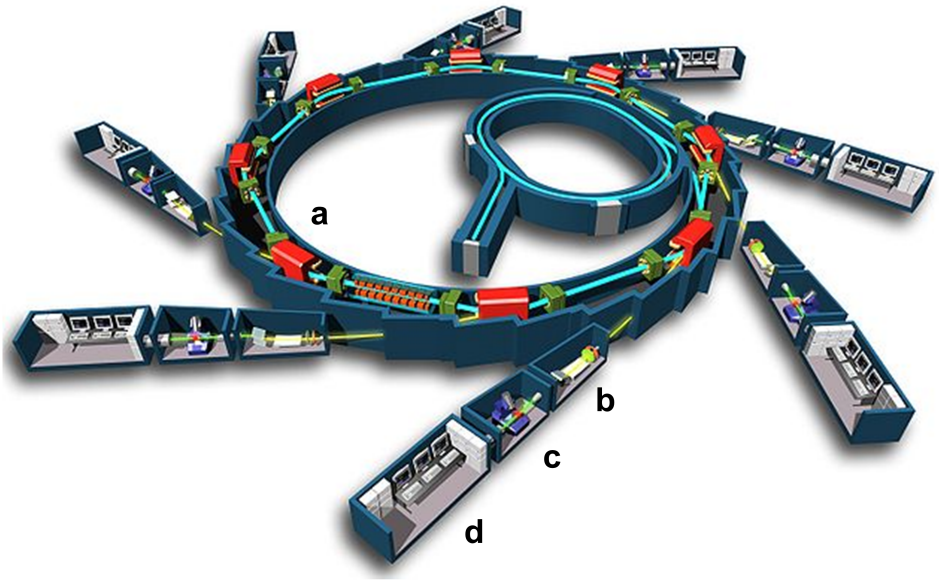

Figure 3.6: Scheme of the *Soleil* synchrotron with undulator (a), optics hutch with monochromator (b), experimental hutch (c) and control room (d). Image taken with permission from ref. [149]

a much higher photon flux, a smaller beam divergence and larger spatial coherence can be produced by a synchrotron. A synchrotron is a cyclic particle accelerator in which a continuous or pulsed particle beam is guided by the magnetic fields of bending magnets, wigglers and undulators. Synchrotron radiation is generated by the acceleration of ultrarelativistic charged particles through magnetic fields. Several experimental endstations (beamlines) can be operated simultaneously. Figure 3.6 shows a scheme of the *Soleil* synchrotron. In the storage ring, the electrons traverse through straight sections (undulators) that consist of a periodic structure of dipole magnets. In these undulators, electrons are forced to undergo oscillations and thus to radiate energy. The contributions from the passage of an electron through such an undulator add coherently, resulting in a very bright X-ray beam. Directly after the undulator, the X-ray beam has a wide spectral distribution. Since most synchrotron experiments require a monochromatic beam, each beamline has an optics hutch with a monochromator, typically a perfect crystal where the desired wavelength can be selected according to Bragg's law. Besides a monochromator, the optics hutch may also contain X-ray mirrors and refractive Fresnel lenses for focussing the X-ray beam.

3.2.1 Interaction of X-rays with matter

In this section, we follow the treatment of X-ray scattering presented in ref. [150]. A monochromatic ideally collimated X-ray beam can be treated mathematically as a linearly polarized plane wave $\mathbf{E}(\mathbf{r}, t)$. The polarization of the electric field can be written as a unit vector $\hat{\epsilon}$, and the wavevector along the direction of propagation as $\mathbf{k}$ with the wavenumber $|\mathbf{k}| = 2\pi/\lambda$, so that

$$\mathbf{E}(\mathbf{r}, t) = \hat{\epsilon} E_0 e^{i(\mathbf{k}\cdot\mathbf{r} - \omega t)}. \tag{3.6}$$

X-ray scattering by a single electron.

When X-ray photons are scattered on a single electron, the electron is forced to vibrate by the electric field of the incoming X-ray beam. The vibrating electron acts as a small dipole antenna and radiates an electromagnetic field. X-rays are either scattered elastically or inelastically. Inelastic scattering, where the scattered photon has a longer wavelength relative to the incident photon, is also known as Compton scattering. However, the elastic scattering of X-ray photons is the more important process for structural studies of materials. In elastic scattering, momentum may be transferred between the X-ray photons and the electrons. Therefore it is useful to define the momentum transfer vector $\mathbf{q}$ as the difference between incoming wave $\mathbf{k_i}$ and outgoing wave $\mathbf{k_f}$ as $\mathbf{q} = \mathbf{k_f} - \mathbf{k_i}$.

The ability of an electron to scatter X-rays can be expressed in terms of a *scattering length* r_0 which is, for a fixed scattering angle, proportional to the ratio of the magnitude of the radiated to incident field.

$$r_0 = \left(\frac{e^2}{4\pi\epsilon_0 m c^2} \right) = 2.82 \times 10^{-5} \text{Å}. \tag{3.7}$$

X-ray scattering by a single atom.

The interaction of X-rays with a single atom can be described as scattering on an electron density distribution $\rho(\mathbf{r})$. The scattered radiation field is a superposition of contributions from different volume elements of this electron density distribution. The phase difference for the incoming wave between two volume elements, one at $\mathbf{r}$ and one at the origin, is the scalar product $\mathbf{k_i} \cdot \mathbf{r}$. Consequently, the phase difference for the outgoing wave with wavevector $\mathbf{k_f}$ between two volume elements, one at $\mathbf{r}$ and one at the origin, is $-\mathbf{k_f} \cdot \mathbf{r}$. The resulting total phase difference between the two scattered waves is thus

$$\Delta\phi(\mathbf{r}) = (\mathbf{k_i} - \mathbf{k_f}) \cdot \mathbf{r} = \mathbf{q} \cdot \mathbf{r} \tag{3.8}$$

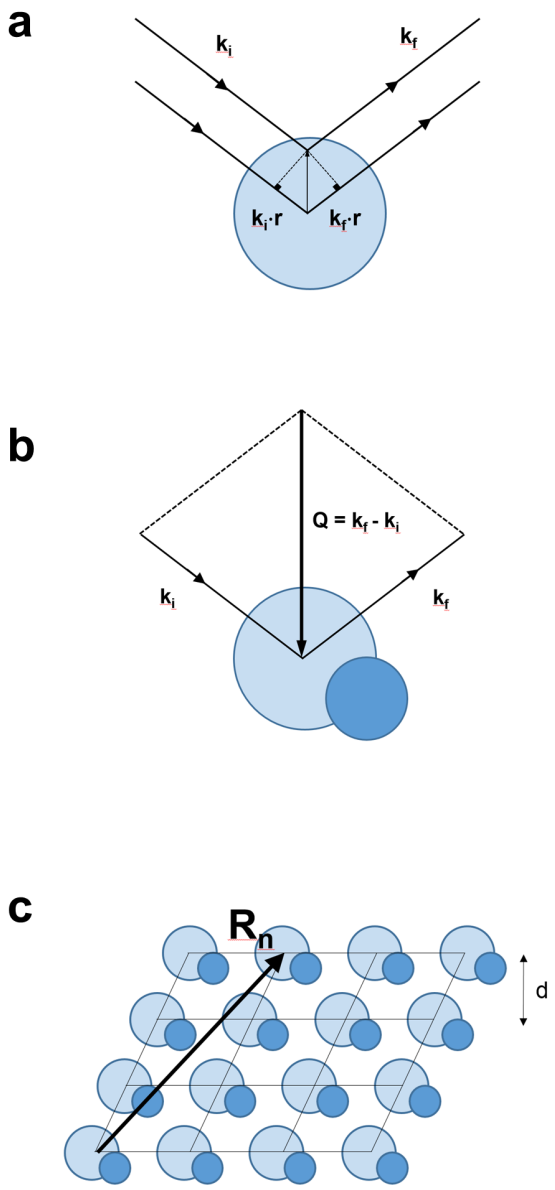

Figure 3.7: (a) Elastic scattering from two volume elements with a spacing **r** within a single atom. The phase difference between a wave scattered at the origin and one at **r** is $\mathbf{q} \cdot \mathbf{r}$, which defines the wavevector transfer **q**. (b) Scattering from a molecule. (c) Scattering from a molecular crystal. $\mathbf{R_n}$ denotes the lattice position vector and d denotes the lattice spacing.

where $\mathbf{q}$ is the wavevector transfer.
Figure 3.7a illustrates elastic scattering ($|\mathbf{k_i}| = |\mathbf{k_f}|$) of X-rays at two different volume elements within a single atom. Thus $|\mathbf{q}| = 2\,|\mathbf{k_i}| \sin\,\theta = (4\pi/\lambda)\sin\,\theta$. Thus a volume element $d\mathbf{r}$ at $\mathbf{r}$ contributes an amount $-r_0\rho(\mathbf{r})d\mathbf{r}$ to the scattered field with a phase factor of $e^{i\mathbf{q}\cdot\mathbf{r}}$. The total scattering length of the atom can be written as

$$-\,r_0 f^0(\mathbf{q}) = -r_0 \int \rho(\mathbf{r}) e^{i\mathbf{q}\cdot\mathbf{r}} d\mathbf{r} \tag{3.9}$$

where $f^0(\mathbf{q})$ is the *atomic form factor*.

X-ray scattering by a molecule.
Just as the scattered radiation field of an atom can be described as the superposition of contributions from different volume elements, the scattered radiation field of a molecule can be described as the superposition of contributions from its different atoms (see figure3.7b). Labelling the different atoms in the molecule by index j, we can write the form factor of the molecule

$$F^{mol}(\mathbf{q}) = \sum_{\mathbf{r}_j} f_j(\mathbf{q}) e^{i\mathbf{q}\cdot\mathbf{r}_j} \tag{3.10}$$

where $f_j(\mathbf{q})$ is the atomic form factor of the j'th atom of the molecule. Here, the constant factor of $-r_0$ has been neglected.

X-Ray scattering by a crystal.
A molecular crystal can be defined as a supramolecular structure that is periodic in space (see Figure 3.7c). The scattering of X-rays at the periodic crystal planes can be described by Bragg's law

$$m\lambda = 2d\,\sin\,(\theta) \tag{3.11}$$

where θ is the angle of incidence of the X-rays relative to the crystal planes, d denotes the lattice spacing of the crystal and m is an integer.

Bragg's law, however, only describes at which angle of incidence the intensity of the outgoing wave is maximal when an X-ray beam is scattered by a crystal lattice. For a quantitative description of the outgoing X-ray wave, the exact electron density distribution within the crystal lattice and the scattering ability of the molecules within the crystal unit cell have to be considered. If $\mathbf{R_n}$ are the lattice vectors and $\mathbf{r}_j$ is the position of the atoms with respect to any one particular lattice site, then the position of any atom in the crystal is given by $\mathbf{R_n} + \mathbf{r}_j$. Thus the scattering amplitude for X-rays scattered by a crystal can be factorized into two separate terms:

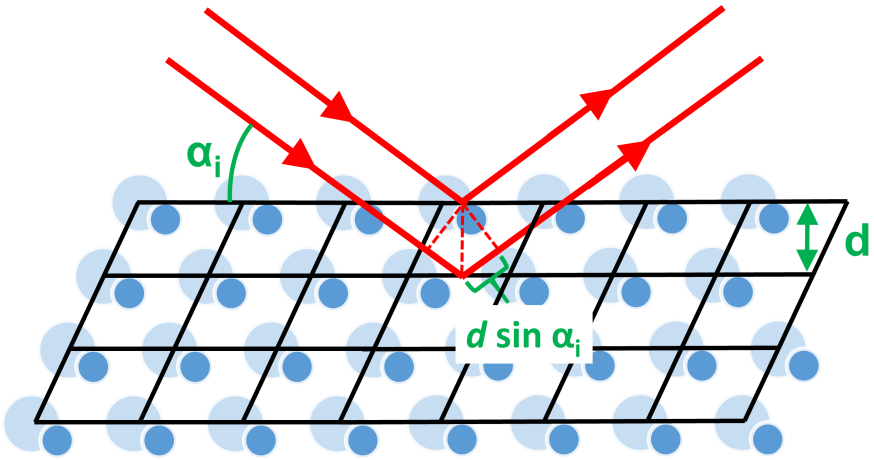

Figure 3.8: Illustration of Bragg's law.

$$F^{crystal}(\mathbf{q}) = \overbrace{\sum_{\mathbf{r}_j} f_j(\mathbf{q}) e^{i\mathbf{q}\cdot\mathbf{r}_j}}^{\text{Unit cell structure factor}} \overbrace{\sum_{\mathbf{R_n}} e^{i\mathbf{q}\cdot\mathbf{R_n}}}^{\text{Lattice sum}} \tag{3.12}$$

Again, the factor $-r_0$ has been neglected.

Reciprocal space.

Note that the lattice sum in equation 3.12 is maximal if the condition

$$\mathbf{q}\cdot\mathbf{R_n} = 2\pi \times integer \tag{3.13}$$

is fulfilled. In the following it is shown that there is a set of vectors $\mathbf{q}$ in reciprocal space for which the above given condition is always true.

The lattice vectors $\mathbf{R_n}$ can be expressed as the linear combination of the three basis vectors of the 3D lattice $(\mathbf{a}_1, \mathbf{a}_2, \mathbf{a}_3)$

$$\mathbf{R_n} = n_1\mathbf{a}_1 + n_2\mathbf{a}_2 + n_3\mathbf{a}_3 \tag{3.14}$$

where (n_1, n_2, n_3) are integers.

One can define a set of reciprocal lattice basis vectors $(\mathbf{a}_1^*, \mathbf{a}_2^*, \mathbf{a}_3^*)$ that allows one to describe any point in the reciprocal lattice as a linear combination of the basis vectors:

$$\mathbf{a}_1^* = 2\pi\frac{\mathbf{a}_2\times\mathbf{a}_3}{\mathbf{a}_1\cdot(\mathbf{a}_2\times\mathbf{a}_3)}, \mathbf{a}_2^* = 2\pi\frac{\mathbf{a}_3\times\mathbf{a}_1}{\mathbf{a}_1\cdot(\mathbf{a}_2\times\mathbf{a}_3)}, \mathbf{a}_3^* = 2\pi\frac{\mathbf{a}_1\times\mathbf{a}_2}{\mathbf{a}_1\cdot(\mathbf{a}_2\times\mathbf{a}_3)}. \tag{3.15}$$

The lattice sum is maximal for every lattice site $\mathbf{G} = h\mathbf{a}_1^* + k\mathbf{a}_2^* + l\mathbf{a}_3^*$ in the reciprocal lattice because

$$\mathbf{G} \cdot \mathbf{R_n} = 2\pi(hn_1 + kn_2 + ln_3) = 2\pi \times integer \tag{3.16}$$

This means that $F^{crystal}(\mathbf{q})$ and thus the scattered intensity is only non-vanishing if $\mathbf{q} = \mathbf{G}$. This is also called the Laue condition which can be shown to be equivalent to Bragg's law. In this section we have neglected multiple scattering effects, that is the possibility that the scattered X-ray beam is scattered a second or third time before leaving the crystal. For most molecular crystals this so called *kinematical approximation* is a reasonable assumption, but it may break down for macroscopic perfect crystals.

3.2.2 X-ray reflectivity (XRR)

So far, this chapter dealt with the interaction of X-rays with electrons, atoms, molecules and crystals. The logical next step is the interaction of X-rays with thin films in general, may they be crystalline or amorphous. Since X-rays are, just as visible light, electromagnetic waves, there are also refraction and reflection effects for X-rays at interfaces between different media. However, X-rays have a much higher energy than visible light. The refractive index for X-rays is very close to one, which is the refractive index of vacuum (see Figure 3.9). Thus, it is convenient to write

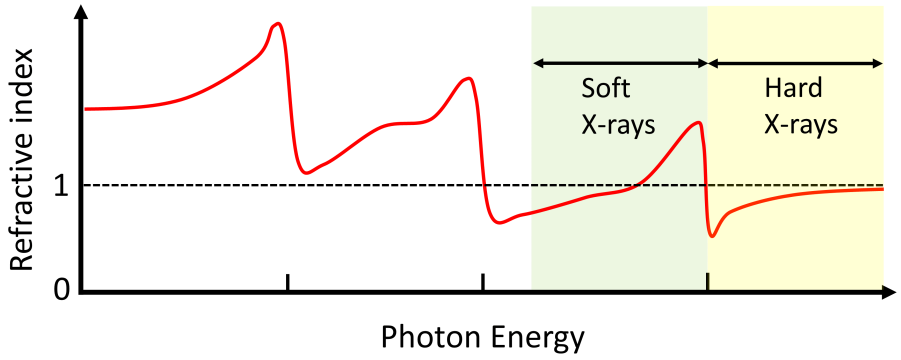

Figure 3.9: Illustration of the refractive index for different photon energies.

the refractive index for X-rays as

$$n = 1 - \delta + i\beta \tag{3.17}$$

where δ is of order 10^{-5} in solid materials and around 10^{-8} in air. The imaginary part β that describes absorption is typically much smaller than that. The material

constants δ and β can also be expressed in terms of the electron density ρ_e, the scatting length of an electron r_e, the X-ray wavelength λ and the absorption coefficient μ. [150]

$$\delta = \frac{\lambda^2}{2\pi} r_e \rho_e \tag{3.18}$$

$$\beta = \frac{\lambda}{4\pi} \mu \tag{3.19}$$

An important result of the fact that n is smaller than unity for X-rays is that X-rays can undergo total external reflection for grazing angles of incidence. This can be seen via Snell's law

$$\cos \alpha_i = n \cos \alpha_r \tag{3.20}$$

where α_i is the incident grazing angle of the X-rays and α_r is the refracted grazing angle. For X-rays, equation 3.20 has a solution for $\alpha_r \leq 0$, which means that total external reflection of X-rays is possible. The solution for $\alpha_r = 0$ is called *critical angle* α_c. The critical angle is related to the refractive index (for $\beta = 0$) of the material via

$$\alpha_c = \sqrt{2\delta}. \tag{3.21}$$

For X-ray reflectivity measurements in the so called Bragg-Brentano or $\theta - 2\theta$-geometry, the angle of incidence α_i and the angle of reflection α_r always fulfill the condition $\alpha_i = \alpha_r$. Under this condition (and for a fixed X-ray energy), each α_i corresponds to a specific absolute value of the component of the wavevector transfer that is perpendicular to the substrate surface $|\mathbf{q}_\perp| = q_\perp$. Usually, the X-ray reflectivity is plotted against $q_\perp$ (also denoted as q_z) because this method, in contrast to plots against α_i takes the X-ray energy into account.

Kiessig fringes

For incident angles $\alpha_i > \alpha_c$, the X-ray reflectivity $R(q_\perp)$ of a smooth surface decays according to the Fresnel equations with $R \propto 1/q_\perp^4$. The situation changes when one considers a flat layer on top of the smooth substrate surface. X-rays get reflected and refracted at two interfaces in this case, the vacuum-layer and the layer-substrate interface. The X-rays reflected at the two interfaces can interfere constructively or destructively, depending on the angle of incidence or $q_\perp$, respectively, and the thickness of the layer d. The resulting oscillations in the X-ray reflectivity curve are called *Kiessig fringes*. It is possible to determine the layer thickness d from the $\Delta q_\perp$

spacing of the minima of the Kiessig fringes:

$$d = \frac{2\pi}{\Delta q_\perp}. \tag{3.22}$$

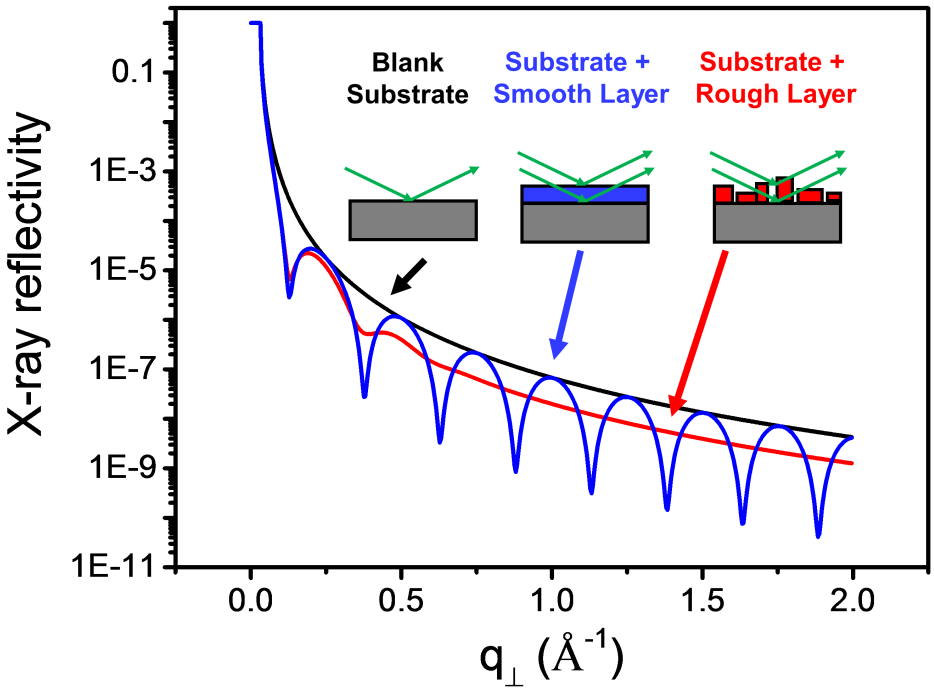

Figure 3.10: Simulated X-ray reflectivity of a perfect smooth substrate surface (black curve) and of the same substrate covered with a perfect smooth layer on top (blue curve) and with a rough layer (σ = 4Å) on top (red curve).

The XRR curves shown in Figure 3.10 are based on the assumption of a perfect smooth interface. In reality, however, most surfaces and interfaces deviate from the perfect smooth situation. The degree of this deviation can be expressed in terms of a surface roughness σ. In general, the X-ray reflectivity of a rough surface will be lower than the reflectivity of a perfect smooth surface. Also the Kiessig fringes typically have less pronounced minima and maxima or might even be completely invisible for a rough surface (see Figure 3.10).

Parratt formalism

In order to extract quantitative information from a measured XRR curve, one has to fit the XRR data with a suitable model. A commonly used model is the *Parratt formalism* [151] for systems with several interfaces. The Parratt formalism is a recursive algorithm that describes the ratio X_j of reflected amplitude R_j and trans-

mitted amplitude T_j for every layer j. Every X_j can be calculated according to the formula

$$X_j = \frac{R_j}{T_j} = e^{-2ik_{z,j}} \frac{r_{j,j+1} + X_{j+1} e^{2ik_{z,j+1} z_j}}{1 + r_{j,j+1} X_{j+1} e^{2ik_{z,j+1} z_j}} \tag{3.23}$$

where $k_{z,j}$ denotes the z-component of the wavevector of the X-ray beam in the j'th layer. $r_{j,j+1}$ denotes the Fresnel coefficient describing the reflectance $R_{j,j+1} = |r_{j,j+1}|^2$ of the interface between the j'th and the $j+1$'th layer:

$$r_{j,j+q} = \frac{k_{z,j} - k_{z,j+1}}{k_{z,j} + k_{z,j+1}} \tag{3.24}$$

For a multilayer system with $n+1$ layers and n interfaces, the recursion starts with $R_{n+1} = 0$.

It is important to note that the Parratt formalism uses the full dynamic scattering theory, that is, it inherently takes into account multiple scattering from different interfaces.

In contrast to the recursive Parratt formalism, one can also simulate the X-ray reflectivity of a multilayer system with ananalytical formula using the so called kinematic approximation. Namely, the kinematic model consists of the following approximations:

- The intensity of the incident beam decreases isotropically when crossing the sample. Extinction, multiple diffraction and anomalous absorption are neglected.
- The scattered intensity is small in comparison with the incident intensity. Coherence is maintained throughout the sample and thermal diffuse scattering is ignored.
- Only elastic and coherent scattering is considered. The detector is assumed to be far away, that is, the scattered wave is treated as a plane wave at the detector position.
- Compton scattering and fluorescence or anomalous scattering effects due to electron excitation are neglected.

The kinematical approximation can neither be applied for perfect crystal samples, nor for samples consisting of randomly oriented crystallites. However, for samples with a finite mosaicity (disorder among the single crystallites), the kinematic approximation can give accurate results.

3.2.3 Grazing incidence X-ray diffraction (GIXD)

For incident grazing angles $\alpha_i < \alpha_c$, there is an evanescent wave within the refracting medium that propagates parallel to the interfacial plane. The corresponding perpendicular electric field of the evanescent wave decays exponentially with increasing penetration depth z:

$$E \propto e^{ik_{t,z}z} = e^{-ik\sqrt{\alpha_i^2-\alpha_c^2}z} = e^{-z/\Lambda}. \tag{3.25}$$

For organic materials, the penetration depth Λ lies typically in the range of a few nm. This makes grazing incidence X-ray diffraction (GIXD) a highly sensitive tool to study the in-plane structure of organic thin films, since this small penetration depth reduces the background scattering from the inorganic substrate significantly.

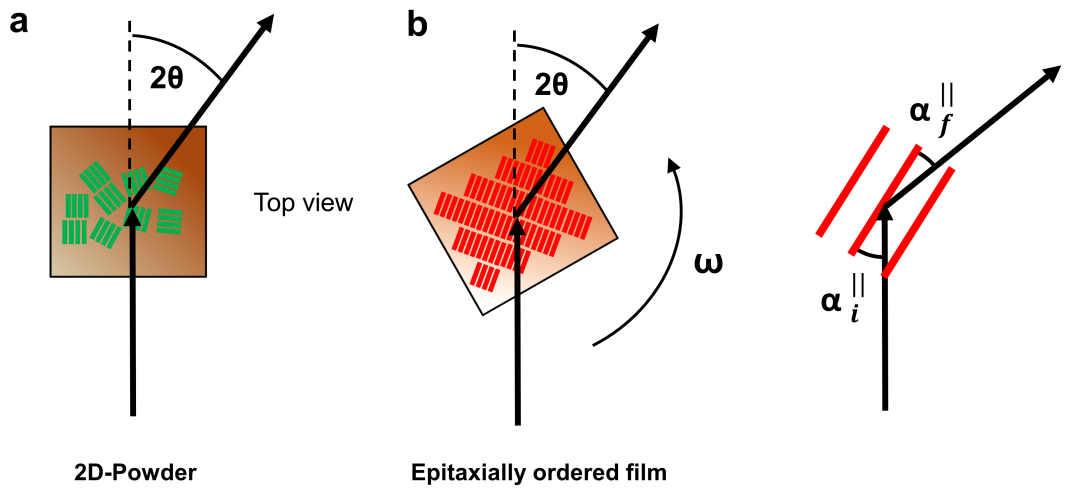

Figure 3.11: Scattering and scanning geometry in grazing incidence X-ray diffraction (GIXD). (a) Scanning geometry for 2D-powder materials. Only the detector angle 2θ is scanned. (b) Scanning geometry for epitaxially ordered films. Both the detector angle 2θ and the azimuthal angle ω are scanned.

Figure 3.11 shows two possible scanning modes for GIXD. If the material is a 2D-powder, that is, if the crystalline domains within the film have no defined orientation with respect to each other, only the detector angle 2θ is scanned, similar to the Debye-Scherrer scanning geometry for 3D-powders. The reason for this is that the X-ray beam will always hit some crystallites whose lattice planes are oriented with respect to the X-rays in such a way that they fulfill the condition $\alpha_i^{||} = \alpha_f^{||}$. If the crystalline domains within the film are, however, not randomly oriented the azimuthal angle has to be adjusted for every 2θ additionally to fulfill $\alpha_i^{||} = \alpha_f^{||}$ for

all sets of lattice planes. In order to achieve this, the sample is rotated around the surface normal.
In GIXD, it is convenient to plot the scattered intensity against the in-plane component $q_{||}$ of the wavevector transfer $\mathbf{q}$.

3.2.4 MS Beamline at the Paul-Scherrer Institut (PSI)

Some of the time-resolved X-ray scattering experiments of this thesis shown in chapter 4 have been performed at the Material Science (MS) Beamline at the Swiss Light Source (SLS) on the campus of the Paul-Scherrer Institut (PSI) in Villigen. The Swiss Light Source is a third-generation synchrotron light source. The SLS storage ring is operated at an energy of 2.4 GeV. The MS beamline consists of a cryogenically cooled, permanent-magnet undulator, an X-ray optics hutch and two experimental endstations. One endstation is optimized for powder diffraction (EH1) and the other one that has been used for some of the measurements presented in this thesis is optimized for *in situ* surface diffraction (EH2). The experimental station of EH2 is

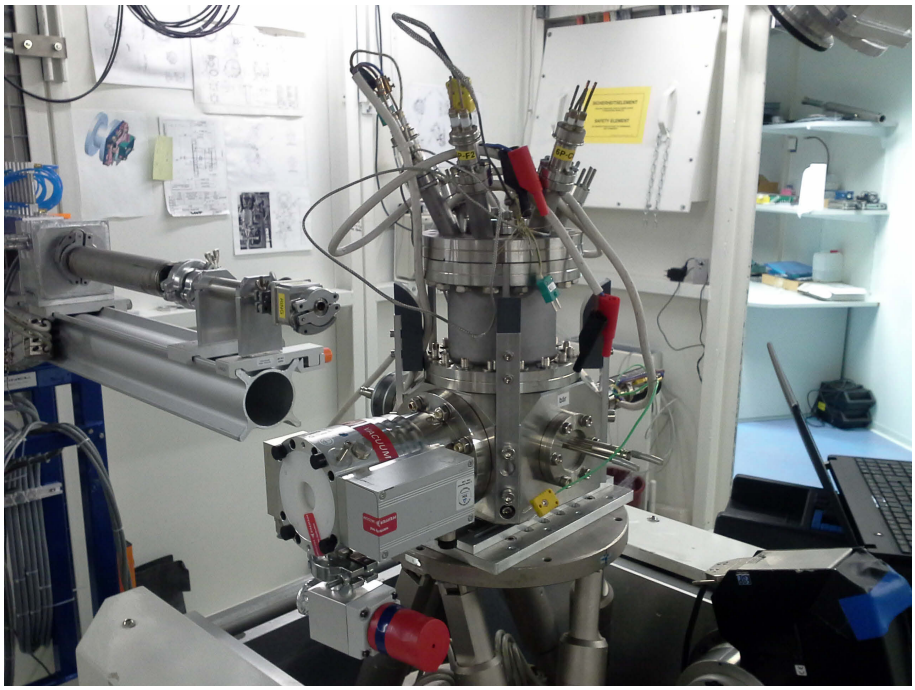

Figure 3.12: Portable vacuum chamber mounted on the hexapod in the surface diffraction hutch (EH2) at SLS.

equipped with a Micro-Controle Newport 2+3-circle surface diffractometer and a hexapod for precise sample alignment. [152] As X-ray detector, a PILATUS II was used. The PILATUS II has a size of 486×195 pixels. For the experiments presented in this thesis, a beam size of about 500×100 μm was used. Figure 3.12 shows the

experimental setup with X-ray beam exit (left), vacuum chamber and hexapod.

3.2.5 ID03 Beamline at the European Synchrotron Radiation Facility (ESRF)

Part of the work presented in chapter 5 has been performed at the ID03 surface diffraction beamline at the European Synchrotron Radiation Facility (ESRF) in Grenoble (France). The beamline is equipped with three undulators providing a photon flux of more than 10^{13} in the range between 5 keV and 24 keV and with a liquid nitrogen cooled Si(111) monochromator. The sample positioning system is a hexapod on which our portable UHV chamber was mounted.

3.3 Differential reflectance spectroscopy (DRS)

Optical Spectroscopy allows one to study the interaction between matter and electromagnetic radiation. In spectroscopy, the transmitted or reflected intensity is measured as a function of energy, which is in contrast to X-ray scattering techniques, where the scattered intensity is measured as a function of the scattering angle. There is a wide range of different spectroscopic methods that each serve a different purpose. Some common examples are NMR-, IR-, UV/Vis-, Fluorescence- and Raman, UPS and XPS-spectroscopy. Depending on the used energy range, one can extract atomic, molecular or inter-molecular information from samples. UV/Vis spectroscopy in particular is ideally suited to study molecular switches because, typically, the different isomers have unique absorption spectra. A simple way to measure the absorption spectrum of a material is to put a sample of the material into a parallel beam of white light and to compare the transmitted intensity with and without the sample. The extinction E_λ is related to the extinction coefficient ϵ_λ, to the thickness d and to the concentration c of the material via the *Beer-Lambert law*:

$$E_\lambda = lg(\frac{I_0}{I}) = \epsilon_\lambda \cdot c \cdot d \tag{3.26}$$

where I is the transmitted intensity behind the sample and I_0 is the intensity received by that sample. If the investigated sample is a thin film on a non-transparent substrate, it is more convenient to measure the reflected light intensity instead of the transmitted light intensity. In the following, it is shown how the reflectance of a thin film is related to the electromagnetic properties of the substrate and thin film material.

3.3.1 Measuring the absorbance of a thin film with reflectance spectroscopy

The optical properties of nonmagnetic materials can be expressed in terms of the dielectric function $\epsilon = \epsilon' + i\epsilon''$. Note that for non-isotropic materials, ϵ_1 and ϵ_2 are vectors with three components. The dielectric function is related to the complex refractive index of the material $N = n + ik$ via $N = \sqrt{\epsilon}$. The real part describes the dispersion of light, whereas the imaginary part describes the absorption of light. The dispersion and absorption properties of a material are not independent from each other. They can be converted into each other via the *Kramers-Kronig* relations:

$$\epsilon'(\omega) = 1 + \frac{2}{\pi} \cdot P \int_0^\infty \frac{\omega' \cdot \epsilon''(\omega')}{\omega'^2 - \omega^2} d\omega'^2 \tag{3.27}$$

In many cases, it is sufficient to know $\epsilon''(\omega)$ in a finite range around the ω in question, under the assumption that ϵ'' is small close to the boundaries. The contribution of additional resonances in the far UV-region can often be neglected as the contribution of ϵ'' to ϵ' scales with $\frac{\omega'}{\omega'^2-\omega^2}$

If the electromagnetic properties of a thin film and the underlying substrate are known, one can calculate the reflectance of the system using the so called Fresnel equations. The incoming light is regarded as a plane electromagnetic wave with wavevector $\mathbf{k}$ and photon energy $\hbar\omega$:

$$\mathbf{E}(\mathbf{r},t) = E^0 e^{i(\omega t - \mathbf{k}\cdot\mathbf{r})}. \tag{3.28}$$

The polarisation of a wave whose plane of incidence is defined by its wavevector $\mathbf{k}$ and the surface normal $\mathbf{n}$ is separated in two components: The part of the electric field that is perpendicular to the plane of incidence (s-polarization) and the part that is parallel to the plane of incidence (p-polarization) (see Figure 3.13a).

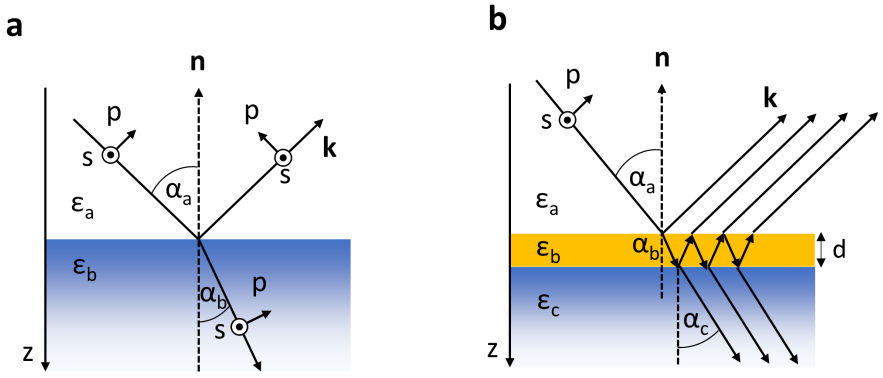

Figure 3.13: (a) Illustration of a plane wave being reflected and transmitted at an interface between two media, characterized by dielectric functions ϵ_a and ϵ_b. (b) Reflection and transmission for a three phase system.

The Fresnel coefficients for reflection for p-polarization and s-polarization are defined as:

$$r_{p/s} = \frac{E^r_{p/s}}{E^0_{p/s}} \tag{3.29}$$

where E^0 denotes the amplitude of the incoming electric field and E^r is the reflected amplitude with the respective polarization. The coefficient $r_{p/s}$ depends not only on the dielectric function of the media but also on the angle of incidence α_a.

$$r_p = \frac{\sqrt{\epsilon_b}\cos\,\alpha_a - \sqrt{\epsilon_a}\cos\,\alpha_b}{\sqrt{\epsilon_b}\cos\,\alpha_a + \sqrt{\epsilon_a}\cos\,\alpha_b} \text{ and } r_s = \frac{\sqrt{\epsilon_a}\cos\,\alpha_a - \sqrt{\epsilon_b}\cos\,\alpha_b}{\sqrt{\epsilon_a}\cos\,\alpha_a + \sqrt{\epsilon_b}\cos\,\alpha_b}. \tag{3.30}$$

The reflectivity R of the interface is defined as

$$R_{p/s} = \frac{I^r_{p/s}}{I^0_{p/s}} = \left| r_{p/s} \right|^2 . \tag{3.31}$$

For all measurements that are presented in this thesis, the angle of incidence was zero (normal incidence). In this case, all the cosine terms in eq. 3.30 become unity and $R_p = R_s$.

So far, only the case of a two-phase system with a single interface has been considered. However, a thin film on top of a substrate has to be treated as a three-phase system with three dielectric functions $(\epsilon_a, \epsilon_b, \epsilon_c)$. The resulting film thickness dependent reflectivity $R(d)$ takes a rather complicated form, but a simple approximation can be made for the case of very thin films with $(d << \lambda)$, which is true for the organic thin films that are studied in this thesis. One can show (see ref. [153]) that the differential reflectance $\frac{R(d)-R(0)}{R(0)}$, that is, the normed difference between reflectance with the thin film and the reflectance of the bare substrate without the film, can be written as:

$$\frac{R(d) - R(0)}{R(0)} \approx \frac{8\pi d n_1}{\lambda} \mathrm{Im}(\frac{\epsilon_b - \epsilon_c}{\epsilon_a - \epsilon_c}) = -\frac{8\pi d n_1}{\lambda} \mathrm{Im}(\frac{\epsilon_a - \epsilon_b}{\epsilon_a - \epsilon_c}) \tag{3.32}$$

where ϵ_a denotes the dielectric function of the ambient medium, typically air or vacuum, in which case ϵ_a is real. ϵ_b and ϵ_c denote the dielectric functions of the thin film and the substrate, respectively (see Figure 3.13b. Thus, for a fixed wavelength there is a direct relation between the differential reflectance and the dielectric function of the thin film. The right side of eq. 3.32 can be separated into the real and imaginary part of the dielectric function of the thin film:

$$\frac{R(d) - R(0)}{R(0)} \approx -\frac{8\pi d}{\lambda} (A \cdot \epsilon''_b + B \cdot [\epsilon'_b - 1]). \tag{3.33}$$

The parameters A and B only depend on the optical properties of the underlying substrate:

$$A = \frac{1 - \epsilon'_c}{(1 - \epsilon'_c)^2 + (\epsilon''_c)^2} \tag{3.34}$$

$$B = \frac{\epsilon''_c}{(1 - \epsilon'_c)^2 + (\epsilon''_c)^2} \tag{3.35}$$

For $|B| << |A|$, that is, if the substrate is transparent in the investigated energy

range, eq. 3.33 can be further simplified to give

$$\frac{R(d) - R(0)}{R(0)} \approx -\frac{8\pi d}{\lambda} A \cdot \epsilon_b''. \tag{3.36}$$

Thus, for transparent substrates, such as fused silica, the differential reflectance is directly proportional to the imaginary part ϵ_b'' of the thin film. Note that the above used approximation is only valid for semi-infinite substrates.

3.3.2 Transfer-matrix method

For the case of an organic thin film on a non-transparent substrate, such as silicon or gold, the reflectance of the corresponding multilayer system can be calculated using the so called *transfer-matrix method*. [154] The transfer-matrix method allows one to simulate the propagation of an electromagnetic plane wave through a multilayer systems with more than one reflecting interface. The layered system is represented as a matrix which is the product of the matrices of individual layers. The transfer-matrix formalism can be applied to several scenarios and systems, including incidence at a finite angle, magnetic and absorbing materials. The Parratt Formalism for the simulation of the X-ray reflectivity of multilayer systems, that has been described in an earlier section, is also based on the transfer-matrix method. [151]
Here, we present the case of normal incidence with respect to the surface of the multilayer system (parallel to the z-axis). The field within a each layer can be written as the superposition of left- and right-traveling waves with wave number k:

$$E(z) = E_r e^{ikz} + E_l e^{-ikz} \tag{3.37}$$

The electromagnetic field can be written in the form of a vector $(E(z), F(z))$ where F denotes the derivation of the electric field

$$F = \frac{dE}{dz} = ikE_r e^{ikz} - ikE_l e^{-ikz}. \tag{3.38}$$

From Maxwell's equation follows that both $E(z)$ and $F(z)$ are continuous across a boundary.

Consequently, the propagation of the vector $(E(z), F(z))$ over a distance d can be written in the form of a matrix operation

$$\begin{pmatrix} E(z+d) \\ F(z+d) \end{pmatrix} = M \cdot \begin{pmatrix} E(z) \\ F(z) \end{pmatrix} \tag{3.39}$$

with

$$M = \begin{pmatrix} \cos\, kd & \frac{1}{k} \sin\, kd \\ -k \sin\, kd & \cos\, kd \end{pmatrix} \tag{3.40}$$

Eq. 3.40 describes the propagation of an electromagnetic wave through a layer with thickness d, where the plane wave has the wavenumber k. A system with N layers can be treated analogously. The system transfer-matrix in this case becomes

$$M_s = M_N \cdot \ ... \ \cdot M_2 \cdot M_1 \tag{3.41}$$

with M_i denoting the transfer matrices of the individual layers and i increasing towards higher z values.
Knowledge of the system transfer-matrix makes it possible to calculate the reflectance and transmittance of the system. If $z = 0$ marks the surface of the layered system, then the field E_{out} with wave number k_{out} outside of the layered structure ($z < 0$) is described as

$$E_{out}(z) = E_0 e^{ik_{out}z} + rE_0 e^{-ik_{out}z}. \tag{3.42}$$

Here, E_0 denotes the amplitude of the incoming wave and r is the amplitude reflectance coefficient. Inside the system ($z \geq 0$), the field has the form

$$E_{in}(z) = tE_0 e^{ik_{in}z} \tag{3.43}$$

with t being the amplitude transmittance and k_{in} denoting the wave number within the system. Solving the equation

$$\begin{pmatrix} E_{in}(0) \\ F_{in}(0) \end{pmatrix} = M \cdot \begin{pmatrix} E_{out}(0) \\ F_{out}(0) \end{pmatrix} \tag{3.44}$$

yields

$$t = 2ik_{out}e^{-ik_{in}d} \left[\frac{M_{11}M_{22} - M_{12}M_{21}}{-M_{21} + k_{out}k_{in}M_{12} + i(k_{in}M_{11} + k_{out}M_{22}} \right] \tag{3.45}$$

and

$$r = \left[\frac{(M_{21} + k_{out}k_{in}M_{12}) + i(k_{out}M_{22} - k_{in}M_{11})}{(-M_{21} + k_{out}k_{in}M_{12}) + i(k_{out}M_{22} + k_{in}M_{11})} \right] \tag{3.46}$$

The more easily measurable quantities T and R that describe the intensity reflectance and transmittance can then be calculated using $T = |t|^2$ and $R = |r|^2$.

3.3.3 Monitoring the switching process of molecular switches with DRS

If two isomers of molecular switches have different absorption spectra, which is the case for most azobenzene derivatives, optical absorption measurements are a well-suited tool to monitor the switching process. Since the optical reflectance of a thin film is related to the optical absorption, it is possible to monitor the switching process with reflectance spectroscopy. Performing material specific simulations based on the transfer-matrix method, it can be shown that for specific regions of the photon energy the optical reflectivity $R(d)$ of a system, consisting of a substrate and an organic thin film on top, has (to a good approximation) a linear dependence on the change of the extinction coefficient k.

$$\Delta R \propto \Delta k. \tag{3.47}$$

Since the extinction coefficient k is related to the attenuation coefficient α via $\alpha = \frac{4\pi k}{\lambda}$, the change of the reflectivity in these regions of the photon energy is proportional to the relative change of the attenuation coefficient α.

$$\Delta R \propto \Delta \alpha. \tag{3.48}$$

As a consequence, ΔR also has a linear dependence on the concentration of the $E-$ or $Z-$ isomer, respectively.

$$\Delta R \propto \Delta E \text{ and } \Delta R \propto \Delta Z. \tag{3.49}$$

In chapter 6, we use this linear dependence for a detailed investigation of the switching kinetics of azobenzenes in nanofibers.

Most of the real-time switching experiments that are presented in this thesis have been performed in a specially designed high vacuum chamber (see Figure 3.14a). The chamber can be equipped with a Beryllium window that is transparent for X-rays. Also, there are several fused silica windows in the top flange which allow for optical access. The top windows can be used for irradiation of the sample with UV- or visible light. A larger window at the central position directly above the sample can be used for DRS measurements with a two-channel reflection fiber probe (see Figure 3.14b). Optionally, a four-leg fiber bundle with an additional reference leg can be equipped that connects the Xenon lamp with a second spectrometer. In this way, any long-time intensity fluctuations of the Xenon lamp can be monitored and

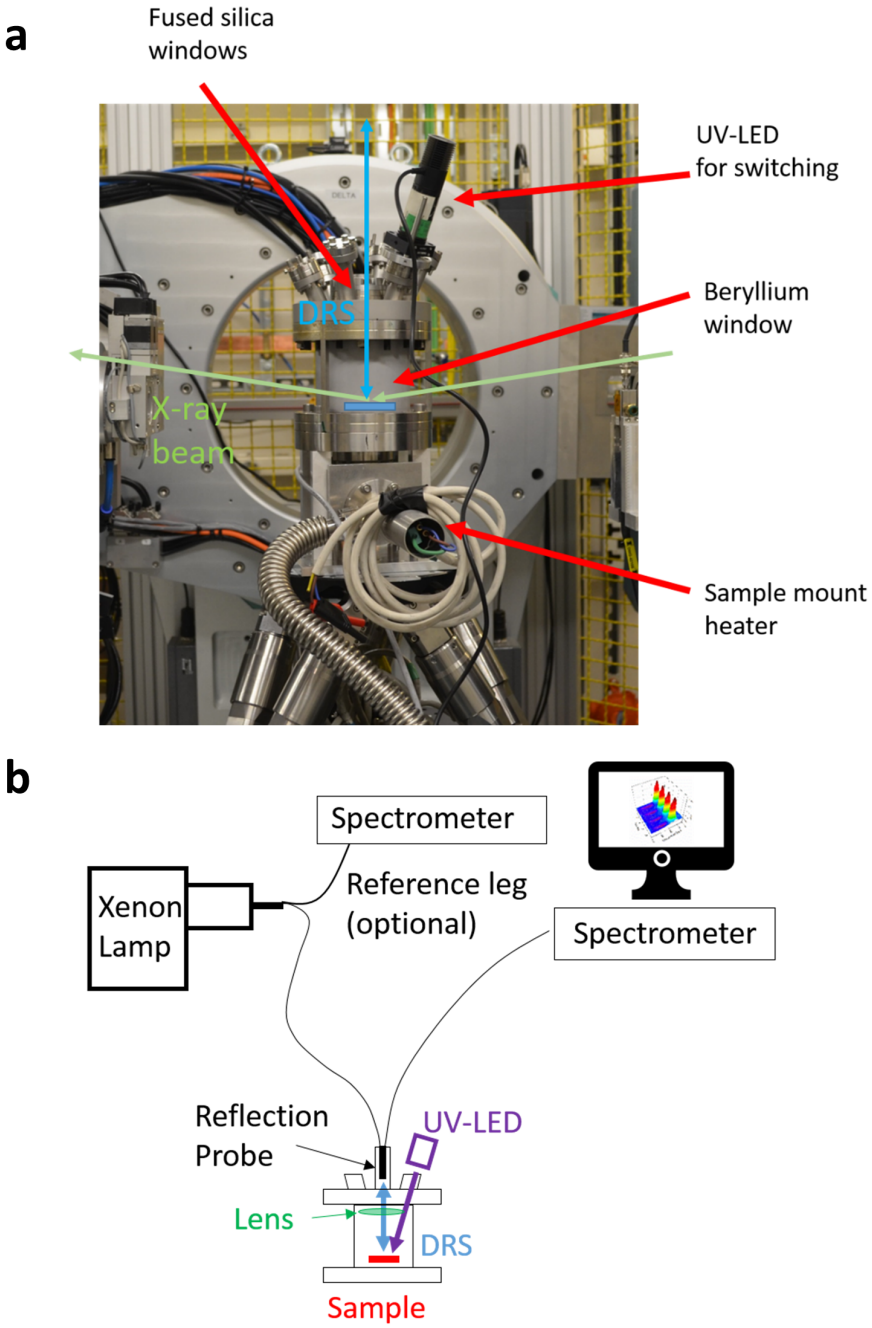

Figure 3.14: (a) The high vacuum chamber that has been designed in this thesis, optimized for inducing and monitoring photoisomerization in real-time and (b) scheme of the reflection probe setup that has been used for real-time DRS measurements

corrected in the data evaluation process. This second setup has been used for the long-time *in situ* measurements that are presented in chapter 4. For measurements that take less than an hour, the long time fluctuations of the Xenon lamp do not play a role. The short time fluctuations of the output of the Xenon lamp $I(t)/I_0$ are typically in the order of 10^{-5}. Spectral fluctuations of the Xe-lamp output have not been observed.

3.4 Spin-coating

Spin-coating is a technique that allows to easily prepare thin films of soluble small molecules, polymers or inorganic materials on a flat substrate. It is intensively used for photolithography and other microfabrication processes. But it can also be used to coat larger objects, such as flat panel TV displays. [155] The basic principle of spin-coating is shown in Figure 3.15. The substrate is put on a rotation stage and fixated via a small vacuum pump. A drop of solution is given onto the spinning substrate (dynamic dispense) or onto the resting substrate that is set to rotation a few seconds later (static dispense). As a result, the coating material is spread across the substrate by centrifugal force. During this process, the solvent evaporates and only the desired material is left on the substrate. The centrifugal force in combination with the surface tension of the solution leads to an even covering of the substrate. The thickness and morphology of the film can be influenced by parameters such as the rotation speed, the solution concentration and the viscosity of the solvent. [156, 157] A higher rotation speed or lower concentration of the solution usually leads to thinner films. In general, the dependency of the film thickness on

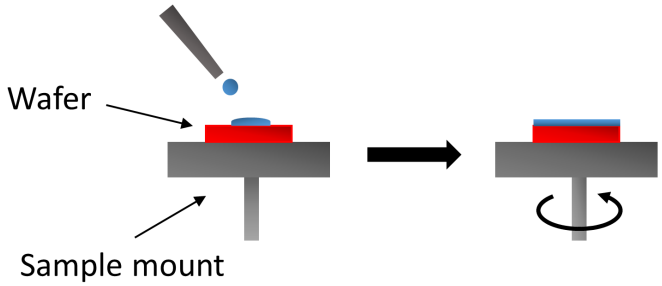

Figure 3.15: Sketch showing the typical spin-coating procedure.

the rotation speed for a spin coated film is given by the formula

$$t \propto \frac{1}{\sqrt{\omega}} \tag{3.50}$$

where t is the thickness of the spin coated film and ω is the angular velocity of the substrate. The absolute film thickness, however, also depends on the material concentration and the solvent evaporation rate which is determined by the solvent viscosity, the vapor pressure, ambient temperature and humidity.

4 Light-controlled 'molecular zippers' based on azobenzene main chain polymers

In this chapter, the molecular structure and the switching process of main-chain azobenzene polymers in thin films are investigated. We show that in thin films, the azobenzene main chain polymer **P1** self-assembles into 'molecular zippers'. Molecular zippers are common in biological systems like DNA or proteins and can be defined as molecular structures where molecules are interlocked in two directions through non-covalent interactions, along the length of the zip and across it. [158, 159] We find that thin films of **P1** can be reversibly switched between a highly ordered state (closed zippers) and a less ordered, amorphous state (open zippers). We use real-time and *in situ* grazing incidence X-ray diffraction (GIXD) and UV-Vis differential reflectance spectroscopy (DRS) simultaneously to obtain information on both the photoisomerization of the azobenzene chromophores and the significant photoresponse of the molecular zippers. Our findings suggest that the observed complete amorphization of the film is induced by $E \rightarrow Z$ isomerization of about 20% of the azobenzene chromophores and that the ensemble kinetics of the $E \rightarrow Z$ isomerization is about 18 times faster than the kinetics of the amorphization.

4.1 Motivation

In 2001, Finkelmann et al. showed that large reversible shape changes of azobenzene functionalized elastomers in solids can be generated optically. [160] Also in 2001, McGrath et al. reported the direct observation of light-induced structural reorganization within a solid monolayer of azobenzene-containing functionalized dendrimers. [161, 162] During the following years, a large variety of photomechanical responses has been found for polymers with azobenzene chromophores in the side chains. [163–167] Application ideas make use of the fact that light-induced collective or cooperative motions of azobenzenes at a molecular level can be amplified to

macroscopic scales, often via a photoinduced phase transition within the polymer film. For example, Ikeda and co-workers have used liquid crystalline thin films of azobenzene polymers to build light-driven motors, in which an isothermal transition from a liquid-crystalline to an isotropic state caused by $E \rightarrow Z$ isomerization of the azobenzene moieties acts as the driving force. [87, 168] All of these systems are

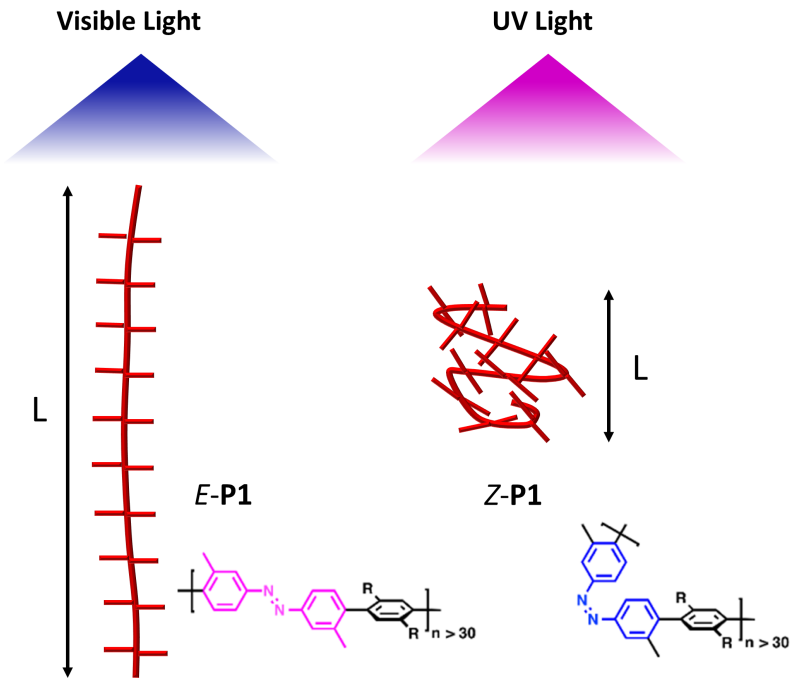

Figure 4.1: Chemical structure of *E*- and *Z*-**P1** (R = $n-C_{12}H_{25}$). UV-irradiation causes a reversible rod-coil transition of the polymer.

based on polymers with azobenzene in the side chains, which allows one to control the molecular structure of a polymer film indirectly via modifiying the interaction between adjacent polymers with light. However, polymers with molecular switches in the main chain allow for a more direct optical control over the molecular structure. [123, 169–175] Recently, Bléger et al. developed polymers with azobenzenes in the main chain and dodecyl side chains that enable a maximized photodeformation in solution [176] and allow for crawling motion on surfaces [177]. The rigid-rod polymer **P1** (see Figure 4.1) incorporates azobenzene chromophores in a poly(para-phenylene) backbone with two dodecyl side chains per repeat unit. A crucial aspect of the design is the presence of ortho-methyl groups and therefore introduction of large dihedral angles between the azobenzene units in order to decouple these units and break the electronic conjugation. This point ensures that a *Z*-rich photostationary state (PSS) can be reached upon irradiation with UV-light. [126] The azobenzene polymers can be switched from a thermodynamically stable linear and

elongated conformation where the azobenzenes are in the so called *E*-configuration to a compact and kinked conformation with azobenzenes in the *Z*-configuration. An important remaining question is, whether in an ordered thin film the polymer can still switch and whether molecular switching of the chromophores may trigger larger structural changes through coupling to neighboring polymers.

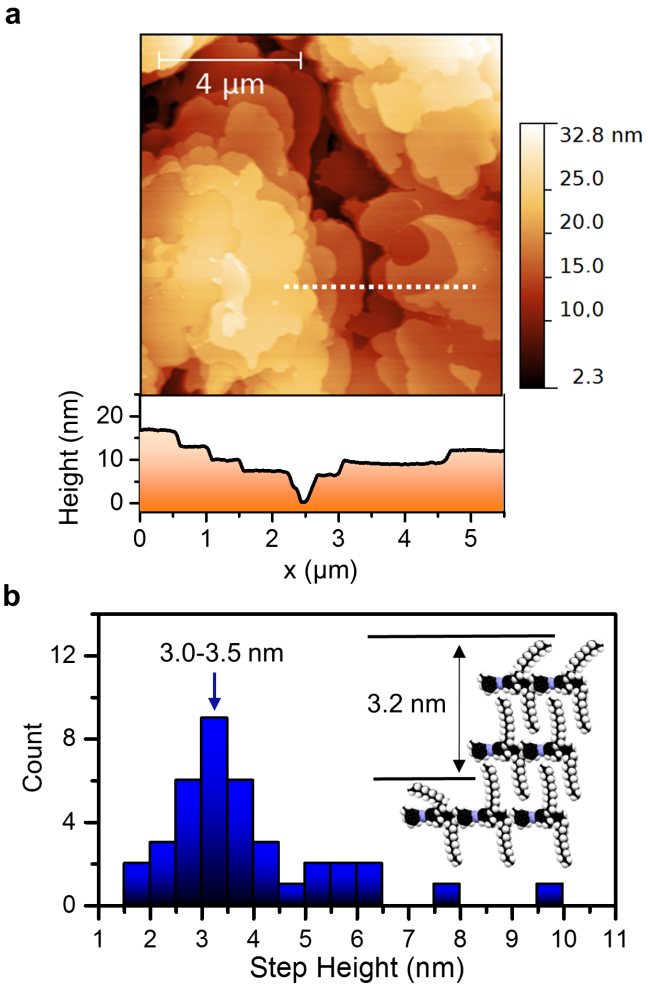

Figure 4.2: (a) AFM Image of a spin-casted **P1** film with height profile and (b) step height distribution.

4.2 Results

4.2.1 Layered island structure as revealed by microscopy

Samples of **P1**-polymers were spin-coated (1500 rpm) onto mica substrates from a 25 mg/ml toluene solution. AFM images of the main chain azobenzene polymer films show a homogeneous sample morphology, characterized by large islands with

diameters $> 1\ \mu m$ and several clearly distinguishable layers (Figure 4.2a). Large terraces with round step edges allow for further evaluation. A histogram of the step-height distribution is plotted in Figure 4.2b. The most frequently occurring step-height of 3.0-3.5 nm suggests a predominant edge-on orientation of the polymers with respect to the mica substrate. The inset of Figure 4.2b shows an illustration

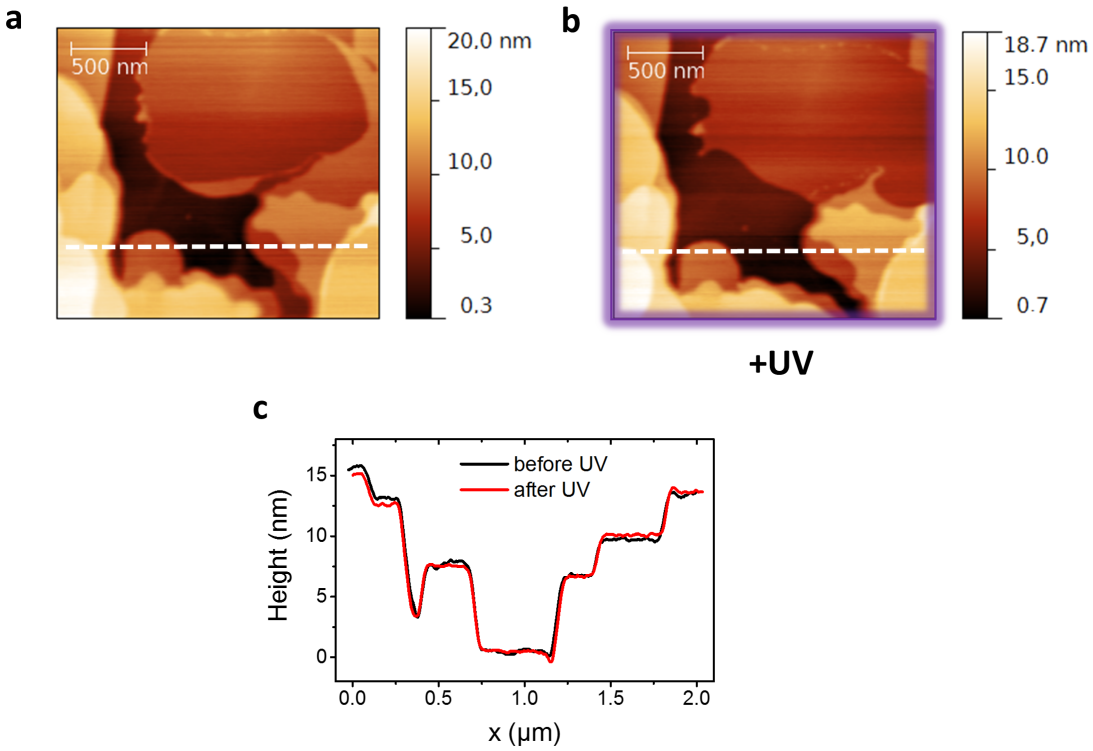

Figure 4.3: AFM images taken (a) before and (b) after 10 min irradiation with UV-light (91 mW/cm^2) and (c) comparison of height profiles taken along dotted white lines in (a) and (b) showing no significant and systematic changes due to exposure to UV-light.

of a stacking model involving interdigitation of dodecyl side chains that would be in agreement with the AFM data.

Irradiating the sample for 10 min with UV-light (91 mW/cm^2, 365 nm $\pm$ 5 nm) did not have a significant effect on the overall sample morphology (see Figure 4.3). Only locally some island shapes change slightly. X-ray reflectivity (XRR) measurements show no out-of-plane Bragg reflections of the polymer film (see Figure 4.4), which is in agreement with AFM, where the varying step heights also indicate the absence of a coherently ordered periodic layer structure perpendicular to the substrate surface.

This point requires some more explanation. In general a rather well defined layered structure such as it is shown in Figure 4.2 can have Bragg reflections that are visible in XRR. However, if the organic structure is very thin (<10 layers) and involves interdigitating layers, the modulation of the electron density along the z-axis might

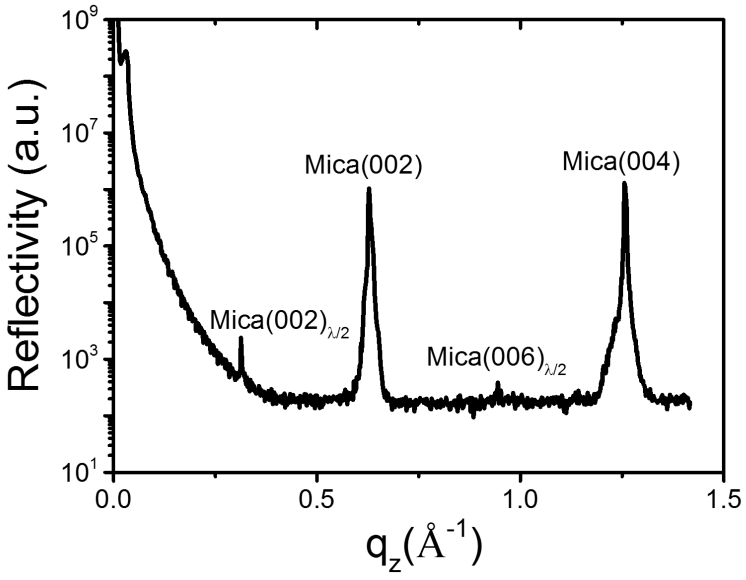

Figure 4.4: X-ray reflectivity of a spin-casted P1 thin film showing only Bragg peaks of the muscovite mica substrate. Peaks assigned with $\lambda/2$ are caused by the second harmonic of the 8 keV Cu-Kα radiation.

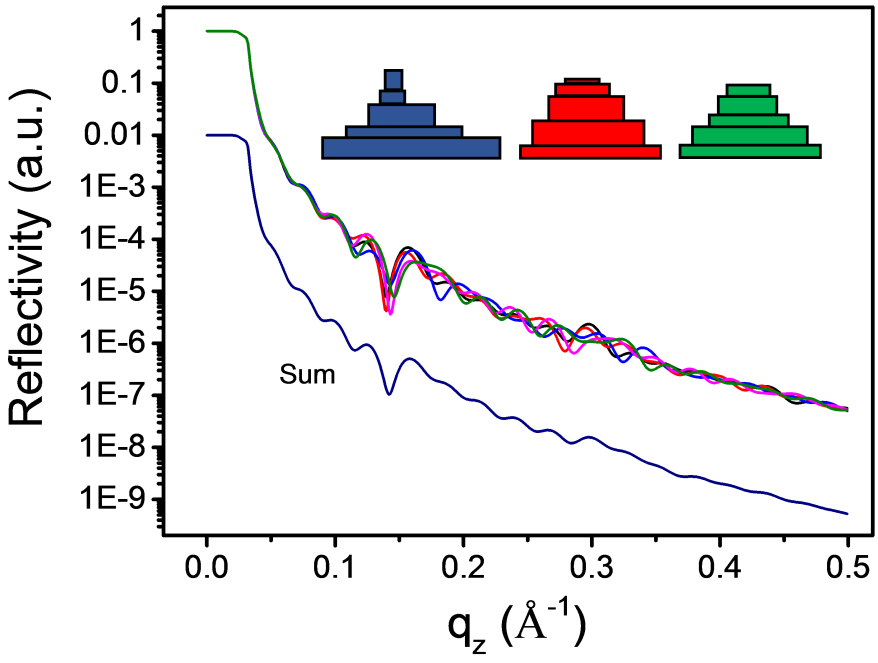

Figure 4.5: Influence of the distribution of lattice spacings on the X-ray reflectivity, demonstrated with simulations using Parratt's formalism. A XRR measurement will give the sum over many XRR curves corresponding to many different islands and therefore show no strong out-of-plane Bragg reflection.

be rather weak and the resulting scattering features might therefore be suppressed. A second explanation for the absence of Bragg reflections in the XRR is related to the step height distribution measured with AFM. Figure 4.2b shows that there is not a single defined step height in the film but rather a distribution of different step heights, ranging from 2.7 nm up to about 3.7 nm, which is a larger spread of lattice spacings than typically observed for organic thin films. One explanation for this could be that the extent of interdigitation of the alkyl side chains varies from spot to spot, which could cause such a distribution of lattice spacings. Since (at least for our laboratory X-ray source where the XRR measurements were taken) our X-ray spot size exceeds the coherence length of the X-ray beam by far, we effectively measure the sum of all the different X-ray scattering signals, corresponding to islands with a different layering. In the sum, the Bragg reflections and Laue fringes of the single islands can superimpose each other and therefore be smeared out. We performed some simulations using the Parratt formalism. Figure 4.5 shows the simulated XRR at different sample spots corresponding to different step heights. The input parameters are based on values obtained from AFM images. One can see that already a small number of interfering layer structures that all have the same average layer thickness but a different step height distribution can cancel out the Kiessig and Laue fringes of the "single" islands.

4.2.2 Light controlled molecular interdigitation as shown by X-ray diffraction

To investigate the initial molecular structure within the film and the UV light induced structural changes, we used time-resolved Grazing Incidence X-ray Diffraction (GIXD). X-ray diffraction is sensitive to coherently ordered molecular crystals and thus presents a powerful technique to address the isomerization of molecular switches in domains with long range ordering. [178–180] The black curve in Figure 4.6a shows a GIXD scan of a **P1** thin film before the very first UV-irradiation. Plotted is the scattered X-ray intensity as a function of the in-plane wavevector transfer $q_{||} = 4\pi/\lambda \sin\theta$, where 2θ denotes the angle between primary and diffracted beam. There are three main diffraction features. The first in-plane scattering feature appears at a wavevector transfer $q_{||} = 0.42$ Å^{-1}, corresponding to an in-plane lattice spacing $d_{||} = \frac{2\pi}{q_{||}}$ of 1.5 nm. Referring to earlier X-ray diffraction studies of rigid rod polymers with long alkyl side chains, we tentatively assign this peak to the packing structure of the polymer main chain. [181] In Figure 4.6a, the position and relative strength of two in-plane Bragg reflections at $q_{||} = 1.52$ Å^{-1}($d_{||} = 4.13$ Å) and $q_{||} = 1.69$ Å^{-1}($d_{||} = 3.72$ Å) resemble the in-plane scattering features of the thin

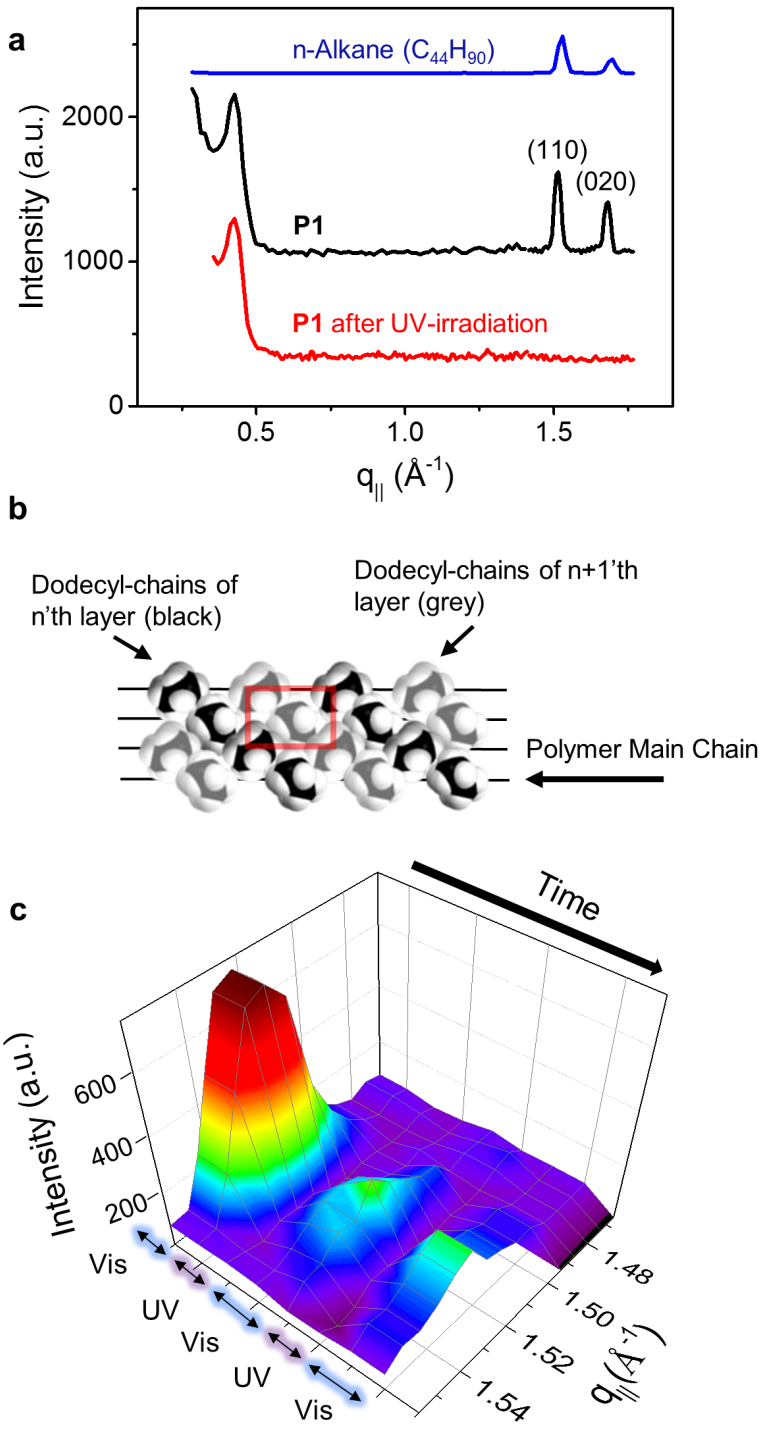

Figure 4.6: (a) GIXD scan of a **P1** thin film before (black) and after (red) UV-irradiation. For comparison the scattering signal of $n - C_{44}H_{90}$ (blue) is also shown. (b) Illustration of the proposed in-plane unit cell of the $C_{12}H_{25}$ side-chains (top view). (c) GIXD scans of the (110) Bragg peak of the sample before the very first UV-irradiation and during two irradiation cycles with UV light and visible light.

film structure of long n-alkanes like $C_{44}H_{90}$ (blue curve), where the *n*-alkane chains align nearly perpendicular to the substrate surface. [139, 182, 183] The large spacing of 1.5 nm between two dodecyl-chains along the polymeric backbone in the stretched out *E*-rich conformation prevents a single layer of **P1** from mimicing the *n*-alkane thin film structure (see Figure 4.6b). However, if the dodecyl side-chains of the n-th layer are allowed to interdigitate with dodecyl-chains from the n+1'th and n-1'th layer, the **P1** polymers can easily adopt the *n*-alkane thin film structure, since the inter-chain spacing of 1.5 nm along the polymeric backbone happens to be almost exactly twice as long as the longer axis of the *n*-alkane in-plane unit cell (0.74 nm). In fact, interdigitating dodecyl side-chains have been found in the case of comparable polymers with long dodecyl side chains such as poly(3-dodecylthiophene), poly[5,5'-bis(3-dodecyl-2-thienyl)-2,2'-bithiophene)] (PQT), poly(2,5-bis(3-alkylthiophene-2-yl)thieno[3,2-b]thiophene) (pBTTT) or poly(n-dodecyl acrylates). [135,136,184,185]

We checked for light-induced changes in the crystal structure with time-resolved GIXD. The red curve in Figure 4.6a shows the GIXD signal after the sample was exposed to UV-light with an intensity of 91 mW/cm^2, an energy of 3.4 eV and spread of 0.1 eV for 10 min. UV-irradiation leads to a comparatively small decrease of (10 ± 1) % of the intensity of the Bragg peak at $q_{||} = 0.42$ Å^{-1}, which we attribute to the main chain of the polymer. If most of the ordered azobenzenes within the film would switch, a stronger decrease or a shift of the scattering feature at $q_{||} = 0.42$ Å^{-1} would be expected. On the other hand, the in-plane Bragg reflections at $q_{||} = 1.52$ Å^{-1} and $q_{||} = 1.69$ Å^{-1} vanish after around 4 min of UV-light exposure (91 mW/cm^2 at 3.4 eV), indicating amorphization of the initially crystalline dodecyl side chains since no new Bragg reflections appear. We observed a slight temperature increase from 22°C to 24°C due to UV-light absorption of the substrate or the film. However, heating the sample up to 100°C did not significantly influence the crystal structure, so that the structural transition is indeed light-induced (and not due to local heating effects). From the thermal stability up to 100°C, we also conclude that the experiments were carried out far below the melting temperature of the (unswitched) azobenzene polymer thin film. Figure 4.6c provides a 3D plot showing GIXD scans of a **P1** thin film that were measured during 3 irradiation cycles. The GIXD measurement of the freshly prepared sample before the very first UV-irradiation shows a Bragg peak at $q_{||} = 1.52$ Å^{-1}. After 10 min of UV-irradiation, the peak vanishes, but it reappears if the sample is irradiated with visible light. While the structural recovery in the first switching cycle is not complete, we find that from the 2nd irradiation cycle on, the light-induced structural transition is almost completely reversible.

4.2.3 Kinetics of the *E*-*Z* isomerization as judged by optical spectroscopy

To investigate how the observed light-induced changes within the film are related to $E \rightarrow Z$ isomerization of azobenzenes, we performed UV-Vis spectroscopy in transmission and reflection geometry. A comparison of the optical transmittance of the sample before and after irradiation with UV-light is shown in Figure 4.7a. Upon UV-irradiation, the film absorbance between 3.2 eV and 4 eV corresponding to the absorption maximum of the *E*-isomer decreases by (19 ± 1) %.

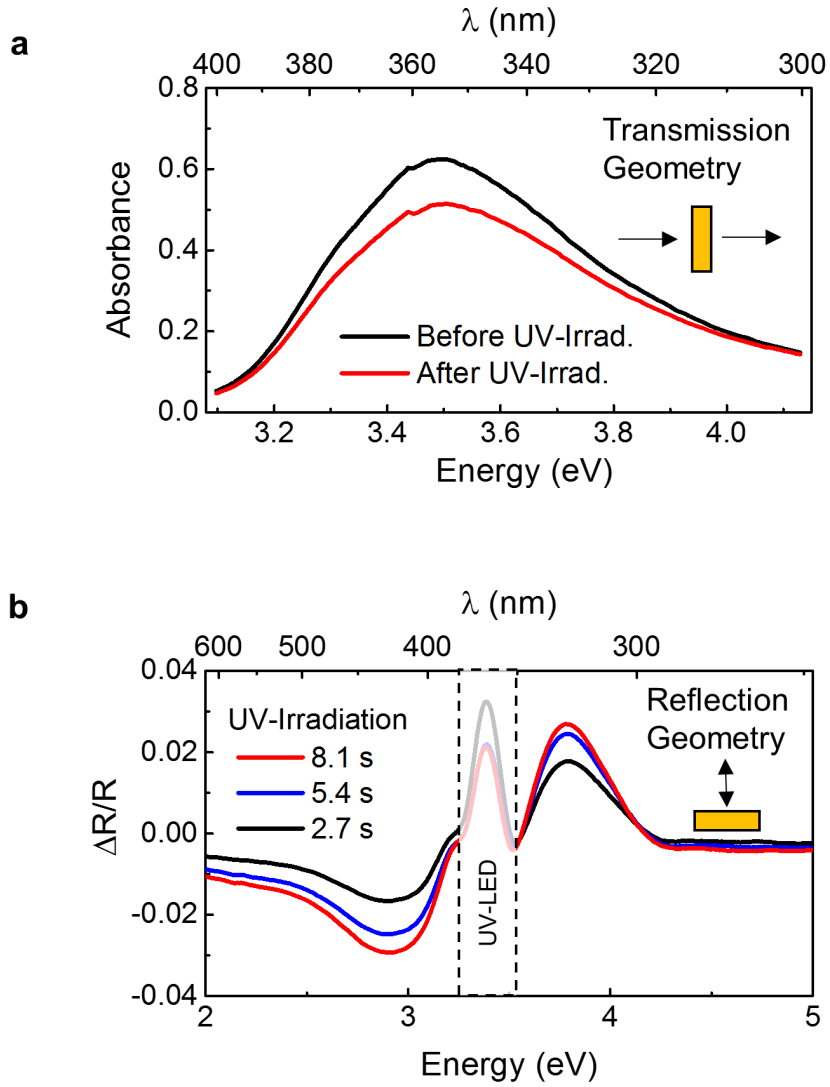

Figure 4.7: (a) Thin film absorbance at 3.5 eV before and after 5 min irradiation with UV-light (3.4 eV, 91 mW/cm^2). (b) DRS spectra during UV-irradiation showing the relative change of reflectivity due to $E \rightarrow Z$ isomerization of azobenzene chromophores.

We also prepared films with a different nominal thicknesses (1-25 nm) by varying the solution concentration (1 mg/mL to 25 mg/mL) to check if only azobenzene units close to the sample surface or close to the substrate surface can be switched; Both scenarios would lead to a thickness dependence of the fraction of azobenzenes that can be switched. However, no significant effect of the film thickness on the relative amount of switched azobenzenes has been found in this range (see Figure 4.8).

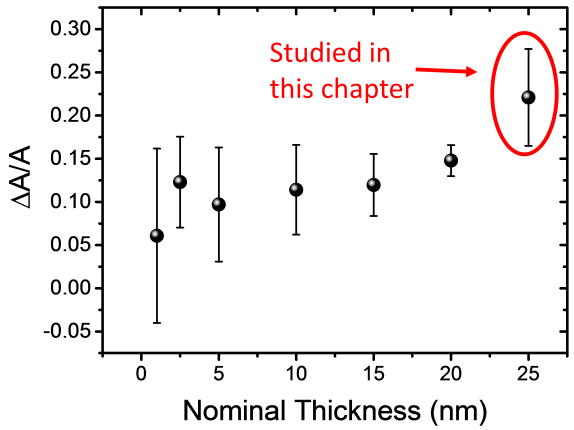

Figure 4.8: Relative change of the thin film absorbance at 350 nm after UV-irradiation plotted for different nominal film thicknesses (measurements performed by Tobias Liebig)

We find that from the 2nd switching cycle on, the spectral changes are almost completely reversible. Under the assumption that the ratio between *E*-isomer absorbance and *Z*-isomer absorbance at 3.5 eV does not significantly change when the polymers are in a thin film, we can give an estimation of the fraction of *Z*-isomers in the thin film after UV-irradiation. Another assumption we have to make is that the absorption of the polymer film in the region around 3.5 eV is dominated by the azobenzene moieties. This assumption is reasonable because neither the dodecyl nor the phenyl groups absorb in the region around 3.5 eV.

In ref. [176], Bléger et al. performed nuclear magnetic resonance (NMR) and optical absorption measurements of **P1** in solution. Using their results, one can estimate the relative absorption of the *Z* isomer at 3.5 eV. ^{1}H-NMR shows that after UV-irradiation there are 14 % E-isomers and 86 % *Z*-isomers in a **P1** solution sample. The optical absorbance of the same solution decreases under the same UV-irradiation conditions from 1 to about 0.2 at 3.5 eV. We can use this to calculate the relative absorbance of Z-isomers. 14 % E-isomers will contribute 0.14 to the absorbance of the switched solution. The remaining 0.06 absorbance of the switched

solution can be attributed to the absorbance of the 86 % Z-isomers at 3.5 eV. The relative absorbance of Z-isomers is then

$$A_Z^{3.5eV} = \frac{1}{0.86} \cdot 0.06 \cdot A_E^{3.5eV} \approx 0.07 \cdot A_E^{3.5eV}. \tag{4.1}$$

Thus, the absorbance of Z-azobenzene at 3.5 eV is about 14 times weaker than the absorbance of E-azobenzene at 3.5 eV. Under the assumption that the ratio between E-isomer absorbance and Z-isomer absorbance at 3.5 eV does not significantly change when the polymers are in a thin film, we can give an estimation of the fraction of Z-isomers in the thin film after UV-irradiation. Figure 4.7a shows that the absorbance of a **P1** thin film at 3.5 eV decreases by (19 ± 1) % upon UV-irradiation with respect to the dark state where all azobenzenes are in the E-conformation.

$$A_{UV}^{3.5eV} = 0.81 \cdot A_E^{3.5eV}. \tag{4.2}$$

Here $A_{UV}^{3.5eV}$ denotes the absorbance of the film after UV-irradiation and $A_E^{3.5eV}$ denotes the absorbance of the polymer film in the dark state. After UV-irradiation, the film contains a mixture of E-isomers and Z-isomers. Thus the measured absorbance after UV-irradiation can be written in the form of

$$A_{UV}^{3.5eV} = (1 - x) \cdot A_E^{3.5eV} + x \cdot A_Z^{3.5eV} \tag{4.3}$$

where x denotes the fraction of Z-isomers in the film after UV-irradiation. Using eq. 4.1 and 4.2 we can solve eq. 4.3 and find that $x = 0.204$. Therefore our optical absorbance measurements suggest that about (20 ± 1) % of all azobenzenes within the film are switched from E to Z. Apart from absorption spectroscopy in transmission geometry, one can also use differential reflectance spectroscopy (DRS) to monitor the photoisomerization process. Figure 4.7b shows the relative change of the optical reflectivity during UV-irradiation. It increases in the region between 3.5 eV and 4.2 eV corresponding to the energy gap of the $\pi - \pi*$ transition of E-azobenzene, while it decreases in the visible region between 2.5 eV and 3.2 eV, corresponding to the energy gap of the $n - \pi*$ transition of the Z-azobenzene. Note that due to interference effects, the peak positions in DRS (Figure 4.7b) are slightly shifted with respect to the peak positions in the measurements in transmission geometry (Figure 4.7a). This behavior proves that $E \rightarrow Z$ isomerization is indeed occurring within the polymer film. The sharp feature at 3.4 eV can be attributed to diffusely scattered light from the UV-LED that is used to induce $E \rightarrow Z$ isomerization.
We performed simultaneously *in situ* GIXD and DRS measurements to study the relation between the partial disordering of the initially highly ordered film and the

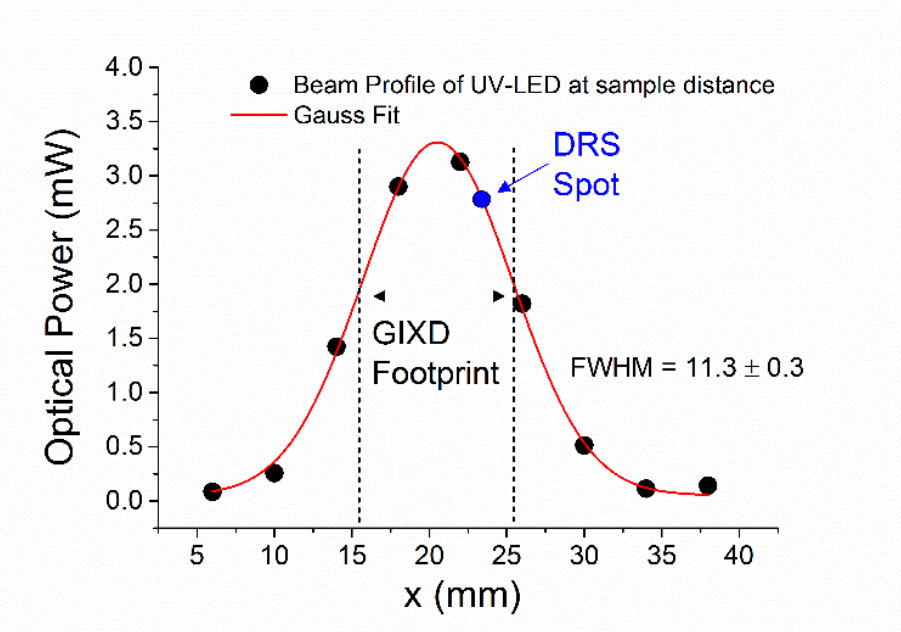

Figure 4.9: UV-light intensity distribution across the sample, together with the size of the GIXD footprint and the position of the DRS sample region.

$E \rightarrow Z$ isomerization of **P1**. To make GIXD and DRS measurements comparable, one has to make sure that both methods sample regions with comparable exposure to UV-light during the switching cycles. Figure 4.9 shows a plot of the light intensity of our UV-light source at the sample distance is shown. The FWHM of the Gaussian profile is slightly larger than the sample diameter. Thus at the very edge of the sample the light intensity is about 60 % of the light intensity in the middle of the sample. The 10×2 mm^2 GIXD footprint overlaps with the 2 mm^2 DRS spot. As can be seen in Figure 4.10a, both the optical reflectivity at 2.75 eV and the GIXD intensity at $q_{||} = 1.52$ Å^{-1} decrease upon UV-irradiation and increase again after the UV-light is switched off. Both the DRS and the GIXD intensity signals show a general decline after several switching cycles, possibly caused by drifts in room temperature that can lead to a slight misalignment in the optical and X-ray reflection geometry. Also, a physical process within the sample like photo-induced chromophore re-orientation [186] could lead to a reduction in DRS and GIXD signals. Further, a gradient in the intensity of the UV-light could cause mass transport within an azobenzene containing thin film [78] reducing the number of molecules in the sampled area. GIXD measurements with higher temporal resolution, taken at the SLS synchrotron source, show that the time to reach the photostationary state (PSS) differs drastically between DRS and GIXD measurements (see Figure 4.10b). For GIXD the scattered intensity is integrated along the vertical detector axis for a small interval around $q_{||} = 1.52$ Å^{-1} (see Figure 4.11).

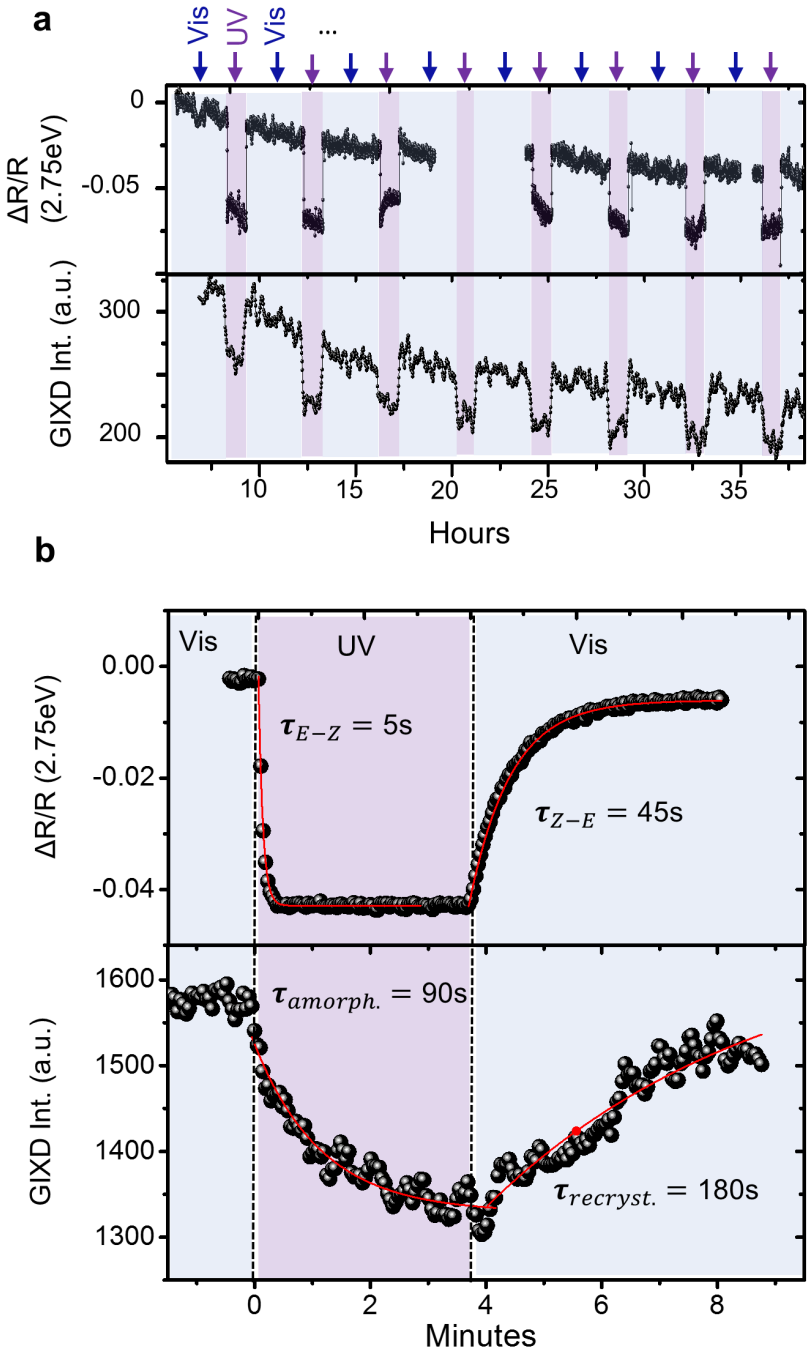

Figure 4.10: (a) Simultaneous DRS (top) and GIXD (bottom) during 9 switching cycles. UV irradiation induces $E \rightarrow Z$ isomerization of **P1** and amorphization of the alkyl side-chains. The $Z \rightarrow E$ isomerization and recrystallization is induced by the Xe lamp. (b) Comparison of the switching kinetics as determined by time-resolved DRS and GIXD under identical conditions but not simultaneously measured.

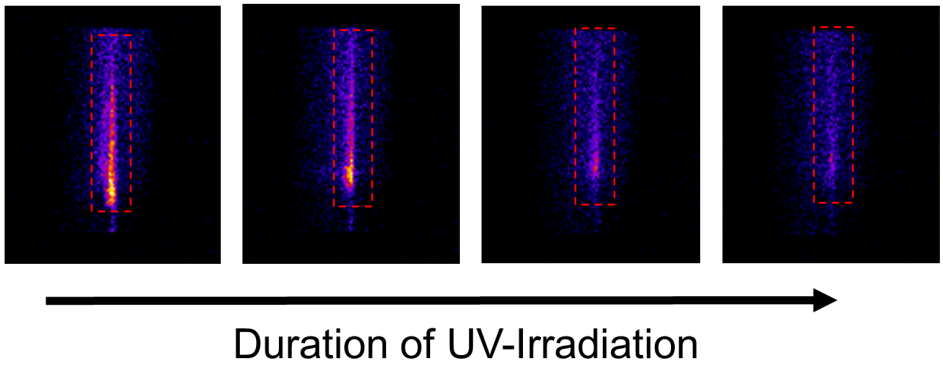

Figure 4.11: A series of 2D detector images taken at the strongest in-plane Bragg reflection ($q_{||} = 1.52$ Å^{-1}) during UV-irradiation. In time-resolved measurements, the integrated intensity in the region marked by red dotted lines is plotted.

In DRS, the PSS is reached with a time constant of $\tau = 5$ s. The red line is a monoexponential fit to the data. In the GIXD measurement, the PSS is reached with a time constant of $\tau = 90$ s under the same conditions. After the UV-light is switched off, the optical reflectivity returns back to its initial state with a time constant of $\tau = 45$ s, while the time constant of the recrystallization as monitored with GIXD is $\tau = 180$ s. Note that the $Z \rightarrow E$ isomerization is induced by visible light (< 3 eV) since the time-resolved optical measurements within a wide spectral range require constant irradiation with white light from a Xe-lamp. We found that the UV-intensity of the Xe-light had only a minor effect (ΔR/R at 3.5 eV = 0.5 %) on the $E \rightarrow Z$ isomerization compared to our UV-LED (ΔR/R at 3.5 eV $\approx$ 4 %). Therefore we can exclude that most azobenzenes were already in the Z-configuration before the UV-LED was switched on. Another point that has to be considered is that Figure 4.9 shows that the average UV-light intensity in the region sampled with GIXD is smaller than the UV-light intensity in the region sampled with DRS. It has been checked that the isomerization rate is proportional to the intensity of the UV-light. Since the UV-light intensities in the regions sampled with GIXD and DRS, respectively, only differ by less than a factor of 2, the observed difference of the time constants in GIXD and DRS (a factor of 18) can not be explained by the inhomogeneous irradiation of the sample with UV-light.

4.2.4 Discussion

Combining our results from GIXD and DRS, we can understand the switching mechanism in the layered thin films of the main chain azobenzene polymers. With GIXD

we find an interdigitating molecular zipper structure, in which UV-light induces amorphization of the dodecyl side-chains, corresponding to an opening of the molecular zippers. A comparison of the time-resolved GIXD and DRS measurements shows that the kinetics of this amorphization is more than one order of magnitude slower than the ensemble kinetics of the $E \rightarrow Z$ isomerization. Interestingly, we observe a fast monoexponential decay in the time-resolved DRS data. If the reason behind the slower kinetics of the amorphization was a slower switching mechanism of constrained azobenzenes in highly ordered domains coexisting with less ordered domains, one would expect a double exponential decay of the DRS data, because optical spectroscopy is sensitive to all azobenzene chromophores within the film. If a double exponential fit based on the two different time constants that were obtained with DRS and GIXD is applied to the DRS data, one finds that less than 0.6 % of all azobenzene chromophores within the film could switch with a slower time constant. From this, we conclude that a monoexponential decay describes the time-resolved DRS data with adequate accuracy and that the time constant of the amorphization is not primarily governed by the kinetics of the $E \rightarrow Z$ isomerization.

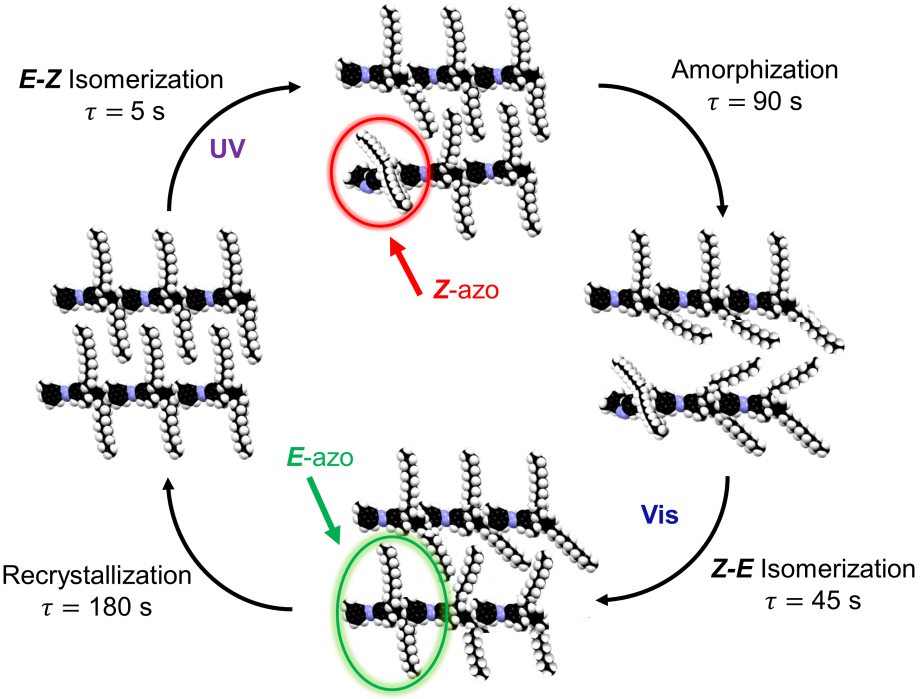

Figure 4.12: Sketch of the proposed switching scenario. Light-induced $E \rightarrow Z$ isomerization of azobenzene chromophores in the polymer main chain disrupts the coherent ordering of dodecyl side chains.

UV-Vis spectroscopy measurements of the optical absorbance of the polymer film showed that in the polymer film only a fraction (around 20%) of all azobenzenes

undergo $E \rightarrow Z$ isomerization. This is supported by GIXD measurements, where the Bragg reflection at $q_{||} = 0.42$ Å^{-1}, which we attribute to the ordering of the polymer main chain, decreases only slightly upon UV-irradiation, indicating that most of the ordered polymer main chains remain stretched out even after the side chains lost their coherent long range order. A scenario that could explain all of our experimental findings is illustrated in Figure 4.12. Strain and disorder generated by fast isomerization ($\tau = 5$ s) of a single azobenzene moiety, possibly close to a defect site or domain boundary slowly spreads throughout the film ($\tau = 90$ s), thereby disrupting the coherent ordering of the initially crystalline dodecyl side chains and ultimately leading to an amorphous structure of the film. After the UV-light is switched off, $Z \rightarrow E$ isomerization of the switched azobenzene moiety occurs ($\tau = 45$ s, triggered by the visible light of the Xe-lamp), followed by a slower recrystallization process of the dodecyl side chains ($\tau = 180$ s). Therefore, light-induced switching occurs rapidly at the local molecular level by $E \rightarrow Z$ and $Z \rightarrow E$ photoisomerization, and subsequent structural changes in the thin films are associated with longer time scales. A similar behavior has been observed for thin films of side chain azobenzene polymers, where the photochemically induced isomerization of azobenzene chromophores triggers a photoexpansion of the film. [187] The time constants of the photoexpansion and the mechanical relaxation were found to be considerably slower than the corresponding time constants of the azobenzene photoisomerization and the thermal back-reaction. The time constants of the amorphization and the recrystallization of the polymer film are primarily not governed by switching but by structural and topological constraints, such as chain stiffness, pinning of amorphous chains and the thickness distribution of lamellae. [188]

4.3 Conclusion

We have shown that it is possible to switch layered thin films of main chain azobenzene polymers reversibly between a highly ordered state involving interdigitating dodecyl side chains (closed zippers) and a significantly less ordered state with disordered side chains (open zippers). To our knowledge, this is the first demonstration of a rigid main chain polymer-based molecular zipper undergoing reversible light-controlled opening and closing. It is a remarkable result that fast $E \rightarrow Z$ isomerization ($\tau = 5$ s) of a small fraction (≈ 20 %) of all azobenzene chromophores within the polymer film is sufficient to disrupt the long range ordering of the protruding dodecyl side chains and to induce amorphization of the film. This amorphization occurs on a much larger timescale ($\tau = 90$ s), determined by structural and topo-

logical constraints. Our findings of a delay between azobenzene switching and the structural effects are important for optomechanically active or self-healing materials that make use of a reversible light-controlled phase transition.

5 Switching in molecular crystals

5.1 Motivation

In the last chapter, we demonstrated that it is possible to switch azobenzene polymers with alkyl side chains in thin multilayer films. In this system, the interdigitating alkyl sidechains formed crystalline nanodomains. However, as typical for polymeric systems, the long range order within the samples is limited. No higher order Bragg reflections and no coherent out-of-plane ordering have been found. Therefore, the question whether linear multiazobenzene compounds can be switched in highly crystalline environments is not answered, yet. Films consisting of smaller organic molecules can exhibit a higher crystallinity than polymeric films. Over the last decade, highly crystalline organic thin films were made for optoelectronic applications using organic semiconductors like, for example, pentacene [189], diindenoperylene [190] or PTCDA [191]. More recently, it has been shown by Koshima and others that molecular switches can form molecular crystals, too, and that some of them remain switchable even in highly crystalline environments. [192–195]. In 2015, Uchida *et al.* demonstrated that single crystalline azobenzene compounds can be used to build macroscopic crystals that can move across surfaces upon irradiation with light. [196] They used the fact that the crystallinity of their azobenzene crystals can be switched off and on reversibly with light. This effect is also known as photoinduced crystal melt transition (PCMT). [178] Therefore, it is an interesting question if multiazobenzene compounds can also be switched in highly crystalline environments and how the photoisomerization kinetics of the azobenzene chromophores will be influenced by the surrounding crystal.

After the investigation of azobenzene main chain polymers, we focus on azobenzene trimers in this chapter. The molecular switch **T1** (see Figure 5.1) consists of three azobenzene chromophores that are electronically decoupled via large dihedral angles ($\approx 90°$) between the azobenzene units. [126] Note that, in contrast to **P1**, there is no phenyl-group separating the azobenzenes. *Tert*-butyl groups are attached to both ends of the azobenzene chain. The azobenzene in the middle is equipped with two dodecyl side chains at the *ortho*-position. In the following section, we

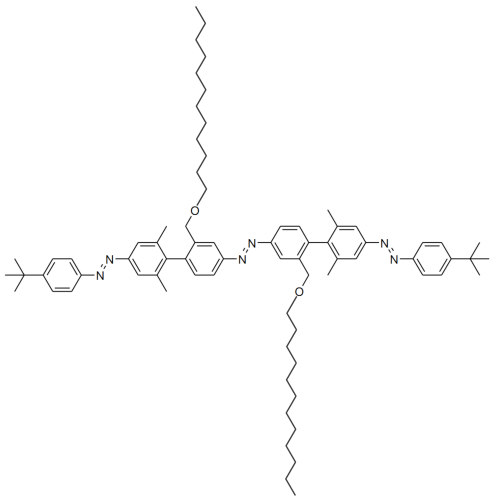

Figure 5.1: Chemical structure of the azobenzene trimer **T1** that is used in this study.

characterize the thin morphology of **T1** thin films that have been prepared via spin-coating using AFM. The molecular crystal structure is determined using XRR and GIXD. We study the azobenzene isomerization in the thin film with DRS and study light-induced structural changes using real-time GIXD.

5.2 Results

5.2.1 Film structure and morphology

Thin films of **T1** on SiO_2 were prepared via spin-coating, using a solution of 20 mg/mL **T1** in toluene. The solution drop was dispensed on the resting substrate which was set to rotation (60 rpm) 5 s after the dispensing step. Figure 5.2a shows a 10 x 10 µm^2 AFM image of a **T1** thin film. Many small crystallites with diameters of several hundred nm are visible. Figure 5.2b shows a 2 x 2 µm^2 AFM image with higher spatial resolution in which small holey structures within the crystallites become visible. In addition to AFM, also XRR has been performed to determine the film thickness, roughness and the electron density. Figure 5.3 shows the XRR plotted against the wave vector transfer q_z pointing along the surface normal. At lower q_z values, Kiessig fringes can be identified. A fit using the Parratt Algorithm [151] yields a nominal film thickness of 28.0 nm, a RMS roughness of 2.4 nm and an electron density of 0.2 $e^-/Å^3$. This electron density lies in the typical range of organic thin films (e.g., bulk PET has 0.3 $e^-/Å^3$).

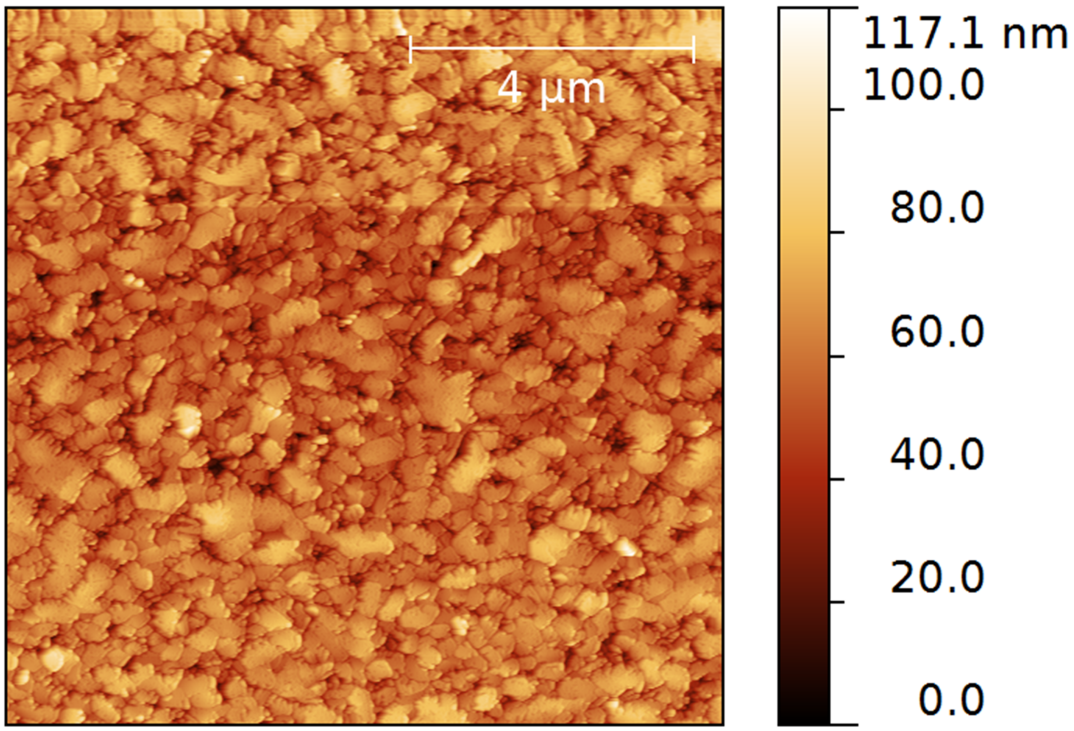

Figure 5.2: AFM images showing a 10 x 10 µm^2 region (a) and a 2 x 2 µm^2 region (b).

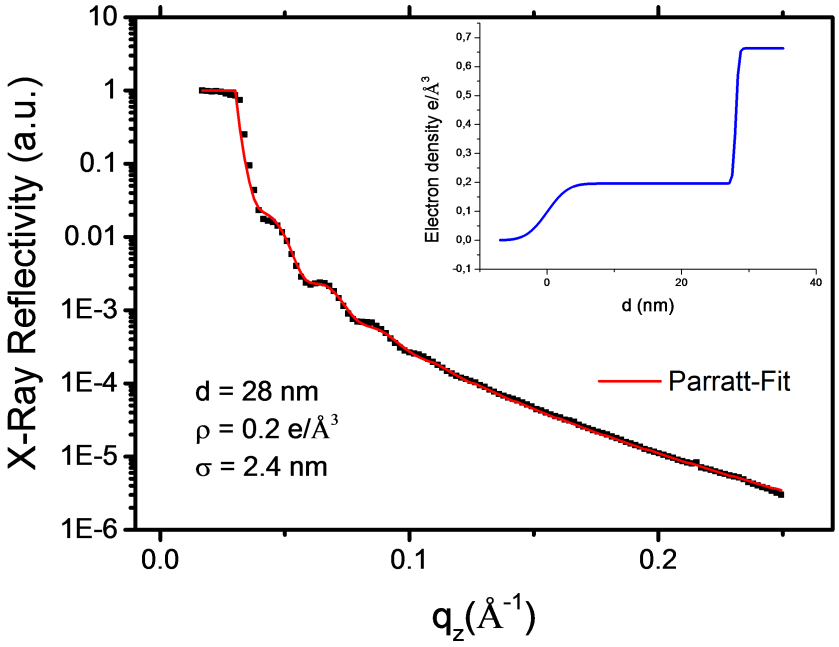

Figure 5.3: XRR scan of an azobenzene trimer sample on SiO_2.

AFM images showing many large island structures suggest that **T1** might form molecular crystals. Wide angle X-ray scattering has been performed for a detailed determination of the molecular crystal structure. Figure 5.4a shows a XRR measure-

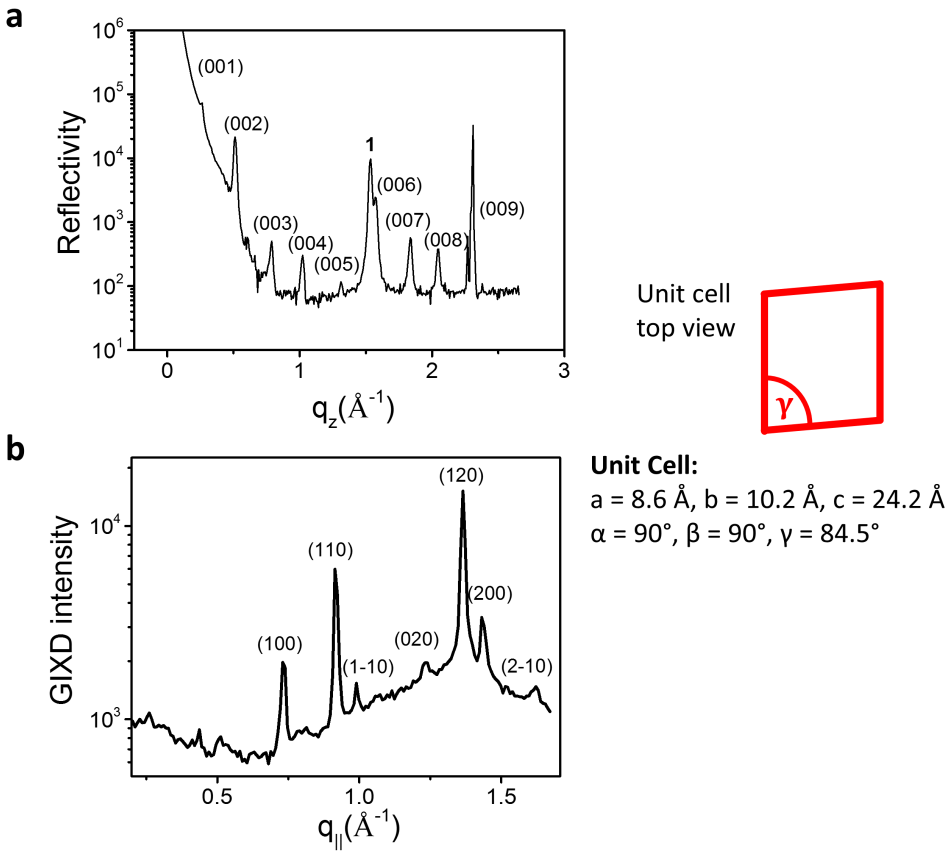

Figure 5.4: Wide-angle XRR (a) and GIXD (b) scans of an azobenzene trimer sample.

ment of a wider q_z region. Several Bragg reflections in the region between 0 and 2.5 Å^{-1} are visible. Most of them are higher order reflections of the (001) out-of-plane Bragg reflection at $q_z = 0.25$ Å^{-1}. The large number of higher order Bragg reflections indicates a very good coherent ordering perpendicular to the substrate surface. The corresponding lattice spacing is 24.3 Å which is significantly smaller than the length of the longitudinal axis of the molecules ($\approx$ 37 Å). One additional Bragg peak at 1.54 Å^{-1}, (denoted with **1** in Figure 5.4a) corresponding to a lattice spacing of 4.08 Å could possibly be attributed to a second crystal phase. The small lattice spacing and the strength of the corresponding Bragg reflection suggest a coexisting structure consisting of many stacked layers of lying-down molecules. The in-plane structure of the molecular crystals has been investigated with GIXD. Figure 5.4b shows a GIXD scan of the same sample. At least seven features have been found. This allows for the determination of an in-plane unit cell. The positions of the Bragg reflections in

Out-of-plane

Reflection	001	002	003	004	005	006	007	008	009
q_z^{exp}	0.263 ± 0.006	0.513 ± 0.015	0.787 ± 0.011	1.021 ± 0.016	1.309 ± 0.013	1.574 ± 0.015	1.837 ± 0.017	2.046 ± 0.014	2.306 ± 0.016
q_z^{calc}	0.258	0.517	0.775	1.034	1.293	1.551	1.810	2.068	2.327

In-plane

Reflection	100	110	1-10	020	120	200	2-10
$q_{||}^{exp}$	0.734 ± 0.010	0.919 ± 0.010	0.991 ± 0.009	1.233 ± 0.014	1.366 ± 0.013	1.437 ± 0.013	1.622 ± 0.013
$q_{||}^{calc}$	0.725	0.911	0.993	1.237	1.378	1.450	1.625

Figure 5.5: Table comparing the measured positions of out-of-plane and in-plane Bragg reflections with calculated positions based on the unit cell as given in the text.

the XRR and GIXD scans are in agreement with the following unit cell parameters: $\mathbf{a} = 8.7$ Å, $\mathbf{b} = 10.2$ Å, $\mathbf{c} = 24.3$ Å, $\alpha = 90°$, $\beta = 90°$, $\gamma = 85°$. The exact values of the unit cell parameters have been determined using a program that calculated the resulting positions of Bragg reflections for a given set of unit cell parameters. Table 5.5 shows the positions of the out-of-plane and in-plane Bragg reflections as measured with XRD and as calculated based on the proposed unit cell. The indexing of the Bragg reflections in Figure 5.4 was performed according to the calculated unit cell. A very high packing density probably involving interdigitating molecular layers is indicated by the volume of the unit cell (≈ 2.1 nm^3) which is only slightly larger than the integrated van-der-Waals volume of a single molecule (≈ 2.0 nm^3). In conclusion, we find that the smaller **T1** azobenzene trimers form molecular crystals with a significantly higher crystalline order as compared with crystals formed by **P1** azobenzene polymers and oligomers which were discussed in chapter 4.

5.2.2 Switching the crystal structure off and on with light

As we already demonstrated in chapter 4, DRS is an excellent method to monitor the switching process of azobenzenes between the E and Z configuration in thin films. Figure 5.6a shows the DRS signal after 5 min of UV-irradiation (≈ 30 mW/cm^2). Upon irradiation with UV-light, the reflectivity increases in the visible region between 2.5 eV and 3.2 eV and it decreases in the UV region between 3.2 eV and 4 eV. At around 3.5 eV there is a small feature that can be attributed to small fluctuations in the output of the UV-LED.

The amplitude of the DRS signal clearly indicates that a significant amount of the

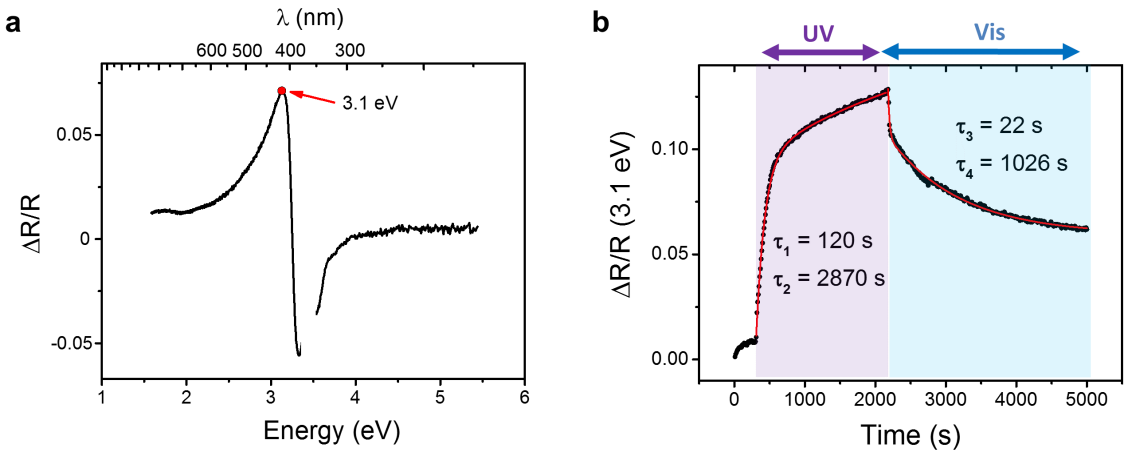

Figure 5.6: Real-time DRS measurements during irradiation with UV-light and visible light. (a) shows the DRS signal vs. the photon energy at a fixed time t and (b) shows the time-resolved DRS signal at fixed photon energy (3.1 eV).

azobenenzene chromophores within the film can be switched. As we already demonstrated in the case of other systems, more can be learned about the isomerization process by studying the ensemble kinetics of the photoisomerization. In Figure 5.6b, the DRS signal at 3.1 eV is plotted against time. After the UV-light is switched on, the DRS signal increases within seconds (see the leftmost red area in Figure 5.6b) to about 1% ($\tau = 4$ s), followed by a much slower increase up to 8% ($\tau = 150$ s). After the UV-light is switched off and the sample is only exposed to the white Xe-light of the measurement lamp, the DRS rapidly decreases by about 2% ($\tau = 3.6$ s) and then decreases in a much slower pace towards a level that appears to be about 2% above the initial level ($\tau = 600$ s). It has been proposed before that in highly ordered environments such as self-assembled monolayers or bulk crystals the photoisomerization can only occur at disordered sites, *e.g.*, close to domain boundaries, defects or at the surface of a bulk crystal. [197, 198]. From DRS measurements alone, it is not possible to understand why there are two extremely different time constants of the photoisomerization kinetics. It is reasonable to assume that the observation of two very different time constants for the photoisomerization process is related to the highly crystalline nature of the sample. Therefore, we performed real-time GIXD to check if the photoisomerization kinetics can be related to structural changes in the film.

Figure 5.7 shows three in-plane Bragg reflections plotted over time as measured at the ID03 surface diffraction beamline at ESRF using a X-ray energy of 9.5 keV. Note that the $q_{||}$ axis is not equidistant because we only monitored the GIXD in-

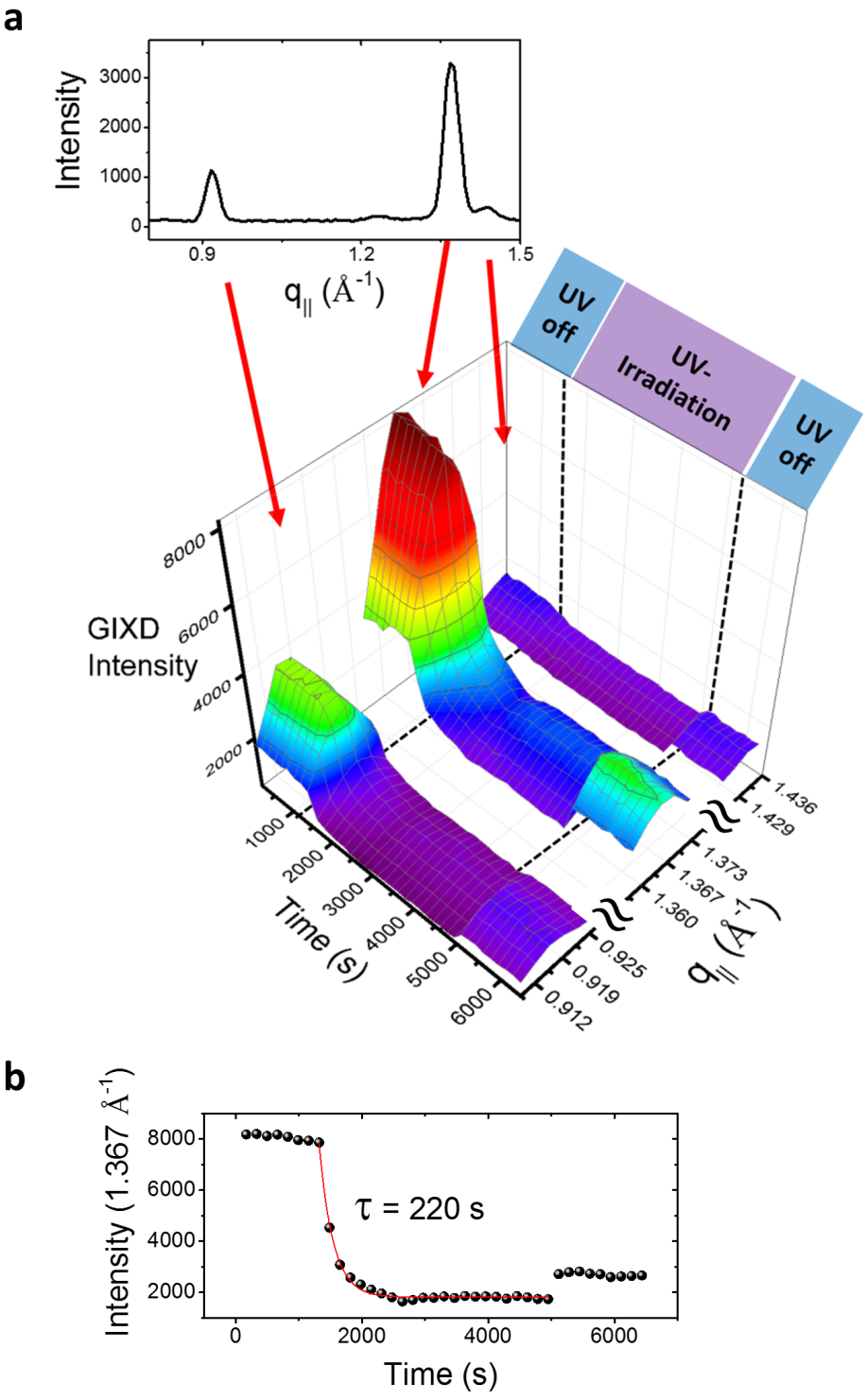

Figure 5.7: Real-time GIXD measurements. Monitored were three in-plane Bragg reflections during irradiation with UV-light. Upon UV-irradiation the intensity of all three Bragg reflections decreases. After the UV-irradiation is switched off, the intensity increases again.

tensity around the Bragg reflections to enhance the temporal resolution. One can clearly see that the GIXD intensity of all three Bragg-reflections decreases upon UV-irradiation ($\approx$ 30 mW/cm^2). The photostationary state is reached with a time constant of τ = 220 s. The Bragg peaks do not completely vanish, indicating that the crystal is not completely destroyed due to the UV-irradiation. After the UV-light is switched off, the GIXD intensity of all three Bragg reflections increases again, indicating a partial recrystallization. We also checked by scanning a wider $q_{||}$-range directly after UV-irradiation of the sample that no new Bragg reflections appear. From this, we conclude that we observe a photoinduced structural phase transition from a crystalline to a disordered phase. Figure 5.7 also shows a cut along the temporal axis. The time constant of the photoinduced phase transition can be derived from the curve. A monoexponential fit gives τ = 220 s. This is in the same order of magnitude as the slower photoisomerization process as measured with DRS (τ = 150 s). This indicates a common origin of the two processes. It is even possible that DRS and GIXD monitor the same photoinduced process. The fact, that the photoinduced process as measured with DRS is about 30% faster than the photoinduced structural transition can be explained by the additional irradiation with white Xe-light in the case of DRS (compare chapter 6). Interestingly, the time constant of the recrystallization is 90 s or less.

5.2.3 Discussion

Figure 5.8 shows a possible scenario that could explain, why the time constant of the photoinduced structural transition (τ=220 s) and the slower time constant of the photoisomerization process (τ=150 s) are relatively similar. Before the first UV-irradiation, nearly all molecules are in a crystalline phase. Only the azobenzenes at the crystal surface have sufficient free volume available for the $E \rightarrow Z$ isomerization. Upon UV-irradiation, they switch with an ensemble time constant of about 4 s. Thereby, the molecules in the region close to the old crystal surface that are now in contact with Z-azobenzenes must rearrange; and this region, which is now the new crystal surface, will become increasingly disordered. In chapter 4, we have already observed that a structural phase transition can be much slower than the photoisomerization process of a molecular ensemble. If the new crystal surface region is sufficiently disordered, the azobenzene chromophores in it will have sufficient free volume available to isomerize. As this process goes on and the crystalline region is continuously shrinking, the real-time DRS signal will look as if there was an additional slower isomerization process of some 'slow' switches. As a consequence of the spreading disorder, the GIXD intensity decreases as observed. In the scenario

that is presented in Figure 5.8, the photoisomerization time constant of every single azobenzene is roughly the same. The slower isomerization time constant as measured with DRS corresponds to the time it takes until the disorder and therefore the free volume will reach the azobenzene chromophores that are deeper in the crystal.

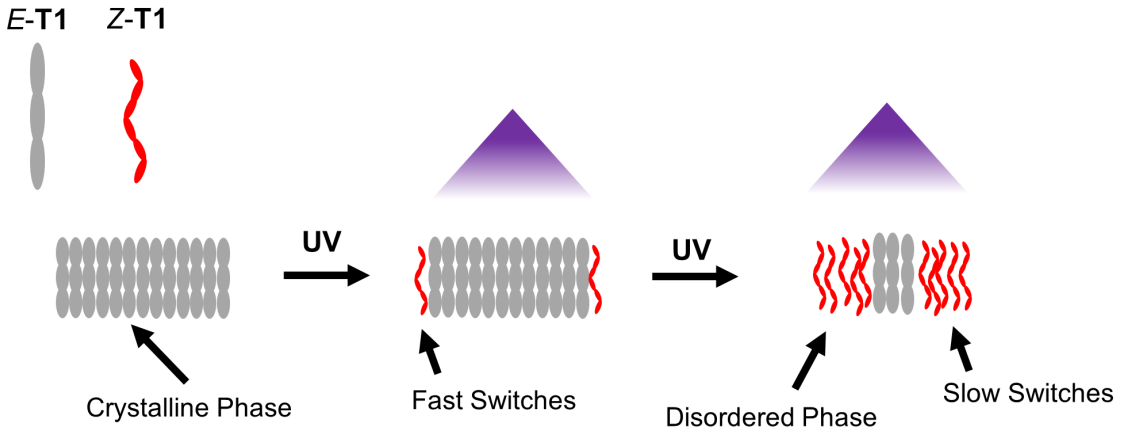

Figure 5.8: Illustration showing how disorder, generated by photoisomerization at the crystal surface might spread through the crystal.

5.3 Conclusion

In this chapter, we studied highly crystalline thin films of azobenzene trimer molecules with dodecyl side chains. We determined the unit cell of the molecular crystal with GIXD and XRR. Using a combination of real-time DRS and real-time GIXD, we monitored the photoresponse of both the azobenzene chromophores and the molecular crystal. Following UV-irradiation of the sample, DRS showed the coexistence of two photoinduced processes with very different time constants. The time constant of the slower process ($\approx$ 150 s) is of the same order as the photoresponse of the molecular crystal that has been measured with real-time GIXD ($\approx$ 220 s). A cascadic scenario could explain all of our findings: The photoisomerization starts at the surface of the molecular crystal, thereby introducing disorder in the adjacent regions deeper in the molecular crystal. The increasing disorder generates additional free volume for the azobenzene chromophores in these regions and enables them to switch from *E* to *Z*. As a consequence, the time constant of the structural phase transition from a crystalline to a disordered phase is of the same order as the slower time constant as measured with optical spectroscopy. This highly cooperative switching behavior might occur in a wide range of crystalline materials incorporating molecular switches. Our main finding, that in crystalline photoresponsive materials

the photoisomerization process of the single molecular switches and the structural photoresponse of the material are interconnected, is thus important for the research field of photoresponsive materials in general. We demonstrated that the photoisomerization of molecular switches that are incorporated in crystalline materials is not always confined to the crystal surface region. This might be a first step towards the developments of novel highly crystalline photoresponsive (nano-)materials in which cooperative effects can be expected to be even more important than in polymeric materials.

6 Cooperative switching in nanofibers of azobenzene oligomers

In chapter 4, we investigated the switching behavior of **P1**-polymers in thin layered films. We found that **P1**-polymers form molecular zippers that can be opened and closed with light. This is a first demonstration that **P1**-type molecular switches could be used as building blocks for supramolecular machines. In this chapter we make the next step towards the development of nanomaterials that demand the integration of multiple molecular switches into larger hierarchical assemblies. We show that azobenzene oligomers of type **P1** self-assemble into well-defined nanofibers and we perform a quantitative analysis of the switching kinetics of these linear, supramolecular assemblies. We find that the photoisomerization of azobenzenes in **P1** nanofibers is significantly slower at higher temperatures, in contrast to isolated azobenzenes where both thermal and optical $Z \rightarrow E$ isomerization are accelerated at higher temperatures. Further, we find that the $Z \rightarrow E$ isomerization is faster when more azobenzenes are in the Z-configuration, demonstrating that interactions between the coupled azobenzenes in **P1** nanofibers lead to cooperative switching.

6.1 Motivation

The development of artificial mechanical machines and molecular motors operating on the nanoscale is one of the most important goals of contemporary nanoscience. [8, 199, 200] Synthetic photoresponsive molecules can be used as building blocks for a large variety of emerging applications ranging from molecular sensors [201], energy [202] and information [4] storage devices to nano-optomechanical devices such as molecular motors [85, 86, 199, 203], artificial muscles [8] and photoactuators [12, 26]. For enabling these applications, it is important to convert molecular nanoscale responses into measurable effects at meso- and macro-scales by integrating molecular switches into well-defined hierarchical assemblies. This can include both

covalent bonding of monomeric switching units to form photoresponsive oligomers or polymers as well as supramolecular assemblies. Examples for such supramolecular systems include linear assemblies as in artificial muscles, 2D arrays for surface functionalization, or 3D crystal lattices for photoactuation. [10,18,19] A high packing density of switching units in these assemblies is crucial in order to maximize, for example, generated forces [18] or energy storage capacity [7]. Within these densely packed supramolecular systems, it is important to control the intra- and intermolecular interaction between switching units, because steric interaction, excitonic and electronic coupling between adjacent molecular switches alters the switching process. Too strong coupling can completely suppress the photoresponse, both via simple steric hindrance or via excitonic coupling leading to delocalization of the excitation before the energy can be transferred to the nuclear coordinates. [24,25] However, coupling within a supramolecular assembly can also lead to positive cooperativity, that is, the chromophores do not switch independently of each other but exhibit emergent behavior, *e.g.*, by supporting switching cascades. [23,27,28]
In synthetic systems, possible applications of positive cooperativity range from sensing devices, where it could be used to amplify detection signals and thus to increase the sensitivity, to artificial muscles, where cooperativity could accelerate the contraction or expansion process. In biological systems, cooperativity is commonly used to accelerate specific processes and to increase or amplify the outcome of reactions. [30] However, there are only very few reports of artificial systems exhibiting cooperative switching, yet. [22,29,31] One problem is to design molecular systems in which the intermolecular coupling is not so strong as to impede reversible switching but strong enough to make the isomerization dependent on neighboring molecules. Azobenzene derivatives in particular are promising building blocks for cooperatively switching multicomponent molecular systems. This is because the isomerization from the stretched out *E*-isomer to the compact *Z*-isomer is accompanied by significant changes of geometry and dipole moment which enables neighboring chromophores to interact during isomerization through sterical or electronical coupling.

6.2 Results

6.2.1 Fibrils of azobenzene oligomers - film morphology

Figure 6.1a shows an AFM image of a sample of **P1** oligomers (see Figure 6.1b) after deposition on native silicon oxide (SiO_2) via spin coating. Thin films of *P1* oligomers were cast from 25 mg/mL solution in toluene. The rotation speed of the

bare substrate was set to 1500 rotations per minute (rpm) before the solution was dispensed. The SiO_2 surface is covered with bundles of fibril structures that each have a typical length of 1-2 µm and a height of about 4 nm. The apparent width of the fibrils ($\approx$ 20 nm) is overestimated due to the finite size of the AFM tip. According to eq. 3.5, the real width of the fibrils is around 4 nm, if the AFM tip has a radius of 10 nm. Many of the fibrils align roughly parallel with respect to each other with a typical spacing of 10 - 30 nm. Also note that only very few of the fibrils on the SiO_2 surface have a loose end, which could indicate the formation of higher aggregates. [204]

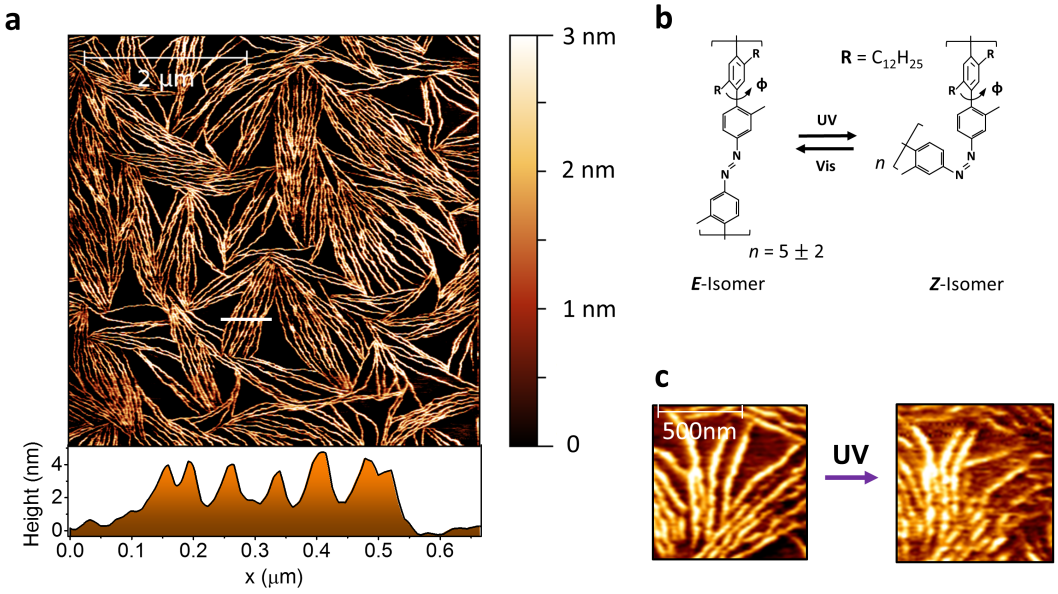

Figure 6.1: (a) AFM image showing a 5 × 5 µm^2 region of a spin coated sample of **P1** oligomers with a height profile. (b) Chemical structure of **P1** and (c) AFM images of the same sample area before (left) and after (right) 5 min of UV-irradiation (30 mW/cm^2).

Since the length of the isolated oligomers in the thermally stable *E*-configuration lies between 3 and 30 nm, the fibrils found with AFM must be supramolecular aggregates consisting of many oligomers. Similar supramolecular aggregates have been found for other poly(*p*-phenylene)s before. [205] The limited width and comparatively homogeneity of the nanofibers suggests the possibility of a stacking motif where the oligomer backbones do not align parallel to the longitudinal fiber axis.

We checked for light-induced structural transitions in the azobenzene oligomer thin films. Figure 6.1c shows AFM images taken in tapping mode before and after 5 min of UV-irradiation (30 mW/cm^2). The overall morphology remains unaffected.

In some areas of the image, small changes, that is, movement or displacement of the fibrils, can be seen. At least one of the straight fibrils in the left image is clearly bent after UV-irradiation. The fibrils persist even after many switching cycles as we checked with AFM. Furthermore, measurements of samples that have been performed almost two years after sample preparation show the same fibril structures. Thus it is safe to say that the fibrils are robust and that the samples can be stored under ambient conditions.

One result of chapter 4 was that in **P1** polymer samples the dodecyl side chains form crystalline nanodomains via interdigitation. To check if the dodecyl side chains also interdigitate in nanofibers of **P1** oligomers we performed GIXD measurements on thin films of **P1** nanofibers. In order to increase the scattering volume, we used samples with a higher nominal thickness for the X-ray measurements, that is, samples containing more oligomers than the samples that were studied with optical spectroscopy. For the preparation of the samples with higher nominal thickness, a

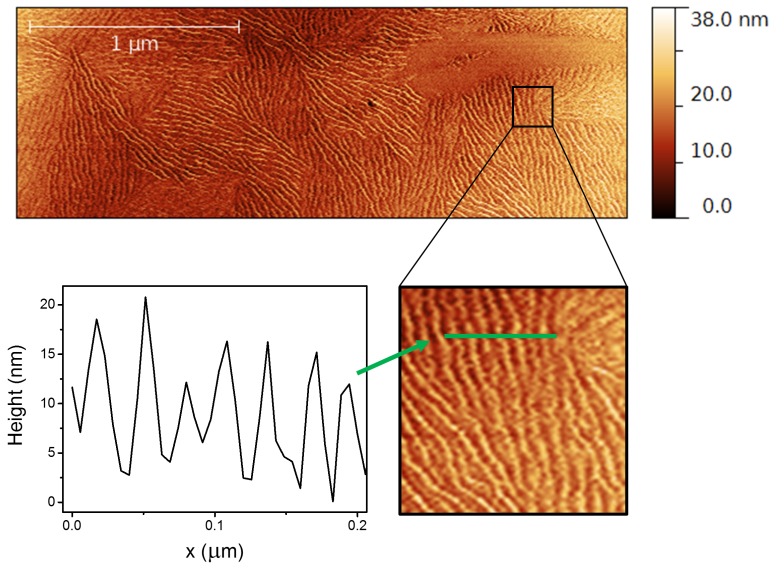

Figure 6.2: AFM image and height profile of a sample with higher nominal thickness.

drop of the 25 mg/mL solution was dispensed onto a resting substrate, that was rotated with 1500 rpm after 5 s waiting time. Figure 6.2 displays an AFM image of a sample with a higher nominal thickness. We find fiber structures with lengths of up to 1 µm, a typical height of 10 nm and an apparent width of about 20 nm, corresponding to a real width of around 4 nm. In comparison with AFM images of samples with lower coverages, such as Figure 6.1a, the nanofibers in Figure 6.2 appear to be packed more densely on the silicon surface.

From the AFM image, we conclude that, indeed, the samples prepared by dispens-

ing the solution onto a resting substrate have a higher nominal thickness (≈ 16 nm instead of ≈ 3 nm) and also consist of nanofibers.
Figure 6.3 shows the scattered X-ray intensity plotted against the in-plane detector angle 2θ. The peak between 21° and 22° can be attributed to the (110) in-plane Bragg reflection of the dodecyl side chains, following the notation of n-alkane crystals. From that, we conclude that the dodecyl side-chains can form crystalline nanodomains in nanofibers of **P1** oligomers, too.

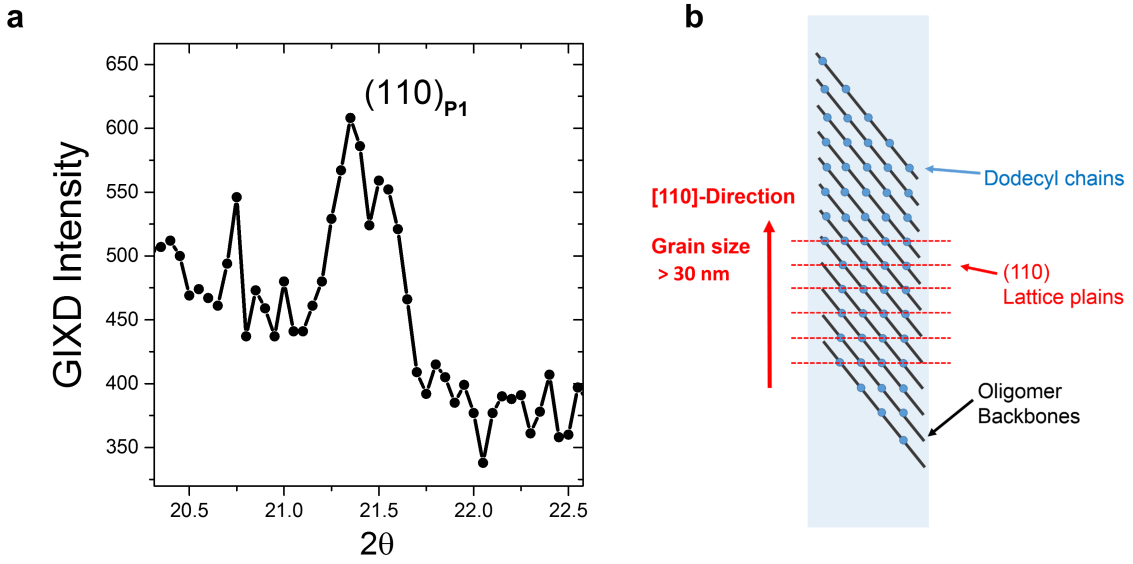

Figure 6.3: (a) GIXD scan of a **P1** oligomer sample. (b) Crystal lattice plains corresponding to the (110) Bragg reflection.

It is possible to calculate a lower bound for the grain size L of a molecular crystal using the Scherrer equation:

$$L = \frac{K\lambda}{\Delta(2\theta)\,\cos\,\theta} \tag{6.1}$$

where K is a dimensionless shape factor close to unity, λ is the wavelength of the X-rays, $\Delta(2\theta)$ is the FWHM of the Bragg reflection in radians after substracting the instrumental broadening and θ is the Bragg angle. The instrumental resolution was 0.22° and the FWHM of the (110) Bragg reflection was 0.45°. Inserting these values into eq. 6.1 gives a lower limit of the grain size in the direction of the (110) planes of 30 nm (± 3 nm). This indicates a stacking motif as illustrated in Figure 6.3b where the oligomer backbones are rotated for about 56° with respect to the longitudinal axis of the nanofibers. The (020) Bragg reflection, corresponding to lattice planes normal to the oligomer backbones has not been found with GIXD, which also points towards a very small grain size along the backbones of the oligomers.

6.2.2 DRS as a tool to measure the isomerization kinetics

Differential reflectance spectroscopy (DRS) provides an easy and efficient way to monitor in real time the conversion of *E*-azobenzene to *Z*-azobenzene in **P1** thin films. DRS measurements demonstrate that the azobenzene chromophores in the thin film can be switched reversibly with UV light and visible light. Figure 6.4a shows a 3D plot of the differential optical reflectance ΔR/R over time for different photon energies. When the UV LED is switched on for the first time at $t = 30$ s, the reflectance is increased in the energy range between 3.2 eV and 4.2 eV, while the reflectance is decreased in the energy range between 2.5 eV and 3.2 eV (see Figure 2b). After the UV LED is switched off at $t = 60$ s, the reflectance returns back to its initial value before the first UV-irradiation. We find an isosbestic point at 3.2 eV, which is characteristic for a transition between only two states.

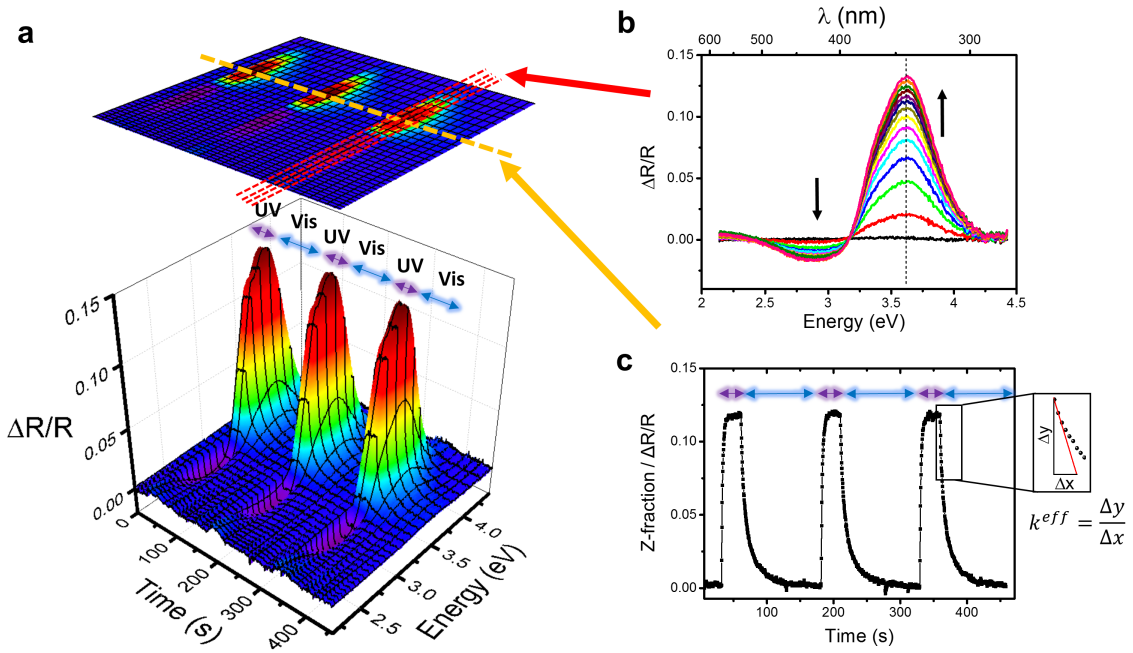

Figure 6.4: (a) Reversible switching of an azobenzene nanofiber sample is apparent from a 3D graph of the optical differential reflectance (DRS) during three switching cycles. Cuts at fixed time as a function of the energy yield DRS spectra (b) and cuts at 3.5 eV as a function of time (c) allow for determination of the effective $Z \rightarrow E$ isomerization rate k^{eff}.

Figure 6.4c shows a cut through Figure 6.4a along the temporal axis at an energy of 3.5 eV. It is possible to extract the photoisomerization kinetics of the azobenzene chromophores from the temporal evolution of the differential reflectance. In a quantitative analysis which we perform later in this chapter, we will find out that the DRS signal can not be fitted with a monoexponential function. In order to

exclude that this unexpected behavior is caused by a nonlinear dependence of the DRS signal on the photoisomerization kinetics, we have to analyse, how the DRS signal and the photoisomerization kinetics are related.

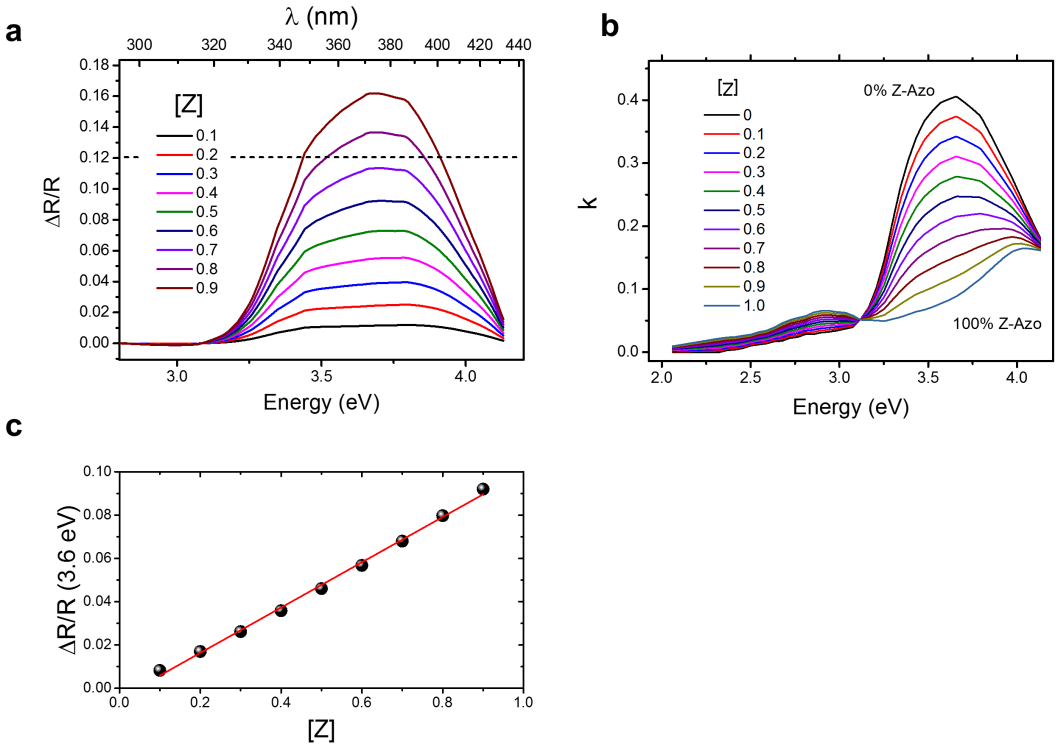

Figure 6.5: (a) Simulated differential reflectance spectra during $E \rightarrow Z$ conversion of **P1** on silicon covered with a thin layer of native silicon oxide. (b) Extinction coefficient k of the azobenzene oligomer film for different fractions of Z-azobenzene in the film. (c) Relation between the DRS signal and the fraction of Z-azobenzene in the film plotted for a photon energy of 3.6 eV.

For thin films on non-transparent substrates such as silicon, the DRS signal ΔR/R does not necessarily have a linear dependence on the fraction of Z-azobenzene in the film. To find the relation between the DRS signal and the photoisomerization kinetics we simulated the DRS signal of a **P1** film on silicon covered with native oxide using the transfer matrix method. [206]

Figure 6.5a shows the simulated DRS spectra. The extinction coefficient k of **P1** both in the E- and in the Z-configuration was determined from absorption spectroscopy measurements in solution. The molar extinction coefficient in solution was converted into the extinction coefficient in the film using the unit cell volume of **P1** polymers in thin films determined in ref. [207]. The anisotropic alignment of the azobenzene chromophores in the fibrils was taken into account. Assuming that E-azobenzene only absorbs light whose polarization vector lies in the plane marked

by the two phenyl rings, one can calculate that for unpolarized light under normal incidence the extinction coefficient of the lying-down azobenzene chromophores in the fibrils is about twice as large as the extinction coefficient of azobenzene chromophores that are isotropically distributed in solution. The spectral shape of the refractive index n of E- and Z-**P1** was calculated from k using the Kramers-Kronig relation. Since the extinction coefficient of **P1** was only known in a finite energy interval between 2 eV and 6 eV, the refractive index n determined by the Kramers-Kronig relation might have a small offset n_∞ due to additional resonances at energies above 6 eV. Also, within an effective medium approximation for the film consisting of a mixture of azobenzene chromophores, alkyl chains and air between the aggregates, we scaled the refractive index using a free parameter within physically reasonable boundaries to reproduce the experimental DRS data. Both the offset n_∞ and the scaling factor of n were considered as free parameters within physically reasonable boundaries and were tuned to reproduce the experimental DRS data. Furthermore, a thin transparent adlayer ($\approx$ 5 nm) modelling the silicon oxide interface was included in the model for a fit of the DRS signal (The introduction or removal of this adlayer had no influence on the linear relation between the DRS signal and the fraction of Z-azobenzene, but improved the fit). The optical properties of mixtures of E- and Z-**P1** were linearly interpolated between the values of pure E-**P1** and pure Z-**P1** (see Figure 6.5b). Figure 6.5c shows that around the $\pi - \pi^*$ absorption band, the DRS signal has a linear dependence on the fraction of Z-azobenzene to a good approximation:

$$\Delta R(\lambda)/R(\lambda) \propto \Delta Z. \tag{6.2}$$

Note that $\Delta Z = Z$, if all azobenzenes are initially in the thermodynamically stable E-configuration. Strictly speaking, eq. (6.2) only holds for the case that the absorption of the two isomers does not shift during the isomerization reaction. In general, this is not true in the solid state. The absorption spectrum of aggregated azobenzene molecules can be strongly shifted with respect to the absorption spectrum of isolated azobenzene due to excitonic coupling between the azobenzene chromophores. [24] Since the aggregation type may change depending on the isomeric state of azobenzenes, one has to consider the effect that the absorbance of the two azobenzene isomers $A_E(\lambda)$ and $A_Z(\lambda)$ may also depend on ΔZ. [119]
However, scaling all the curves in Figure 6.4b to the same amplitude shows that the azobenzene absorption lines do not shift significantly during the isomerization reaction. One possible explanation is, that π-stacking of azobenzene chromophores with azobenzene chromophores of adjacent oligomers may not be possible due to the large dihedral angle between the azobenzene chromophores and the phenyl-rings on

the one hand, and the long alkyl side chains on the other hand. Optical absorption spectroscopy performed on multilayer films of long **P1** polymers showed no significant shift of the absorption line in the solid state with respect to its position in solution. [207] This also suggests, that there is no π-stacking of azobenzene chromophores in thin films of **P1**.

The above given equation 6.2 allows one to fit the real time DRS data analytically using rate equations that describe the fraction of *E*- and *Z*-azobenzene in the film. By comparing the simulated DRS signal with our experimental data, we can also give a rough estimate of how many azobenzene chromophores within the film are switched. According to simulations of the DRS signal using realistic values of the geometry, packing densities and the optical constants of azobenzene in **P1** nanofibers that have been obtained as described earlier, about 70% (+20%/-30%) of the azobenzenes must switch from *E* to *Z* to cause a DRS signal of $\Delta R/R \approx 12\%$. Thus, we can roughly estimate that about 70% of the azobenzene chromophores are switched from *E* to *Z* upon UV-irradiation of the sample with an intensity of 110 mW/cm^2.

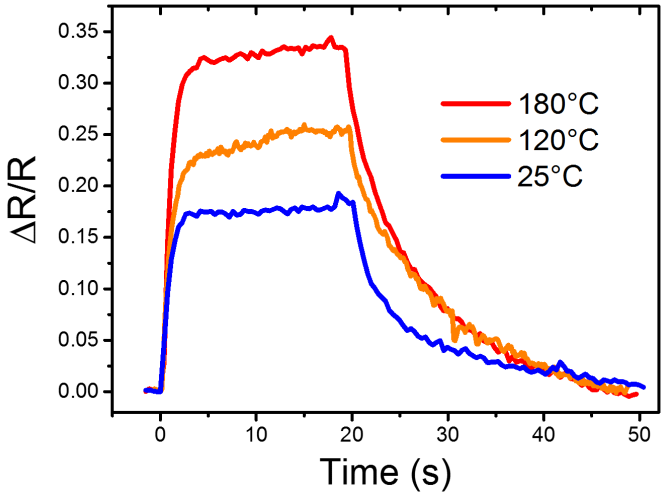

Figure 6.6: Direct comparison of real-time DRS at 25°C, 120°C and 180°C during a single switching cycle.

6.2.3 Cooperative switching

In the following, we discuss the dependence of the effective isomerization rate k^{eff}, that is, the slope of the time-dependent *Z*-azobenzene fraction, on temperature and light-intensity. We performed DRS at three different temperatures to investigate the temperature dependence of the cooperative switching behavior. Figure 6.6 shows

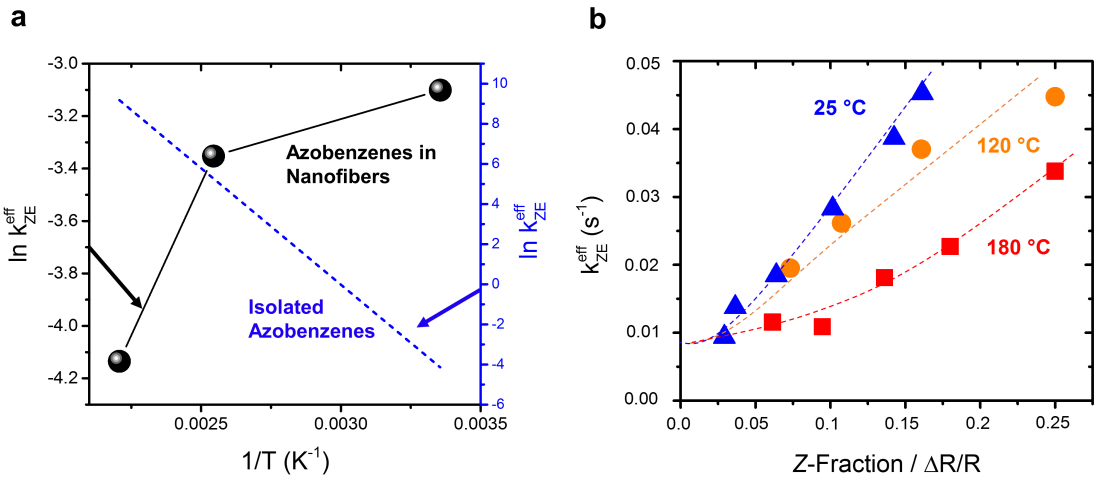

Figure 6.7: (a) Arrhenius plot of the rate of the $Z \rightarrow E$ photoisomerization reaction, measured at three different temperatures, starting from the same level of Z-azobenzene fraction. The thermal behavior we find is in clear contradiction to the behavior of isolated azobenzenes that switch faster at higher temperatures. (b) Dependency of the $Z \rightarrow E$ photoisomerization rate on the fraction of Z-azobenzene in the film, plotted for three different temperatures (dotted lines as guides to the eye), showing that the isomerization rate also depends on the fraction of Z-azobenzene.

measurements of the differential reflectance during one switching cycle, using the same UV LED intensity at 25°C, 120°C and 180°C. All measurements were done for the same **P1** oligomer thin film and performed on the same sample spot. After heating up the sample with a heating stage, we waited for 1 h for the sample to equilibrate its temperature. Note that at higher temperatures more azobenzenes are switched from E to Z under the same irradiation conditions, as indicated by the higher photostationary level. This also shows, that the Arrhenius type behavior of the thermal backswitching is not the dominant thermal effect here. Analyzing the kinetics we find that the azobenzene chromophores in the nanofibers do not switch independently but exhibit cooperativity and non-Arrhenius-type thermal switching behavior. The first indication is shown in Figure 6.7a. Plotted is the measured effective isomerization rate k^{eff} which encompasses contributions from the thermal isomerization rate k_{ZE}^{therm} and the photoisomerization rates k_{EZ}^{light} and k_{ZE}^{light} (see inset in Figure 6.4c). We find that the effective $Z \rightarrow E$ photoisomerization rate starting from the same fraction of Z-azobenzene decreases with increasing temperature. This behavior is diametrically opposed to the behavior of independently switching azobenzenes, for which the thermal back-reaction across an energetic barrier on the order of 1 eV [208] would lead to an increasing k^{eff} with higher temperatures. The

dotted line in Figure 3a shows the typical Arrhenius behavior for this thermal process. Also, the light-induced isomerization rate has been found to be temperature dependent due to free volume effects which would again lead to faster k^{eff} at higher temperatures. [209] In addition to real-time measurements at different temperatures, we also measured the rate of the $Z \rightarrow E$ isomerization as a function of the fraction of Z-azobenzene in the nanofibers. Figure 6.7b shows the effective $Z \rightarrow E$ isomerization rate as a function of the starting level of Z-azobenzene, plotted for three different temperatures. Importantly, the effective $Z \rightarrow E$ photoisomerization rate does not only depend anomalously on temperature but also on the fraction of Z-azobenzene in the nanofibers. This dependency of the kinetics of a single azobenzene unit on the isomeric state of the environment directly shows, that the azobenzenes in the nanofibers do not switch independently but cooperatively.

Simulations of the cooperativity

For a quantitative understanding of the cooperativity, we use a phenomenological model to fit the isomerization kinetics. The real-time kinetics of back-switching from different fractions of Z-azobenzene and the extracted Z-dependent k^{eff} that have been used for the fitting are shown in Figure 6.8a and b, respectively. Plotted in Figure 6.8a is the fraction of Z-azobenzene corresponding to the differential reflectance during several cycles of alternating irradiation with white light (from the Xe-lamp) and white light + UV light of varying intensities. When the dark sample gets exposed to white probe-light of the Xe-lamp, the Z-fraction increases to its photostationary state, and further UV-light from the LED (I = 110, 40, 17, 7 and 1.7 mW/cm^2 in the range 360 - 370 nm) increases the Z-fraction to intensity dependent photostationary levels. After the UV LED is switched off, the Z-fraction returns back to the level corresponding to exclusive irradiation with Xe-light. For independent azobenzene chromophores, the effective rate of the $Z \rightarrow E$ back-isomerization k_{ZE}^{eff} only depends on the spectrum of the Xe-lamp and the temperature and thus would be the same for all switching cycles shown in Figure 6.8a. However, our real-time measurements during several switching cycles with different UV light intensities show that the effective $Z \rightarrow E$ isomerization rate k_{ZE}^{eff}, as measured right after the UV LED is switched off, is faster in those switching cycles where a higher optical output power of the UV LED was used to induce $E \rightarrow Z$ isomerization.

The dependency of the backswitching rate on the Z-fraction cannot be described with the simple rate equation for isolated azobenzene moieties (eq. 6.3), because

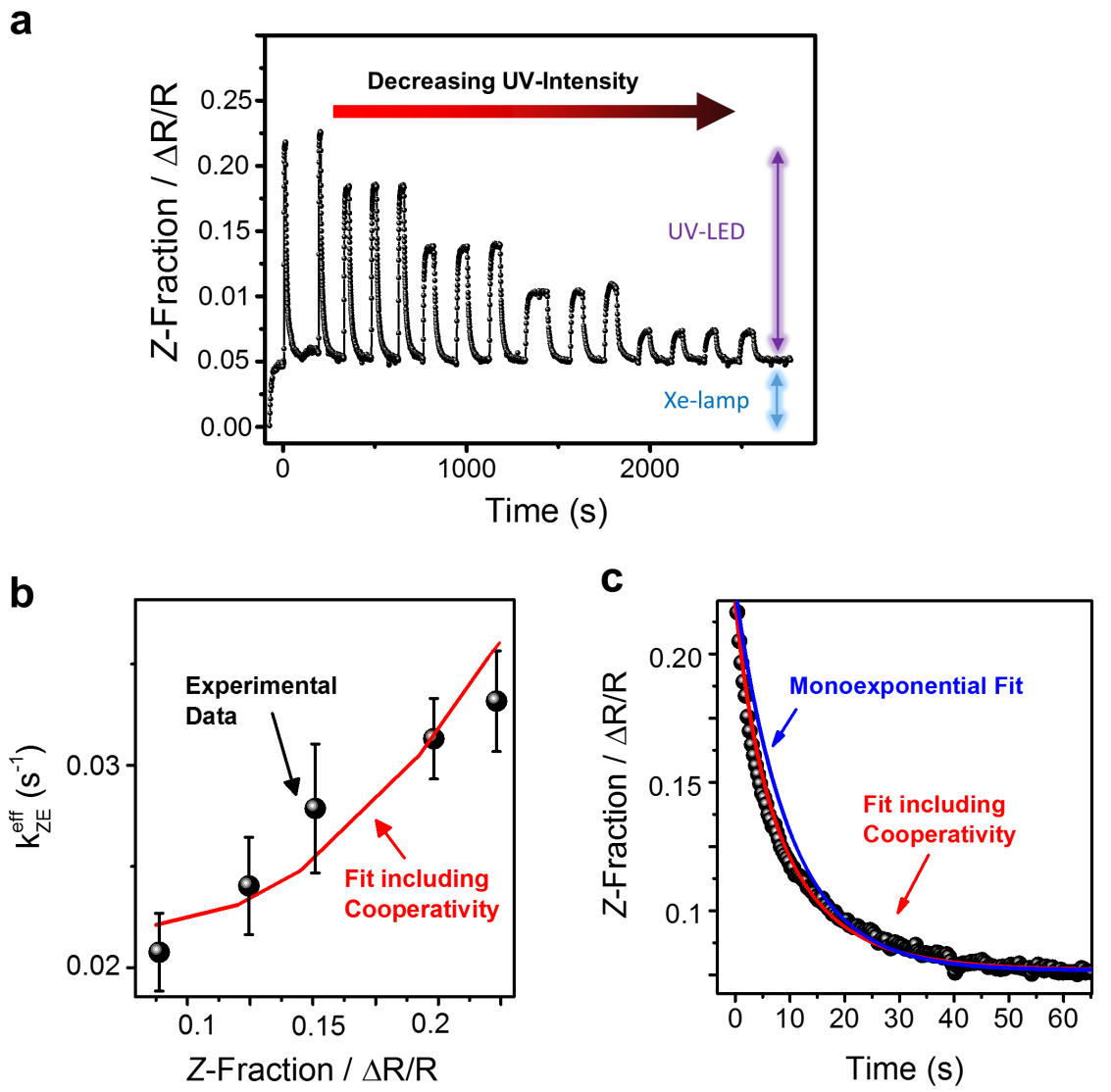

Figure 6.8: (a) Differential reflectance at 3.5 eV during several cycles of alternating irradiation with white light + UV light of varying intensities and white light. (b) Experimentally determined $Z \rightarrow E$ isomerization rates at different photostationary levels together with a simulation including cooperativity (red curve). (c) ΔR/R plotted over time together with fits based on a model without (blue curve) and with cooperativity (red curve).

its solution is a monoexponential function with the Z-independent rate constant $k^{eff} = k_{EZ} + k_{ZE}$.

$$\frac{dZ}{dt} = k_{EZ} \cdot E - k_{ZE} \cdot Z. \tag{6.3}$$

Here, E and Z denote the fraction of E- and Z-azobenzene, k_{EZ} denotes the rates of light-induced $E \rightarrow Z$ isomerization having contributions from both the UV-part of the Xe-lamp spectrum and the UV LED, and k_{ZE} denotes the $Z \rightarrow E$ isomerization rate of azobenzenes having both thermal contributions and contributions from the Xe-lamp. A simple modification to the rate equation (6.3) is to include a linear Z-dependency of the rates. We find, that a modification of the $E \rightarrow Z$ isomerization rate alone cannot explain the observed switching behavior, however, both the kinetics and the photostationary levels of the real-time data can be fitted, when modifying the back-switching rate as follows

$$k_{ZE}(Z) = c \cdot Z. \tag{6.4}$$

Inserting eq. (6.4) into eq. (6.3) introduces cooperative behavior into the rate equation model, that is, the $Z \rightarrow E$ isomerization is faster when there is a higher Z-azobenzene fraction in the film (see Figure 6.8b). Also the shape of the real-time kinetic data is reproduced well in contrast to a monoexponential fit (see Figure 6.8c). Note that we did not introduce additional model parameters, even though a refined model could include, *e.g.*, a further offset parameter to achieve a finite rate at $Z = 0$. In summary, we only need three parameters for the fits to our real-time data: k_{EZ}, c and a scaling parameter that scales Z to the DRS signal (Z / (ΔR/R) $\approx$ 4). The red line in Figure 6.8b results from a fit of the solution of our modified rate equation to the experimental real-time data in $E \rightarrow Z$ switching direction for five different UV-intensities and for five corresponding $Z \rightarrow E$ switching processes. The parameters c and k_{EZ} were fitted, yielding

$$c = 0.105 \text{ s}^{-1} \tag{6.5}$$

and

$$k_{EZ} = 0.0125 \text{ s}^{-1} + 0.0072 \text{ s}^{-1} \cdot \frac{I_{UV-LED}}{\text{mW cm}^2}, \tag{6.6}$$

where I_{UV-LED} denotes the intensity of the UV-LED in mW/cm^2.
For $I_{UV-LED} = 0$, the remaining $E \rightarrow Z$ photoisomerization rate $k_{EZ} = 0.0125$ has purely contributions from the probe light of the Xe-lamp. The good agreement of our simulation model with the measured cooperative kinetics indicates, that the linear Z-dependence of the $Z \rightarrow E$ isomerization rate, indeed, is a good approximation.

Figure 6.9 shows fits to the DRS data based on the modified rate equation.

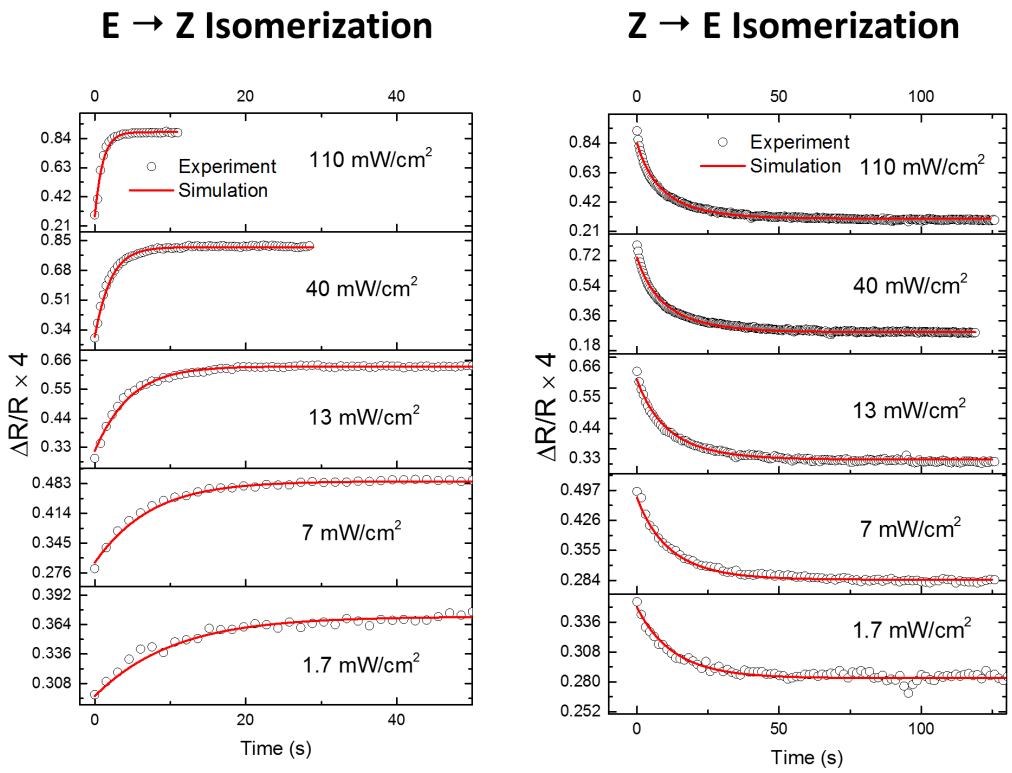

Figure 6.9: Real-time DRS data during irradiation with UV-light (left) and visible light (right). Shown are five cycles of alternating irradiation with UV-light and visible light corresponding to five different intensities of the UV-LED. The red lines are analytical fits based on our modified rate equation model.

6.2.4 Discussion

Based on the findings of a Z-dependent $Z \rightarrow E$ isomerization rate in nanofibers, we now discuss the origin of cooperativity, in particular, inter- and intramolecular interactions of the azobenzene chromophores. Theoretically, electrostatic interactions of the oligomers with the SiO_2 surface might also play a role. However, it is reasonable to assume that the interaction between the long nonpolar alkyl sidechains and the SiO_2 surface is not the dominant effect, here. Isolated azobenzene derivatives have been shown to exhibit cooperative switching behavior in solution due to π-π-stacking or electronic coupling between azobenzene moieties. [31,122] However, in the case of the rigid rod polymer **P1**, the azobenzene chromophores are electronically decoupled.

In an earlier study by Bléger et al., no signs of cooperative switching have been found for isolated **P1**-type molecules. [126] They studied the switching kinetics of

P1-type molecules dissolved in cyclohexane ($\approx 10^{-5}$ mol/L). In such an extremely diluted solution, no supramolecular aggregates are formed. For comparison, our nanofiber samples were prepared from a solution with a much higher concentration of about $5{\cdot}10^{-2}$ mol/L, whose high absorbance made spectroscopic measurements in solution difficult. In this earlier study, the isolated **P1**-type molecules exhibited Arrhenius-typical thermal behavior and their switching kinetics followed a mono-exponential function and thus did not depend on the fraction of *Z*-azobenzene. In

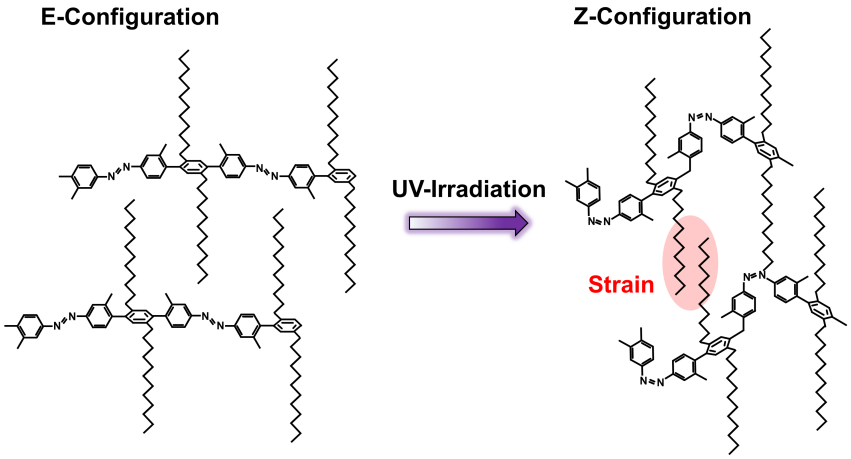

Figure 6.10: Illustration how $E \rightarrow Z$ isomerization of azobenzene might lead to strained alkyl side-chains.

contrast, intermolecular coupling as well as intramolecular coupling of **P1** azobenzenes in nanofibers is possible, either via dipole-dipole interactions or via strain. In the *Z*-configuration, azobenzene has a static dipole moment of about 3 Debye while azobenzene in the *E*-configuration has a dipole moment near zero. [40] Strong static dipole moments due to a large fraction of *Z*-azobenzene in the nanofibers could influence the back-switching kinetics of *Z*-azobenzene. Also, a larger fraction of *Z*-azobenzene within the sample corresponding to more twisted oligomers may cause strain in the environment due to the altered alkyl chain spacing along the polymeric chain (see Figure 6.10). It is well known that mechanical strain can influence the isomerization kinetics of azobenzene. [210] Tamaoki et al. demonstrated that for bridged bis-azobenzenes, the $Z \rightarrow E$ isomerization is accelerated by orders of magnitude if the *Z*-isomer is strained. [211] Turansky et al. performed simulations of the photoinduced $Z \rightarrow E$ isomerization of stretched azobenzene and found, that mechanical stretching favors the photoinduced $Z \rightarrow E$ isomerization. [212, 213] At temperatures above 120-150°C, roughly corresponding to the melting temperature of polyethylene, the ordered alkyl side-chain domains involve

more gauche-defects [214], thereby decreasing the intermolecular interaction strength of azobenzene chromophores of different oligomers. This could weaken the coupling via side-chain mediated strain and thereby suppress the positive cooperativity.

6.3 Conclusion

In this work, we showed that azobenzene oligomers form nanofibers with well-defined dimensions and shapes, having lengths of 1-2 µm, a typical width of around 4 nm and a height of about 4 nm. Whereas the azobenzene units in isolated molecules switch independently [126, 128], the azobenzene units in the nanofibers are coupled via intermolecular interactions and switch cooperatively as evidenced by unusual thermal and kinetic behavior: first, in contrast to the common Arrhenius-type behavior of isolated molecular switches, the isomerization rate of azobenzenes in the nanofibers is faster at lower temperatures. We attribute this to the temperature dependency of the intermolecular coupling strength of the azobenzene chromophores via side-chain mediated strain. Second, the $Z \rightarrow E$ isomerization rate depends approximately linearly on the fraction of Z-azobenzene within the film. To our knowledge, this is the first demonstration that multi-azobenzene compounds can self-assemble into photoresponsive nanofibers that are stable on surfaces. Our findings are important for next-generation optomechanics and sensing devices based on arrays of molecular switches, as they show that it is possible to significantly accelerate the photoisomerization reaction of azobenzene by leveraging cooperativity of mechanically interlocked molecular switches. In future studies, coupled azobenzene polymers of type **P1** could be integrated into multicomponent molecular systems that utilize cooperativity to fulfil useful tasks above the molecular scale, *e.g.*, nanofibers that can be reversibly contracted and expanded with light, or nano-robotic arms that bend upon UV-irradiation.

7 Summary: From functional molecules to functional materials - translating molecular processes into the macroscopic world

This chapter gives a summary of the experiments presented in this thesis as well as their main results. In this thesis, a combination of structural (XRD and AFM) and spectroscopic (DRS) real-time techniques has been used to study physical processes at the molecular scale in photoresponsive materials to find out how the (supra-)-molecular structure and the photoresponse of the materials are related.

7.1 Light-controlled molecular zippers based on azobenzene main-chain polymers

The development of artificial mechanical machines and molecular motors operating at the nanoscale is one of the most important goals of contemporary nanoscience. The integration of photochromic molecular switches into hierarchical assemblies, *e.g.*, into layered thin films or 3D nanostructures, will make it possible to construct smart and dynamic materials, that is, materials with switchable properties. Azobenzene, probably the most extensively studied molecular switch, can be switched from the thermally stable planar *E*-isomer (*E*) to the metastable 3D *Z*-isomer (*Z*) via irradiation with UV-light. The back-reaction from *Z* to *E* proceeds via thermal relaxation or can be induced by irradiation with blue light. A large variety of photomechanical responses has been found for polymers with azobenzene chromophores in the side chains. Many application ideas demand that light-induced collective or cooperative motions of azobenzenes at a molecular level can be amplified to macroscopic scales, often via a photoinduced phase transition within the polymer film. Many of the photoresponsive systems that have been investigated during the last decades incorporated azobenzene polymers with azobenzenes in the side chains. The

molecular structure of these liquid crystalline materials can be switched by a light-induced modification of the intermolecular interaction. More recently, a number of azobenzene polymers with azobenzene units incorporated in the polymeric backbone have been developed. They have the potential to give a more direct optical control over the molecular structure. Recently, Bléger *et al.* designed rigid rod polymers with electronically decoupled azobenzenes in the main chain and dodecyl side chains. It has already been shown that this molecular design enables a maximized photodeformation in solution and for crawling motion on surfaces. The rigid-rod polymer **P1** incorporates azobenzene chromophores in a poly(para-phenylene) backbone with two dodecyl side chains per repeat unit (see Figure 7.1). The azobenzene polymers

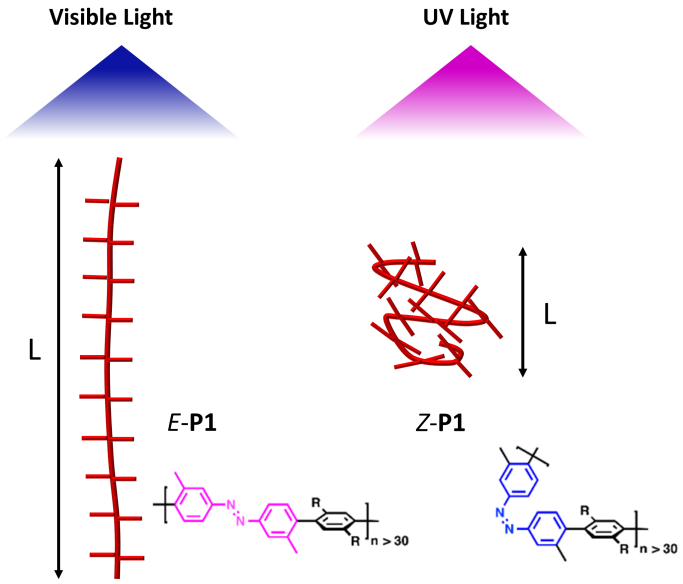

Figure 7.1: The multi-azobenzene compound **P1** converts light into mechanical work.

can be switched from a thermodynamically stable linear and elongated conformation, where the azobenzenes are in the *E*-configuration to a compact and kinked conformation with azobenzenes in the *Z*-configuration.

- *First result: Molecular zippers formed by azobenzene-main chain polymers with alkyl side chains (**P1**) can be opened and closed with light.*

In this thesis, a detailed study of the switching mechanism of **P1**-polymer thin films has been performed.
AFM images of the main chain azobenzene polymer films show a homogeneous sample morphology, characterized by large islands with diameters > 1 µm and several clearly distinguishable layers. The molecular structure of the film has been investigated with grazing incidence X-ray diffraction (GIXD). We find that the alkyl side

chains of the azobenzene polymers adopt the thin film crystal structure of n-alkanes. This crystal structure involves interdigitation of the alkyl side chains, thereby leading to a 'molecular zipper' structure.

- *Second result: Photoisomerization of a small fraction of azobenzene chromophores occuring within seconds triggers a complete amorphization of the layered thin film that occurs on the timescale of several minutes.*

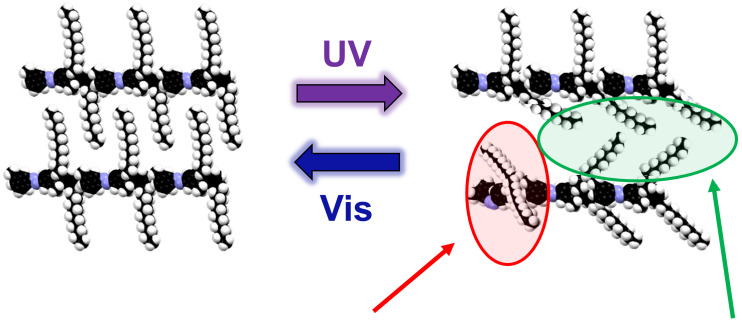

Figure 7.2: Light-induced $E \rightarrow Z$ isomerization of azobenzene chromophores in the polymer main chain disrupts the coherent ordering of dodecyl side chains.

Using real-time GIXD during irradiation with visible and UV light, we show that it is possible to switch the **P1** thin films reversibly between a highly ordered state involving interdigitating dodecyl side chains (closed zippers) and a significantly less ordered state with disordered side chains (open zippers). This is the first demonstration of a rigid main chain polymer-based molecular zipper undergoing reversible light-controlled opening and closing. Based on optical spectroscopy data, we estimate that about 20 % of the azobenzenes in the thin film can be switched. We conclude that the photoinduced structural transition is indeed triggered by the photoisomerization of azobenzene chromophores (see Figure 7.2). A comparison of the switching kinetics as monitored with GIXD and DRS yielded that the structural transition is about 12 times slower than the ensemble isomerization kinetics of the azobenzene chromophores. Thus, the amorphization occurs on a much larger timescale (τ = 90 s), determined by structural and topological constraints. It is a remarkable result that fast $E \rightarrow Z$ isomerization (τ = 5 s) of a small fraction ($\approx$ 20 %) of all azobenzene chromophores within the polymer film is sufficient to disrupt the long range ordering of the protruding dodecyl side chains and to induce amorphization of the film. Our findings of a delay between azobenzene switching and the structural effects are important for optomechanically active or self-healing

materials that make use of a reversible light-controlled phase transition. Our results have been published in 2015 in ***Macromolecules***. [207]

7.2 Switching in molecular crystals

In chapter 5, we studied the photoisomerization of azobenzene trimers in highly crystalline environments. Short azobenzene trimers with alkyl side chains (**T1**) form crystalline thin films exhibiting long-range coherent order as found with XRR and GIXD. We determined the unit cell of the molecular crystal with GIXD and XRR.

- *Third result: In highly crystalline thin films, cooperative switching behavior can trigger a cascadic structural phase transitions.*

Using a combination of real-time DRS and real-time GIXD, we monitored the photoresponse both of the azobenzene chromophores and of the molecular crystal. Following UV-irradiation of the sample, DRS shows the coexistence of two photoinduced processes with very different time constants (τ_1=4 s and τ_2= 150 s). The time constant of the slower process ($\approx$ 150 s) is of the same order as the photoresponse of the molecular crystal as measured with real-time GIXD ($\approx$ 220 s). A cascadic scenario could explain all of our findings (see 7.3): The photoisomerization starts at the surface of the molecular crystal, thereby introducing disorder in the adjacent regions deeper in the molecular crystal. The increasing disorder generates additional free volume for the azobenzene chromophores in these regions and enables them to switch from E to Z. In this way, the time constant of the structural phase transition from a crystalline to a disordered phase is of the same order as the slower time constant as measured with optical spectroscopy.

This highly cooperative, cascadic behavior is an important aspect of a wide range of crystalline materials incorporating molecular switches and azobenzene in particular. The azobenzene $E \rightarrow Z$ isomerization requires a critical free volume to occur. The reaction from the elongated E-isomer to the more compact Z-isomer creates additional free volume in certain parts of the environment, enabling more E-azobenzenes to isomerize. Our main finding, that in crystalline photoresponsive materials the photoisomerization process of the single molecular switches and the structural photoresponse of the material can be interdependent, is therefore important for many future supramolecular devices and machines that use azobenzene derivatives in crystalline environments.

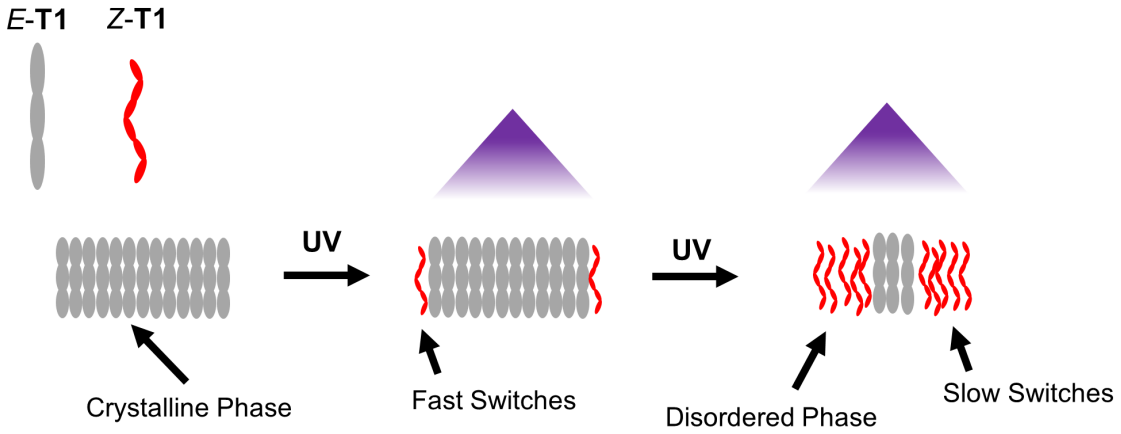

Figure 7.3: Disorder, generated by photoisomerization at the crystal surface, spreads through an azobenzene trimer crystal and enables more azobenzenes to switch.

7.3 Cooperative switching in nanofibers of azobenzene oligomers

In the following chapter 6, we moved from 2D thin film structures on to linear supramolecular aggregates and looked into the switching process of multiazobenzene compounds integrated into nanofibers. The arrangement of photoresponsive molecules to larger supramolecular aggregates that convert the randomly oriented photoresponse of single molecules into a directed photoresponse at the meso- or macroscale is a crucial step towards the development of future artificial muscles based on multi-azobenzene compounds.

- *4^{th} result: Shorter **P1** oligomers form robust nanofibers in solution. After deposition onto surfaces, the azobenzenes in the nanofibers can still be switched reversibly with high efficiency and reproducibility.*

Moreover, the interaction between mechanically interlocked molecular switches in supramolecular aggregates can lead to emergent behavior, *e.g.*, cooperative switching. Whereas cooperativity can suppress the photoresponse in some cases, cooperativity could ideally also be used to couple the switching process of single molecular switches and to amplify the response of (supra-)molecular devices and machines. In this thesis, we performed a quantitative analysis of the cooperative switching behavior on the example of fibrils of shorter **P1** oligomers on SiO_2.

- *5^{th} result: In nanofibers, azobenzene chromophores switch cooperatively as indicated by the fact that the $Z \rightarrow E$ isomerization rate depends on the fraction of Z-azobenzene in the microenvironment.*

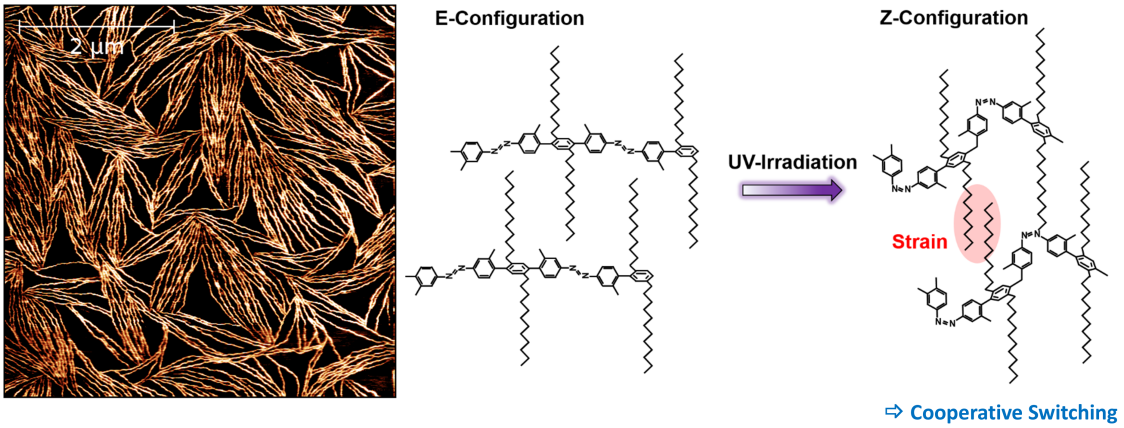

Figure 7.4: AFM image showing nanofibers consisting of **P1** oligomers (left) and a sketch showing how side-chain mediated strain can lead to cooperative switching (right).

With AFM, we observed that azobenzene oligomers form well defined nanofibers in solution, with lengths of 1-2 µm, a typical width of 30 nm and a height of about 4 nm. Deposited on SiO_2 substrates via spin-coating the nanofibers tend to align parallel with respect to each other. Upon irradiation with UV or visible light, the azobenzene chromophores within the nanofibers can be switched reversibly and the nanofibers may move or bend as observed with AFM performed before and after switching. This is the first demonstration that photoresponsive nanofibers consisting of multi-azobenzene compounds can be used for the efficient conversion of light into mechanical work, *e.g.*, in artificial muscle strands. By monitoring the ensemble kinetics of the $Z \rightarrow E$ isomerization with real-time DRS, we find that the isomerization of the azobenzene chromophores is cooperative since the $Z \rightarrow E$ isomerization rate depends on the fraction of Z-azobenzene within the film. As a result, the light-driven isomerization from the compact Z-isomer to the stretched E-isomer is significantly accelerated in comparison with isolated azobenzenes (up to a factor of 4). We also find that the cooperativity decreases at temperatures above the melting temperature of the alkyl side-chains. Thus, we attribute the emergent cooperative behavior to side-chain mediated strain generated by the isomerization of adjacent azobenzene chromophores. This result is important for applications in optomechanics, *e.g.*, for artificial muscles, as it shows that by utilizing cooperativity it is possible to significantly increase the mechanical power that can be generated by light within a certain timeframe in arrays of molecular switches. An article with our findings has been submitted recently.

8 Appendix

8.1 Self-assembled monolayers (SAMs) on Si(111)

In addition to our studies of molecular switches in thin films and nanostructures, we also performed some X-ray scattering on self-assembled monolayers (SAMs) on Si(111) surfaces. The SAMs we studied are used to attach molecular switches via click-chemistry to silicon surfaces. The structure and, in particular, the packing density of the underlying linker SAM is crucial for the functionality of the photoresponsive system. In detail, we compared three different samples. In the first sample, the Si(111) surface is passivated with a layer of hydrogen. In the second sample, an Alkin-SAM is attached to the Si(111) surface. And in the third sample, molecular switches (fulgimides) are attached to the Si(111) surface via the Alkin-SAM.

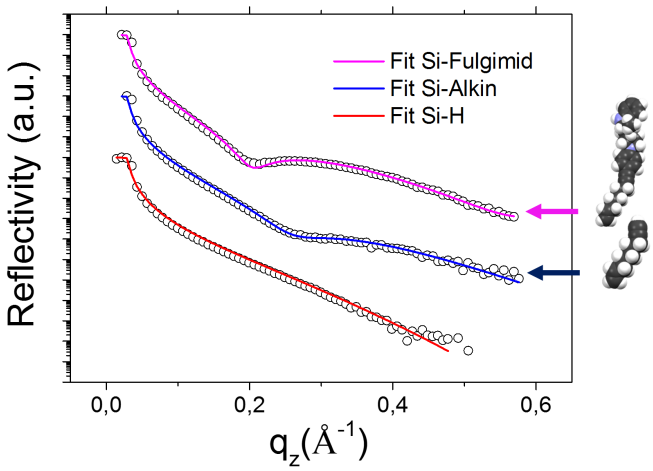

Figure 8.1: X-ray reflectivity of three different Si(111) samples. One is passivated with hydrogen (Si-H), one is covered with an Alkin-SAM and one is functionalized with molecular switches (Si-Fulgimid)

Figure 8.1 displays the X-ray reflectivity of all three samples (y-axis shifted for clarity). The XRR curve of the hydrogenated surface shows no significant features beyond the total reflection edge. The reflectivity of the alkin-sample, however, exhibits a local minimum at about $q_z = 0.25$ Å^{-1}, indicating a thin layer on top of the Si(111) substrate. The thickness of the adlayer d can be estimated via the formula

$d = \frac{\pi}{q_z^{min}}$, where q_z^{min} denotes the position (in Å^{-1}) of the first local minimum in the XRR scan. The exact thickness of the adlayer can be determined via a fit using Parratt's formalism (the continuous lines in Figure 8.1). This fit gives a thickness of 11.5 Å± 1 Å, a roughness of 4 Å and an electron density of 0.32 e$^-$/Å^3. We also know that a single alkin molecule has 69 electrons. From this, we can calculate the area per alkin-molecule to be about 19 Å^2, which corresponds to about $5.3 \cdot 10^{14}$ molecules/cm^2 or a Si-bond coverage of 68 ± 5 %, respectively. A Si-bond coverage above 50 % can be considered very high. A coverage of 68 % is close to the maximal theoretically possible coverage. One explanation for the extremely dense packing of the alkin molecules is that the anchor group of an alkin is significantly smaller than the anchor group of an alkyl-chain due to the carbon double bond. This allows alkin molecules to attach more molecules per cm^2 to the Si(111) surface.
The upmost curve in Figure 8.1 displays the XRR of an alkin SAM that is functionalized with molecular switches (fulgimides). The first local minimum is shifted to smaller values of q_z, indicating a higher thickness of the adlayer. A Parratt fit gives a total thickness of 17.2 ± 2 Å, a roughness of 3.2 Å, and an electron density for the additional fulgimide layer of 0.22 e$^-$/Å^3. From this, we can calculate that, in average, the coverage of fulgimides on top of the alkin layer is about 14 %, that is, a switch is attached to every 7'th alkin molecule.

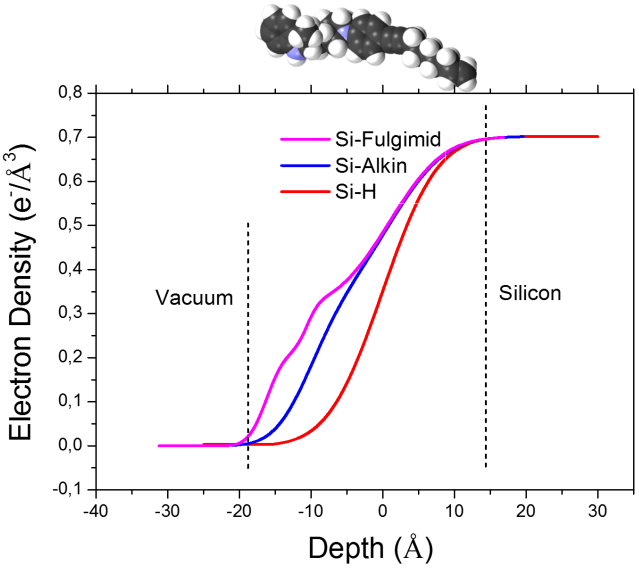

Figure 8.2: Electron density distribution of the three different samples, as obtained from Parratt fits to the XRR.

Figure 8.2 shows the electron density distributions of the three Si(111) samples, as determined from Parratt fits to the XRR curves. Whereas the alkin layer on the Si(111) substrate was fitted using a two box model, the fulgimide-functionalized

SAM is fitted using a three box model in which the values of the pure alkin layer have been re-used.

8.2 Switching SAMs on Si(111)

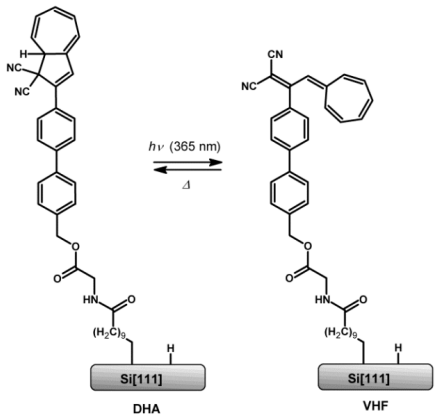

Figure 8.3: The molecular switch Dihydrazulene (DHA) can be attached to Si(111) surfaces via an acid-terminated linker SAM. Upon UV-irradiation, DHA can be switched to Vinylheptafulvene (VHF).

In addition to investigations of the SAM structure, we also performed *in situ* XRD on SAMs functionalized with molecular switches during switching. Here, we present a study of a Dihydrazulene (DHA) SAM on Si(111). The molecular switch Dihydroazulene/Vinylheptafulvene can be switched reversible via a ring opening/closing reaction between two stable isomers. Upon UV-irradiation, the stretched out DHA can be switched to the tilted Vinylheptafulvene (VHF) as shown in Figure 8.3. The backreaction can only be induced thermally. The molecular switches have been attached to the Si(111) surface via an acid-terminated alkyl linker SAM.

The thickness, electron density and surface coverage of DHA SAMs on Si(111) were determined with XRR. Figure 8.4 shows the true specular XRR curve of a freshly prepared DHA SAM on Si(111) as a function of momentum transfer $q_z = 4\pi/\lambda \sin\theta$, with θ being the angle of incidence. The occurrence of a local minimum at $q_z = 0.12$ Å^{-1} indicates a 2 - 3 nm thick adsorbed layer on top of the Si(111) surface. A Parratt fit using a stratified homogeneous media approach gives a film thickness of 25 ± 1 Å, a mean-square roughness of 5.7 ± 0.5 Å and an electron density of 0.41 ± 0.03 e$^-$/Å^3. The electron density distribution, obtained from the fit, is plotted in the inset of Figure 8.4. Our XRR-measurements of the bare linker-SAM without DHA attached gave an electron density of about 0.30 e$^-$/ Å^3 and a thickness of 14 ± 1 Åfor the linker-SAM, corresponding to an area of 24 ± 2 Å^2

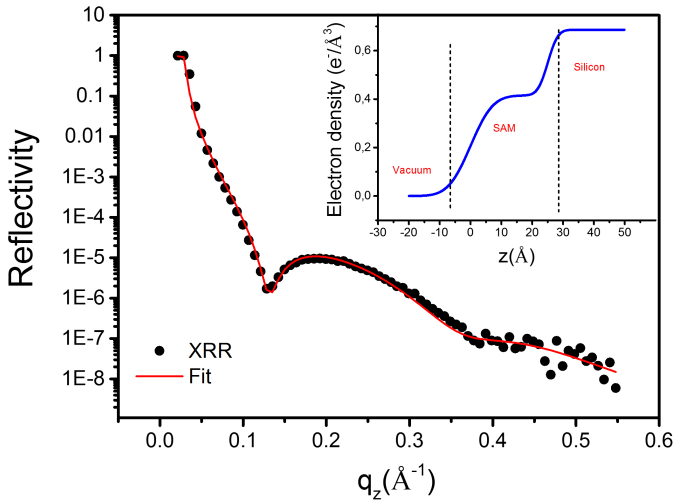

Figure 8.4: X-ray reflectivity of a DHA-SAM on Si(111). The inset shows the electron density profile as given by the Parratt fit. The measurement was performed at 70°C to exclude nano-scale water adsorbation. The fit parameters suggest that DHA is attached to 51 (± 5)% of all alkyl-chains.

per linker-molecule. [215] Thus, the attachment of DHA leads to a higher electron density and a larger film thickness. It is possible to calculate the area per DHA molecule A^{DHA} using the formula

$$A^{DHA} = \frac{n_e^{DHA}}{d^{DHA} \cdot \rho_e^{DHA}}. \tag{8.1}$$

Here, n_e^{DHA} denotes the number of electrons per DHA molecule, d^{DHA} is the additional thickness contribution and ρ_e^{DHA} is the additional electron density contribution caused by the attachment of DHA on top of the linker-SAM. This gives an area of 12 ± 1 Å^2 per DHA molecule, meaning that a DHA molecule is attached to every other alkyl-chain.

In addition to structural investigations, we managed to detect reversible, light-induced switching of DHA-SAMs with XRR. Figure 8.5 shows the XRR, plotted for alternating irradiation with UV-light and visible light, close to the local minimum at $q_z = 0.12$ Å^{-1}, where the XRR signal is very sensitive to small changes in the film thickness, since the film thickness is directly connected to the position of the minimum. While 60 min of irradiation with UV-light leads to an increase of the XRR signal at $q_z = 0.12$ Å^{-1}, irradiation with visible light brings back the initial XRR intensity. Both irradiation with UV-light and with visible light lead only to

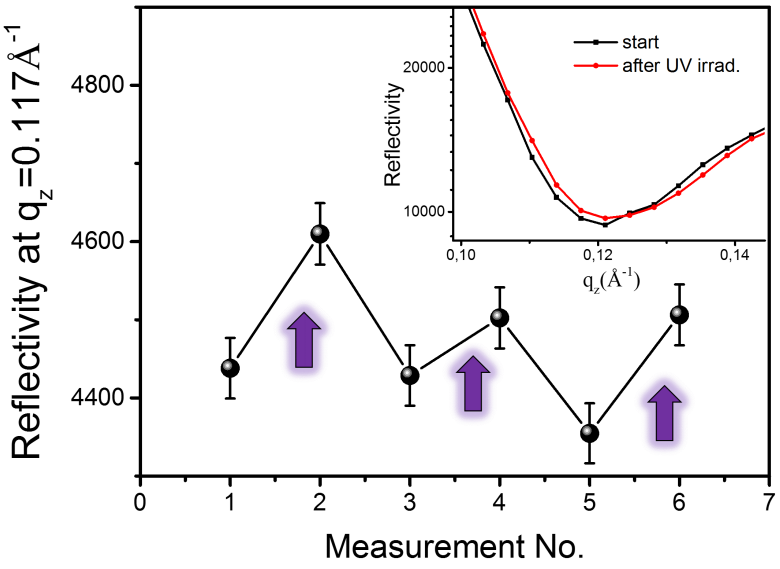

Figure 8.5: Optically induced switching monitored with X-ray reflectivity. Plotted is the reflectivity in the region close to the first minimum (average over three adjoining points to improve statistics), where the sensitivity for the switching process is best (see inset in the upper right). Arrows indicate illumination with UV-light (365 nm, 80 mW/cm^2). Measurements number 2, 4 and 6 were taken after 4 h illumination with UV-light, while measurements 1, 3 and 5 were performed after leaving the sample for about 20 h each time in the dark. All measurements were performed at 110°C to exclude water-related effects.

a negligible change of sample temperature (< 2°C). We performed three switching cycles to check if the light-induced changes were reversible and reproducible. The inset in Figure 8.5 shows the section of the XRR around the first minimum before and after irradiation with UV-light. One can clearly see that UV-irradiation causes a shift of the minimum to higher q_z values, corresponding to a decrease in film thickness.

To estimate the absolute change in film thickness and interface roughness, we plotted the relative difference of XRR before and after irradiation with UV-light

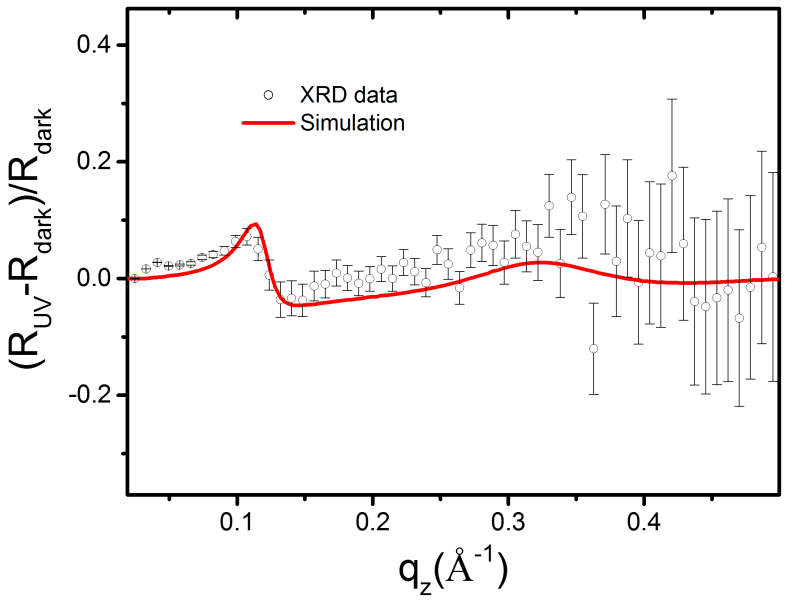

Figure 8.6: Experimental data and simulation of the normed difference between the XRR before and after illumination with UV light. The best fit suggests that the average SAM thickness is decreased for about 0.2 Å upon UV-irradiation while the mean-square roughness of the SAM-air interface increases for about 0.1 Å.

(Figure 8.6). Here, one can see that the biggest deviation indeed occurs around the first minimum at $q_z = 0.12$ Å^{-1}. Starting from the Parratt Fit parameters of the XRR from the not-irradiated sample, we were able to get a reasonable fit to the data. The best fit suggests a UV-light induced decrease of the film thickness of about 0.2 Å and an increase of the interface roughness on top of the SAM of about 0.1 Å. These rather small geometrical change of the SAM, compared with the expected conformational change of a single DHA molecule upon isomerization, indicates that, at a sample temperature of 110°C, only a fraction of the DHA molecules are switched to VHF.

8.3 Chain-length dependent growth dynamics of n-alkanes

All of the molecular systems that are investigated in this thesis incorporate alkyl side-chains, which play an important role for the photoresponse of the (nano-)materials. Therefore, it is also useful to study the molecular packing and crystallization of n-alkanes.

In what follows, we present a comparative real-time and *in situ* study of the thin

film growth of the three n-alkanes $C_{36}H_{74}$,$C_{40}H_{82}$ and $C_{44}H_{90}$ on SiO_2. We show that in the case of n-alkanes on SiO_2, a smaller interlayer-transport leads to a greater roughness of the final film. Films consisting of longer molecules exhibit faster roughening in multilayer growth. While all three films mainly consist of upright standing molecules (σ-orientation), a chain-length dependent amount of lying-down molecules (λ-orientation) is found within the upper region of each film. This result has also some technological relevance, because smooth thin films of long n-alkanes can be used as passivation layers in organic field effect transistors, where they significantly improve the transport and mobility of charge carriers. [216]

Experiments in the past have shown that even minimal changes of the chain-length of n-alkanes can lead to large changes of molecular orientation and completely different thermodynamic behavior. While in the regime of shorter n-alkanes (carbon number $n \leq 22$), it has been observed that molecules with fewer carbon atoms form a more disordered molecular structure, less is known about the multilayer ordering behavior of n-alkanes with medium length ($36 \leq n \leq 50$). Parameters such as the persistence length and the intramolecular degrees of freedom of the molecules are supposed to play a major role in the film growth process of longer and thus more flexible n-alkanes. [217,218] We use three different n-alkanes ($C_nH_{2n+2} := C_n$) shown in Figure 8.7a, with even carbon numbers, namely n-hexatriacontane ($C_{36}H_{74}$), n-tetracontane ($C_{40}H_{82}$) and n-tetratetracontane ($C_{44}H_{90}$) to study the influence of chain-length on molecular growth and thin film structure.
While the system has been studied as a model for wetting and dewetting, we emphasize that growth is a kinetic process with a multitude of physical processes happening at the same time. In this case, we are particularly interested in the role of interlayer-transport of molecules. Interlayer-transport denotes the process of molecules hopping from one layer into the next lower layer during organic thin film growth (see Figure 8.7c). This process can either be governed by the diffusivity of molecules or by the height of the energy barrier that molecules have to overcome when hopping from one into another layer (Ehrlich-Schwoebel barrier, [219–221] Figure 8.7b). Optical and X-ray real-time methods are particularly suited to monitor the growth dynamics such as transitions in growth mode, interlayer-transport and roughening, since the growth of organic thin films usually is a non-equilibrium process. [222–226] After the growth process has stopped, many organic systems undergo structural changes, for example dewetting. [227, 228]

In the last two decades, organic molecular beam deposition (OMBD) has proven to

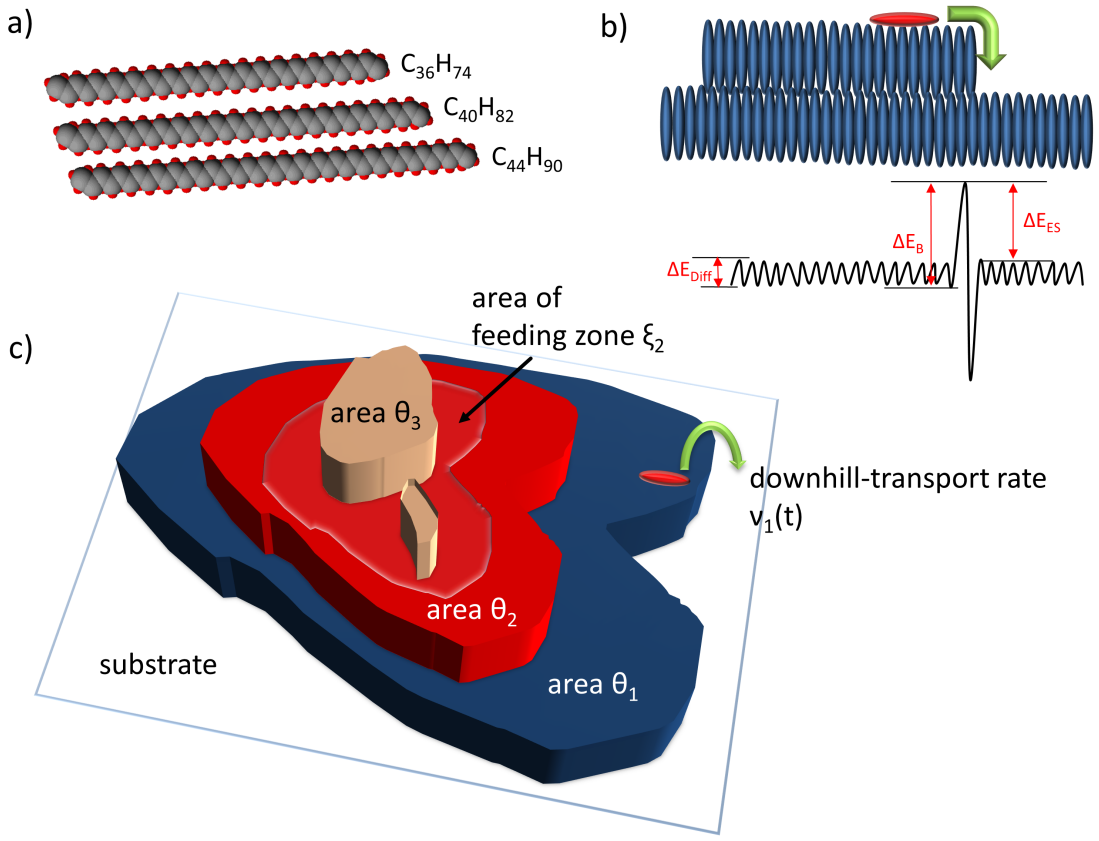

Figure 8.7: (a) Atomic structure of n-tetratetracontane (C_{44}), n-tetracontane (C_{40}) and n-hexatriacontane (C_{36}). (b) Sketch of the Ehrlich-Schwoebel barrier for the case of a single molecule diffusing across a layer of upright standing molecules. ΔE_{Diff} denotes the diffusion barrier that molecules have to overcome when moving from one spot to another spot nearby within the same layer, ΔE_B marks the step-edge barrier that molecules have to overcome when diffusing from one layer into the next lower layer. The Ehrlich-Schwoebel barrier is then defined as the difference $\Delta E_{ES} = \Delta E_B - \Delta E_{Diff}$. (c) Illustration of the growth process. θ_1, θ_2 and θ_3 denote the layer coverage of the first, the second and the third layer. ξ_2 denotes the feeding zone of the second layer, and ν_1 describes the downhill-transport of molecules from the second into the first layer.

be a attractive technique to produce high crystalline thin films of organic molecules on surfaces [229]. But the process is still far from being completely understood. The process of depositing molecules on surfaces is a very complex one with several events and effects occurring at the same time. A big difference compared to single atom growth is the finite size of the molecules and the resulting additional orientational degrees of freedom which makes it more difficult to describe the nucleation process. The main processes happening during organic thin film growth are (see also fig. 8.8):

1. **Adsorption** - as the evaporated molecules reach the substrate they condense on the surface and are therefore able to interact with neighboring molecules.

2. **Nucleation** - molecular nucleation is particularly driven by Van-der-Waals forces interacting between molecules and starts at energetically favorable sites such as step edges or defects within the substrate surface. There is a critical cluster or island size that has to be reached before crystallization takes place. That means islands remain unstable to dissociation until they reach that critical size. Depending on the investigated system and the deposition parameters, a dendritic or a more compact island shape might be favored [230].

3. **Intralayer-diffusion** - Surface diffusion is a random-walk like process that involves the motion of molecules at solid material surfaces. One has to distinguish between hetero-diffusion and self-diffusion. While *hetero-diffusion* describes the movement of molecules directly on the substrate, self-diffusion is the process of molecules moving on top of other molecules. Another distinction can be made between intra-layer and inter-layer diffusion, describing the molecular transport within one layer or from one to another layer respectively. The diffusivity can be quantified by a surface diffusion length λ_D.

4. **Desorption** - some molecules have enough kinetic energy to overcome the energy barrier that holds them on the surface. From a certain temperature on, the desorption process dominates the adsorption process.

For most technical applications, layer-by-layer growth is the desired growth mode as it provides the smoothest and most homogeneous films. But in reality most organic systems exhibit the layer-plus-island growth mode.

Film growth and real-time scattering

The molecules were evaporated from a Knudsen cell attached above the substrate. [231] The growth rate was set to 10 Å/min as monitored by a crystal quartz

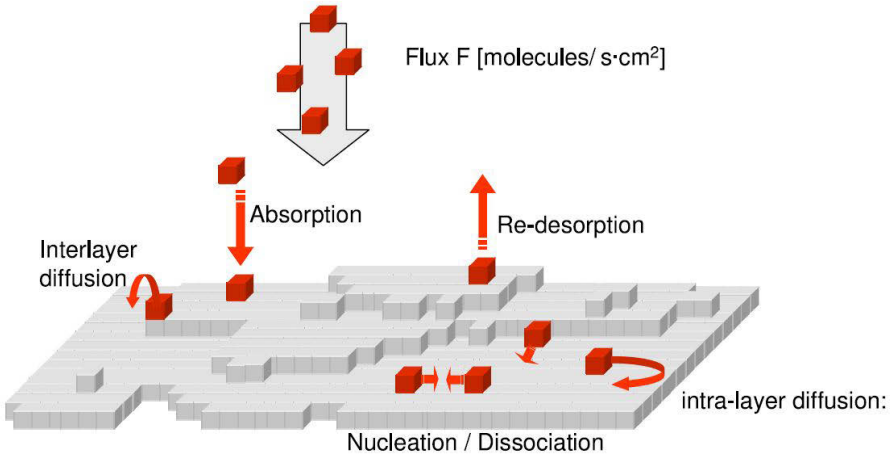

Figure 8.8: Effects occurring during molecular beam deposition (picture taken from ref [229])

microbalance. In the case of C_{44} the growth rate of the first two monolayers dropped temporarily below 3 Å/min, but during the growth of the second monolayer it was increased and stabilized to 10 Å/min again. The substrate temperature was measured at two spots inside and outside the sample holder and was set to 34°C (average of temperatures at both spots). The real-time X-ray reflectivity measurements were performed using a portable UHV chamber [232] at the BESSY II synchrotron source at the energy-dispersive reflectivity (EDR) beamline. [233] The technique of energy dispersive detection makes it possible to measure the X-ray reflectivity within a wide q-range without moving the sample and can thus provide good temporal resolution. [234, 235] The white synchrotron X-ray beam (5 to 30 keV) was reflected on the sample and detected by an energy dispersive Roentec Xflash 1000 detector that provided an energy resolution of about 200 eV. The time-resolution of about 30 s was limited by the intensity of the scattered signal needed for a signal-to-noise ratio of > 100. The angle of incidence was set to 0.386°. At this fixed angle of incidence the monolayer-Bragg reflection (002) of C_{36} can be found at a photon energy of 19.6 keV, while in the case of C_{40}, the (002)-Bragg reflection appears at 17.7 keV and for C_{44} at 16.2 keV. In this way it was possible to use simultaneously photon energies between 8 and 20 keV that provided the highest flux to monitor the region between the monolayer-Anti-Bragg point and the monolayer-Bragg-point in the reciprocal space.

In order to measure a wide energy interval of reflected X-rays with a single X-ray detector simultaneously, we had to adapt the energy spectrum and the intensity of the incoming beam by attenuators made of aluminum. [233] The reflectivity data was normalized for each set of absorbers with the corresponding spectrum of the direct

beam. After the real-time runs the samples were checked for X-ray beam damage by comparing the reflectivity at pristine and exposed spots. Deviations of less than 1 % were visible so that we conclude that our results are not significantly influenced by beam damage within our accuracy. The XRR and GIXD measurements of the final film structure were performed on a lab based diffractometer with a Cu-K_α rotating anode source. The angle of incidence was set to 0.17° for the GIXD measurements and the vertical gap of the detector slits gave an acceptance angle of $\alpha_f < 1°$.

Post-growth studies

The structure as grown for films of thicknesses between 90 and 120 nm has been investigated with X-ray reflectivity (XRR) and grazing incidence X-ray diffraction (GIXD) (see Figure 8.9b). All three n-alkanes show similar in-plane unit cell structures whereas the out of plane lattice spacing differs depending on the length of the molecules, indicating mainly upright-standing molecules with respect to the substrate surface. According to the literature, [139,236] coexistence of an orthorhombic (a=4.96 Å, b = 7.42 Å, c = 95.14 Å, $\alpha = \beta = \gamma = 90°$) and a monoclinic unit cell (a = 5.572 Å, b = 7.420 Å, c = 45.93 Å, $\alpha = \beta = 90°$, $\gamma = 113°$) has been observed for C_{36}, while only orthorhombic unit cells have been observed for C_{40} (a = 4.966 Å, b = 7.430 Å, c = 93.680 Å, $\alpha = \beta = \gamma = 90°$) and C_{44} (a = 4.982 Å, b = 7.427 Å, c = 102.740 Å, $\alpha = \beta = \gamma = 90°$) thus far.

The observed (hk0)-reflections in our GIXD data in Figure 8.9b would not be consistent with a deviation from the 90°-angles of an orthorhombic unit cell by more than 3°. The indexing of the Bragg reflections is in agreement with an orthorhombic $Pca2_1$ unit cell (see Table 8.2) as it has been observed before in bulk and on Si(100) for C_{36} and shorter molecules. From our data we cannot directly conclude a double unit cell, but we follow the literature and use the C_{36} double unit cell, given in reference [236], which is consistent with our data. The $Pca2_1$ unit cell consists of two subcells related by a twofold rotation around the c-axis. For the same sterical reasons we also apply a double unit cell for C_{40} and C_{44}. In the case of C_{40} and C_{44} thin films, the symmetry and c-parameter differ from the Pbca bulk unit cell that has been found in literature. [139, 236, 237] The c-axis of our proposed $Pca2_1$ orthorhombic unit cell equals the height of two monolayers. In this molecular packing structure the (001) reflection is forbidden and only even-numbered higher order reflections are visible.

The Bragg reflection at $q_z = 1.52(4)$ Å^{-1} denoted with $(110)\lambda$ in the XRR graph also appears at exactly the same position in the in-plane measurement. For C_{44} and

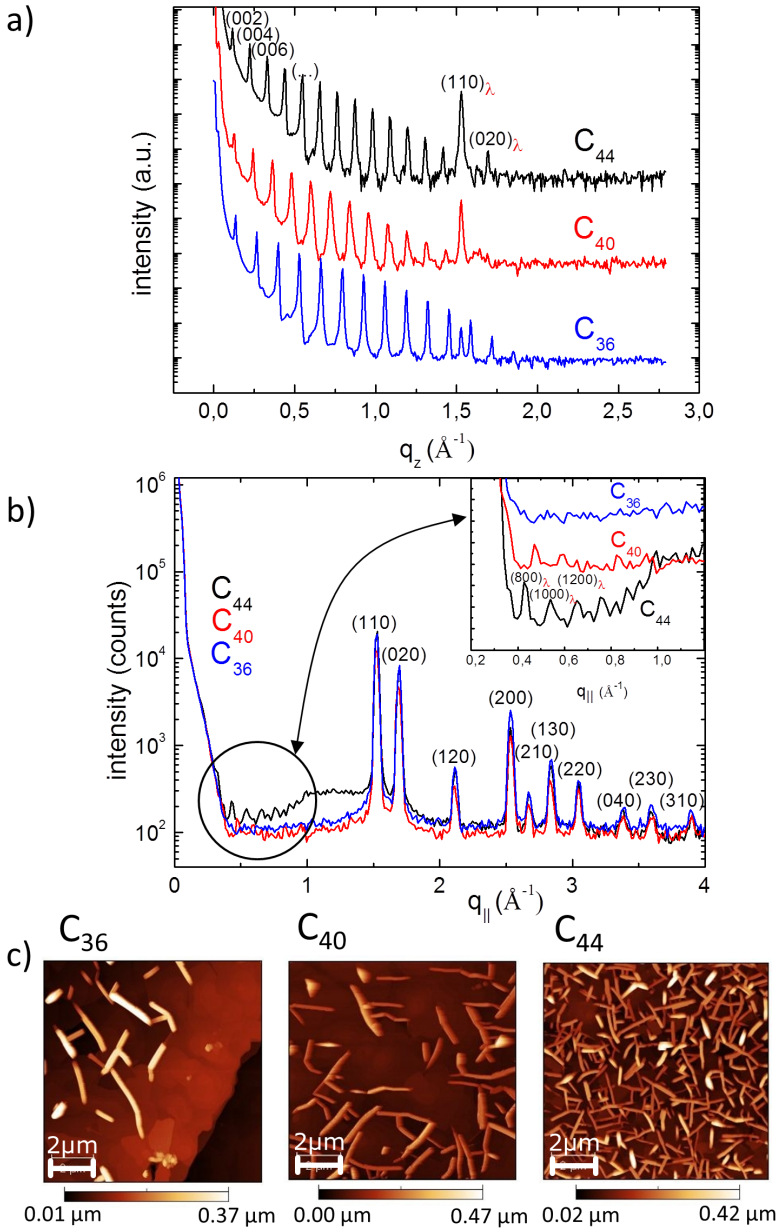

Figure 8.9: (a) X-ray reflectivity, (b) grazing incidence X-ray diffraction and (c) atomic force microscopy scans of C_{36}, C_{40} and C_{44} (shown area $10 \times 10\ \mu m$). The lattice spacings as extracted from the XRR measurements for the monolayer thickness are d = 47.8 Å for C_{36}, d = 52.8 Å for C_{40} and d = 57.6 Å for C_{44}.

C_{40} the (002) reflection and its higher orders are also visible in the GIXD graph. Both these findings point to the fact that there must be a co-existing 90° tilted unit cell that we refer to as the lying-down λ-orientation in contrast to the thermodynamically favorable upright-standing σ-orientation. [238] Both in the XRR and in the GIXD measurements the Bragg reflections of the λ-orientation are considerably stronger for C_{44} than in the case of C_{40} and likewise stronger for C_{40} than for C_{36} (see Figure 8.9b). Under the assumption that all three molecules have similar molecular form factors this suggests that longer molecules form a higher percentage of λ-orientation. For shorter n-alkanes with chain-lengths between 23 and 27 carbon atoms, this behavior has been observed before. [237]

Unit cell parameters under the assumption of an orthorhombic cell for the three investigated n-alkanes as determined from the Bragg reflections in the XRR and GIXD data:

	a	**b**	**c**	$\boldsymbol{\alpha}$	$\boldsymbol{\beta}$	$\boldsymbol{\gamma}$
$\mathbf{C_{36}H_{74}}$	4.98 Å	7.44 Å	95.6 Å	90°	90°	90°
$\mathbf{C_{40}H_{82}}$	4.98 Å	7.44 Å	105.6 Å	90°	90°	90°
$\mathbf{C_{44}H_{90}}$	4.98 Å	7.44 Å	115.2 Å	90°	90°	90°

(8.2)

AFM measurements, performed by Christian Frank at the University of Tübingen, in combination with GIXD scans using various angles of incidence revealed that the biggest amount of λ-orientation is concentrated in the topmost region of the film. At lower angles of incidence corresponding to a smaller penetration depth into the film, the Bragg reflections of the λ-orientation became more dominant compared to the reflections of the σ-orientation. This indicates that the needle-like structures that can be seen on top of the film in the AFM scans are indeed crystallites of λ-orientated molecules. This result is consistent with theoretical findings by Yamamoto et al. [238] The AFM-height of these crystallites (100 - 400 nm) indicates that the absolute number of layers with λ-orientated molecules exceeds the number of layers of the σ-orientation. This explains the strong $(110)_\lambda$ Bragg reflections in XRR scans as shown in Figure 8.9a. The AFM scans shown in Figure 8.9c confirm the findings from the X-ray data and show that C_{44} forms indeed the highest percentage of λ-orientation while C_{36} forms the lowest percentage of λ-orientation of the three compared alkanes.

From X-ray rocking scans at the $(110)_\lambda$ reflection (see Figure 8.10), we can conclude that the λ-orientation consists of crystallites with a high mosaicity (FWHM $\gg 1°$) as compared to the σ-orientation that exhibits a very low mosaicity in the

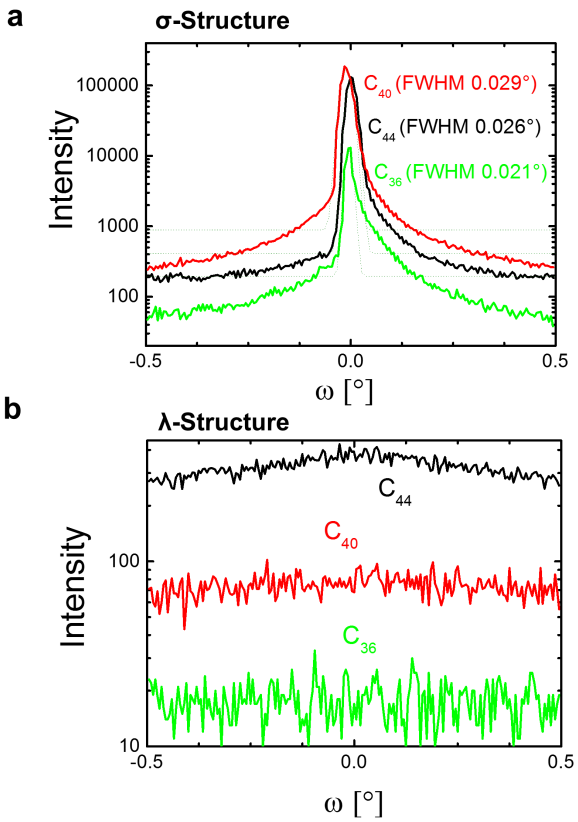

Figure 8.10: (a) Rocking scans of the σ-structure, corresponding to upright-standing molecules of C_{36}, C_{40} and C_{44} on oxidized silicon wafers. (b) Rocking scans of the λ-structure, corresponding to lying-down molecules.

order of the substrate width (FWHM of (002)-reflection $< 0.03°$).

Real-time studies during growth

It has been proposed that the higher mobility of shorter n-alkanes makes it easier for them to crystallize into the thermodynamically more favorable σ-orientation. Time-resolved X-ray measurements during growth allow us to follow the growth dynamics and thereby can help to support this conjecture or yield alternative explanations. The suitability of measuring the X-ray reflectivity at the so called Anti-Bragg point in reciprocal space to study layer-by-layer growth has been demonstrated for several organic systems. [190, 222, 239–241]

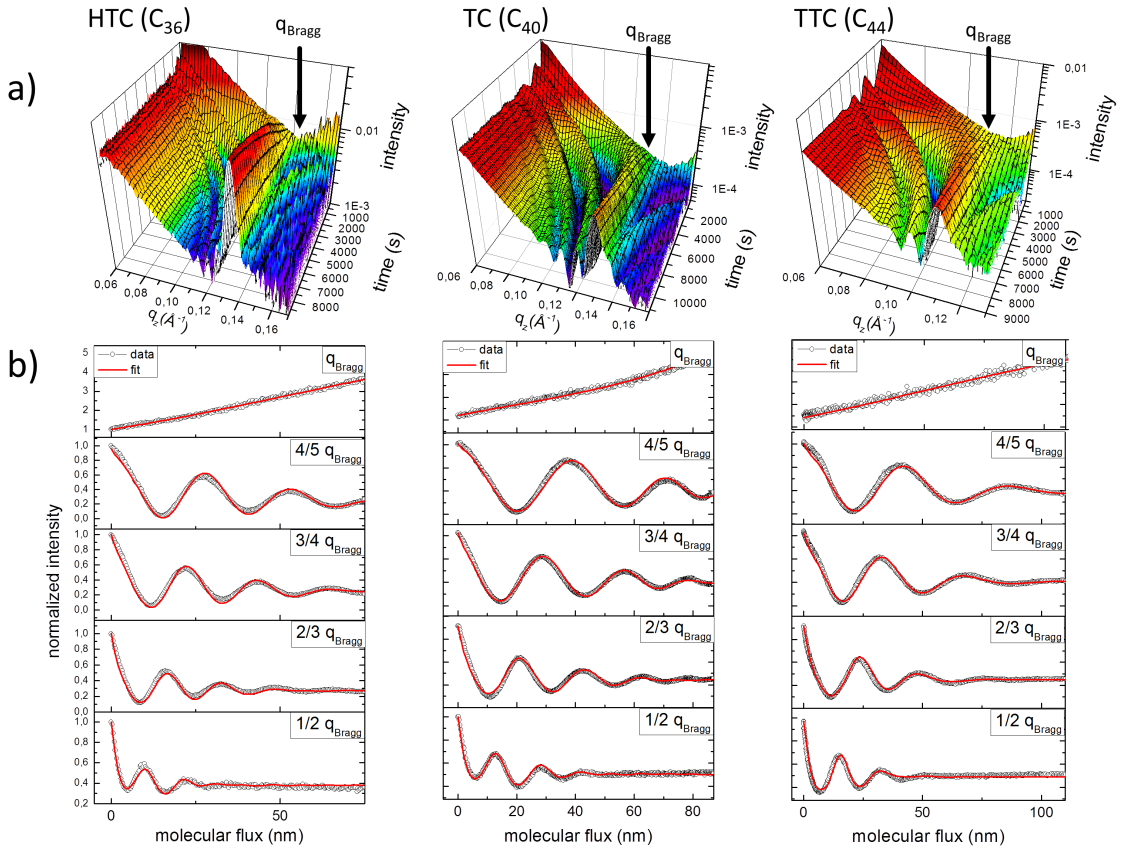

Figure 8.11: (a) Evolution of the specular reflectivity as a function of time and q_z during growth of C_{36}, C_{40} and C_{44} on oxidized silicon wafers. (b) Cuts through the above 3D graph at fixed $q_z = 1/2\ q_{Bragg}$, $2/3\ q_{Bragg}$, $3/4\ q_{Bragg}$, $4/5\ q_{Bragg}$, and q_{Bragg} result in experimental growth oscillation shown in black. Red lines show a simultaneous fit at five distinct values of q_z, using the Trofimov model.

Layer interference leads to temporal oscillations of the reflected intensity during

layer-by-layer growth. [241, 242] This can be seen directly from the equation for the reflected intensity $I_{reflected}(t)$, as calculated in kinematic approximation (see also Figure 8.12):

$$I_{reflected}(t) = \left| A_{substrate}(q_z) \cdot e^{i\phi(q_z)} + f(q_z) \cdot \sum_n \theta_n(t) e^{inq_z d} \right|^2 .$$

$A_{substrate}(q_z)$: substrate scattering amplitude

$f(q_z)$: molecular form factor

$\phi(q_z)$: phase between substrate and ad-layer scattering

n : layer number

θ_n : fractional coverage of the n'th layer

q_z : X-ray wavevector transfer upon reflection

d : lattice spacing in z-direction.

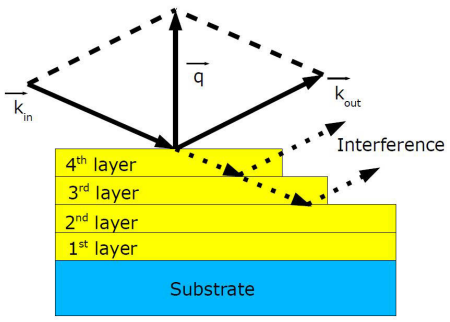

Figure 8.12: Oscillations in the real-time XRR can occur during layer-by-layer growth due to interference of reflected X-rays.

Figure 8.11 shows the temporal evolution of the X-ray reflectivity of C_{36}, C_{40} and C_{44}. In the following, q_{Bragg} denotes the monolayer-Bragg point at q_z=0.111 Å^{-1} for C_{36}, q_z = 0.121 Å^{-1} for C_{40} and q_z=0.134 Å^{-1} for C_{44}. The monolayer-Anti-Bragg point equals the (001)-Bragg-point of the proposed $Pca2_1$ unit cell whose long c-axis equals the height of two monolayers. Since the (001) reflection is forbidden, no additional scattering intensity from the (001) reflection is observed during the measurement of the Anti-Bragg oscillations. From the damping of the intensity oscillations at the (monolayer-)Anti-Bragg point (1/2 q_{Bragg}) after 4 monolayers (ML) one can conclude the occurrence of a transition from layer-by-layer growth to island growth accompanied by roughening, which is typical for Stranski-Krastanov growth of organic molecules. As the growth proceeds, Laue oscillations develop in the region between the Anti-Bragg and Bragg point, indicating a good degree of coherent ordering across the full film thickness. When the temporal intensity oscillations of

all three molecules are compared, a chain-length dependence for the growth behavior can be found. In particular the growth oscillations of the longest molecule C_{44} are damped more than the oscillations of C_{36} and C_{40}, e.g. in the case of C_{40} four oscillations are visible at 2/3 q_{Bragg} while there are only two or three oscillations for C_{44}. This suggests that films consisting of the longest molecule C_{44} exhibit the fastest roughening.

The quantitative evaluation of real-time X-ray data requires the use of a model describing the growth process to determine the temporal evolution of the layer coverage $\theta_n(t)$. Numerous models have been developed over the last several decades to describe the growth of thin films. [227, 243] In contrast to some of the simpler layer-coverage-based models, the growth model developed by Trofimov et al. [244–247] allows us, within the assumptions of the model, to extract real, physical parameters such as the ratio of molecular diffusivity to the incident flux of molecules and facilitates comparison of experimental data with theoretical predictions. The main assumptions of the Trofimov model are as follows. Complete condensation of evaporated molecules on the surface is assumed (no re-evaporation from the surface). Islands consisting of two or more molecules are assumed to be stable and immobile (only single molecules can diffuse). Furthermore uphill-transport, long-range interactions, and multilayer diffusion, *e.g.*, molecules diffusing directly from the 3rd into the 1st layer, are excluded. In this way the amount of parameters needed to describe the growth and nucleation process can be reduced significantly. In this work, we apply the Trofimov model to fit the X-ray reflectivity simultaneously at 5 distinct points of reciprocal space, namely at 1/2 q_{Bragg}, 2/3 q_{Bragg}, 3/4 q_{Bragg}, 4/5 q_{Bragg} and q_{Bragg} (see Figure 8.11b).

As we are concerned only with out-of-plane structure, we use a simplified version of the original Trofimov model, describing the growth process only via the growth rate R_n and the effective critical layer coverage of each layer as shown in eq.8.3-8.5. This version of the Trofimov model has already been successfully applied to the growth of pentacene and diindenoperylene. The critical layer coverage of the n'th layer $\theta_{(n,cr)}$ gives the coverage θ_n of a layer before the n+1'th layer starts to nucleate and grow on top of the n'th layer. [248] The feeding zone parameter ξ_n marks the size (in units of normalized coverage) of the zone on top of the n'th layer where molecules will contribute to nucleation and growth of the n+1'th layer as opposed to the region outside the feeding zone where molecules will diffuse over the edge into the n'th layer (see Figure 8.7c).

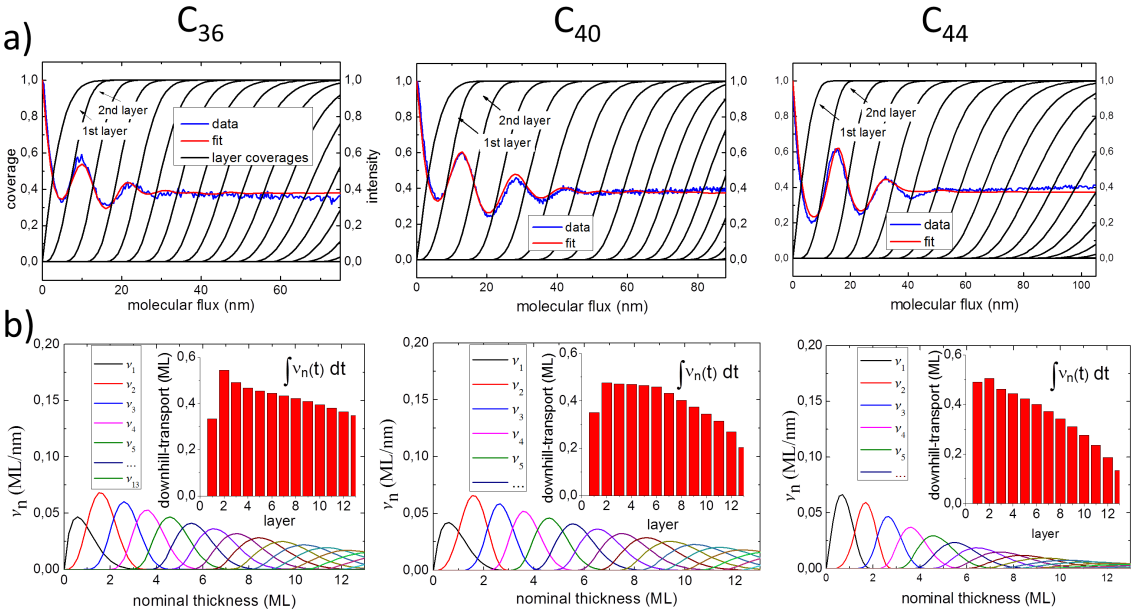

Figure 8.13: (a) Layer coverage and (b) downhill-transport rates for C_{36}, C_{40} and C_{44} (from left to right). The insets in (b) show the integral downhill-transport for each layer, in other words the total amount of molecules that are transported from a specific layer into the next lower layer.

$$\frac{d\theta_n}{dt} = \begin{cases} R_1(1-\theta_1) + R_{n>1}(\theta_1 - \xi_1), n = 1 \\ R_{n>1}(\xi_{n-1} - \xi_n), n > 1, \end{cases} \tag{8.3}$$

with the size of the feeding zone given by

$$\xi_n = \begin{cases} 0, \theta_n < \theta_{cr,n} \\ 1 - e^{-\left[\sqrt{-ln(1-\theta_n)} - \sqrt{-ln(1-\theta_{cr,n})}\right]^2} \end{cases} \tag{8.4}$$

The critical layer coverage parameters in eq.8.4 are calculated via

$$\theta_{n,cr} = \theta_{2,cr} e^{(-n-2)/N_c} \text{ for } n > 2. \tag{8.5}$$

The fit of only the Anti-Bragg oscillations is in some cases overdetermined by the seven fit parameters, that is, the fit parameters could be ambiguous. Fitting simultaneously at five distinct points in reciprocal space simultaneously restricts the range of the fit parameters and therefore gives a better estimate. Besides, additional information is contained within the oscillations closer to the Bragg reflection. At 1/2 q_{Bragg} the oscillations are completely damped after about 4 monolayers (ML) and no information about the growth dynamics beyond that point can be extracted. But at q_z-values closer to the Bragg reflection like 4/5 q_{Bragg} the XRR intensity keeps on

oscillating, yielding information about the critical layer coverage and growth rate up to thicknesses of 10-20 ML.

Two slightly different sticking coefficients for the first monolayer adsorbed directly on the substrate and all subsequent layers have been introduced to take different substrate-molecule and molecule-molecule interaction mechanisms into account, [249] while for C_{40}, a slightly accelerated growth rate for higher layers has been put into the model to deal with the changing growth oscillation periodicity towards the end of the growth. The layer thickness parameter d has been kept constant, that is, the molecular tilt angle is assumed not to change. The fitted layer coverage can be seen in Figure 8.13a, also indicating a stronger layer-by-layer growth behavior in the early stages of the growth. In the later stages of the growth many layers get filled at the same time, indicating island growth and roughening.

For a quantitative comparison of the growth behavior of the three molecules, we compare physical parameters derived from the fitted layer coverage, such as the amount of molecules diffusing from one layer into lower layers during growth. The downhill-transport rate $\nu_n(t) = [\theta_n(t) - \xi_n(t)] \cdot R_n$, shown in Figure 8.13b, describes the amount (in ML) of molecules diffusing from the n+1'th into the n'th layer per time interval. The total amount of molecules diffusing from the n+1'th into the n'th layer is shown in the insets in Figure 8.13b. In the case of C_{36} and C_{40}, a rather small critical layer coverage (< 20 %) of the first monolayer yields a comparatively small downhill-transport from the second into the first layer. For C_{44} the first two layers grow in a smoother way, indicated by a larger downhill-transport from the second to the first layer. After growth of about 5 ML, the integral downhill-transport of the longer molecules drops below the integral downhill-transport of the shorter molecules. This chain-length dependence becomes even more significant as the growth proceeds. For thicknesses above 10 ML, the integral downhill-transport of C_{36} exceeds the integral downhill-transport of C_{44} by about 60 % (see Figure 8.13b). This indicates that the length of a molecule is crucial for its interlayer-transport properties, particularly within the roughening regime.

The small critical layer coverage parameters (< 0.3) that have been derived for all three molecules indicate a substantial Ehrlich-Schwoebel barrier, limiting the downhill-transport probability. [219] The probability of molecules diffusing from the n+1'th layer into the n'th layer is in this case related to the Ehrlich-Schwoebel barrier E_{ES} as follows

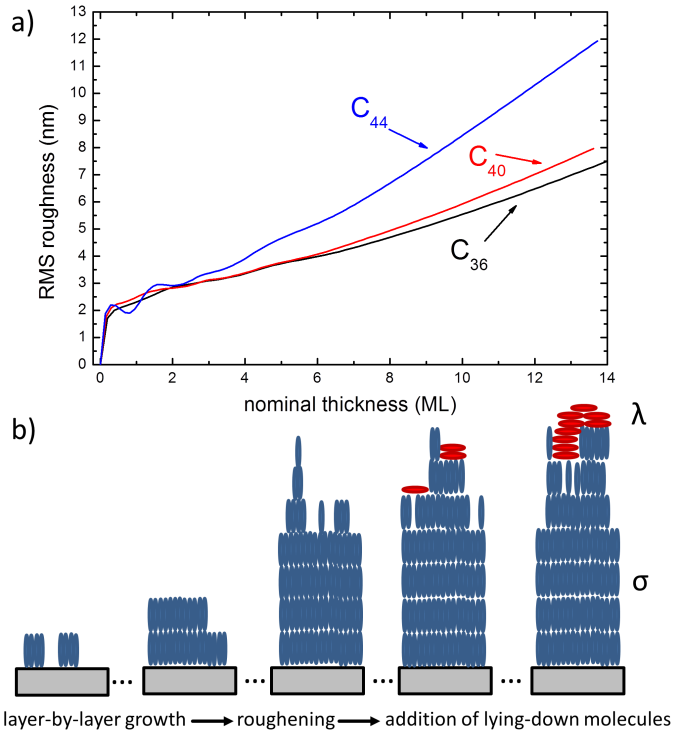

Figure 8.14: (a) Evolution of the interface roughness during growth of C_{36}, C_{40} and C_{44} and b) sketch of the transition of the growth mode and the formation of λ-orientation within the topmost region of the film.

$$p_n = \frac{\nu_n(t)}{R_n \cdot [\theta_n(t) - \theta_{n+1}(t)]} \propto A_n(t) \cdot e^{-E_{ES}/kT} \tag{8.6}$$

with A_n being a factor depending on the island perimeters and the diffusivity of the molecules. [220, 250, 251] Averaging the time-dependent probability of eq.8.6 by integrating from the beginning of the growth of the n'th layer $t(\theta_n = 0)$ to the filling of the n+1'th layer $t(\theta_{n+1} = 1)$ and dividing by the time interval makes it possible to simplify the above relation to

$$\overline{p_n} \propto \overline{A_n} \cdot e^{E_{ES}/kT}, \tag{8.7}$$

where $\overline{p_n}$ denots the *mean* downhill-transport probability. According to this, and for film thicknesses above 5 ML, the mean probability of downhill-transport is about 34% for C_{36}, 31% for C_{40} and only 28% for the longest molecule, C_{44}.

While the absolute value for E_{ES} is not easy to establish reliably, we can estimate the differences of E_{ES} between the different chains, namely C_{36}, C_{40} and C_{44}, assuming that they can all be similarly well described by our model. Further we assume that the island perimeters and intra-layer diffusion barriers, and thus the

prefactors $\overline{A_n}$ are similar for all three molecules. According to this estimate and for film thicknesses > 5 ML, C_{40} molecules hopping from one layer into the next lower have to overcome an Ehrlich-Schwoebel barrier that exceeds the corresponding Ehrlich-Schwoebel barrier of C_{36} by about $\Delta E_{ES} = E_{ES}(C_{40}) - E_{ES}(C_{36}) = 2$ meV, while C_{44} molecules have to overcome a barrier that exceeds the barrier of C_{36} by approximately $\Delta E_{ES} = E_{ES}(C_{44}) - E_{ES}(C_{36}) = 5$ meV. In other words, in this regime the increase of the Ehrlich-Schwoebel barrier per additional carbon atom is of the order of 0.5 meV under the above approximations.

The chain-length dependent downhill-transport and the chain-length dependent percentage of λ-orientation in the topmost region of the film suggest that there might also be a chain-length dependence of the film roughness. The root-mean-square roughness of the film can be calculated directly from the layer coverage as given by the Trofimov model fit via

$$\sigma(t) = \sqrt{\sum_{n=0}^{\infty} \left(\theta_n(t) - \theta_{n+1}(t)\right) \left[d \cdot n - \overline{d}(t)\right]^2} \tag{8.8}$$

with $\theta_n(t)$ being the fractional coverage of the n'th layer, d the lattice spacing and $\overline{d}(t)$ being the nominal film thickness. [231] In Figure 8.14a, the roughness evolution during thin film growth is shown for all three molecules. C_{44} exhibits the smoothest layer-by-layer growth during the first two monolayers, indicated by oscillations of the roughness evolution. After evaporation of about 4 ML there is a strong increase of roughness. Despite the smooth growth in the beginning, C_{44} exhibits by far the fastest roughening after 4 ML, and C_{40} roughens faster than C_{36}, but the differences between the latter two are within our error bars. Therefore we conclude that the observed chain-length dependent roughening is a consequence of the chain-length dependent interlayer-transport properties and Ehrlich-Schwoebel barriers. This behavior is different from the corresponding chain-length dependent behavior in the case of small molecules where shorter chains form more disordered structures. In the past, simulations have shown that, indeed, a greater downhill-transport is expected to support layer-by-layer growth while a smaller downhill-transport of molecules probably leads to faster roughening. [239] Nevertheless, in order to get a thorough understanding of the molecular kinetics governing the growth process, additional real-time studies are required, e.g. measurements of the in-plane island perimeters, performed at different temperatures, to determine reliable absolute values of E_{ES}.

Conclusion

A comparative real-time and in situ growth study of the three n-alkanes C_{36}, C_{40} and C_{44} on SiO_2 has been performed using energy dispersive real-time X-ray reflectivity. It has been shown that structural properties of organic thin films consisting of chain-like molecules can be tuned significantly by varying the number of chain segments. While all three molecules align mostly in upright-standing geometry, longer molecules form more crystallites of lying-down molecules in the topmost region of the film. Furthermore, films made of longer molecules exhibit faster roughening than films consisting of shorter molecules. This can be explained by the chain length dependence of the downhill-transport rates during the growth. The amount of molecules diffusing from one layer into the next lower layer decreases with increasing chain-length of the molecules. Assuming that the thermal activation over the Ehrlich-Schwoebel barrier limits the downhill-transport probability during the later stages of the growth, [219, 250] we conclude from the derived downhill-transport rates that there must also be a chain-length dependence of the Ehrlich-Schwoebel barrier, with longer molecules having a higher energy barrier to overcome when diffusing from one layer into the next lower layer. This would be in agreement with simulations for several organic molecules performed by Goose et al. [221] Our results show that it is preferable to use shorter molecules for any application where a smooth interlayer is required and coexistence of two different molecular orientations (lying-down/upright-standing) has to be avoided.

9 Author Contributions

Peer reviewed publications:

1. *Light-Controlled 'Molecular Zippers' Based on Azobenzene Main Chain Polymers.*
   C. Weber, T. Liebig, M. Gensler, L. Pithan, S. Bommel, D. Bléger, J.P. Rabe, S. Hecht, and S. Kowarik, **Macromolecules 48, 1531 (2015)**.

2. *Cooperative switching behavior in nanofibers of azobenzene oligomers.*
   C. Weber, T. Liebig, M. Gensler, D. Bléger, J.P. Rabe, S. Hecht, and S. Kowarik, **submitted**

3. *Chain-length dependent growth dynamics of n-alkanes on silica investigated by energy-dispersive x-ray reflectivity in situ and in real-time*
   C. Weber, C. Frank, S. Bommel, T. Rukat, W. Leitenberger, P. Schäfer, F. Schreiber, and S. Kowarik, **J. Chem. Phys. 136, 204709 (2012)**.

4. *Unravelling the multilayer growth of the fullerene C60 in real time.*
   S. Bommel, N. Kleppmann, **C. Weber**, H. Spranger, P. Schäfer, J. Novak, S.V. Roth, F. Schreiber, S.H.L. Klapp, and S. Kowarik, **Nat. Commun. 5, 5388 (2014)**.

5. *Light Controls Polymorphism in Thin Films of Sexithiophene.*
   L. Pithan, C. Cocchi, H. Zschiesche, **C. Weber**, A. Zykov, S. Bommel, S.J. Leake, P. Schäfer, C. Draxl, and S. Kowarik, **Cryst. Growth Des. 15, 1319 (2015)**.

6. *Formation of carboxy- and amide-terminated alkyl monolayers on Silicon(111) investigated by ATR-FTIR, XPS, and X-ray scattering: construction of photoswitchable surfaces.*
   K. Rück-Braun, M.Å. Petersen, F. Michalik, A. Hebert, D. Przyrembel, **C. Weber**, S.A. Ahmed, S. Kowarik, and M. Weinelt, **Langmuir 29, 11758 (2013)**.

7. *Controlling the growth mode of para-sexiphenyl (6P) on ZnO by partial fluorination.*
   M. Sparenberg, A. Zykov, P. Beyer, L. Pithan, **C. Weber**, Y. Garmshausen, F. Carlà, S. Hecht, S. Blumstengel, F. Henneberger, and S. Kowarik, **Phys. Chem. Chem. Phys. 16, 26084 (2014)**.

8. *Real-time and in-situ x-ray scattering during the growth of C_{60} on mica.*
   S. Bommel, **C. Weber**, J. Novak, P. Schäfer, S.V. Roth, S. Kowarik, **HASYLAB Annual Report 2011**

9. *Thermally-activated post-growth dewetting of the fullerene C_{60} on mica.* S. Bommel, H. Spranger, **C. Weber**, N. Kleppmann, S.V. Roth, S.H.L. Klapp, S. Kowarik, **submitted**

10. *Interface and crystal engineering of n-alkane thin films by annealing.*
    L. Pithan, E. Meister, C. Jin, **C. Weber**, A. Zykov, K. Sauer, W. Brütting, H. Riegler, A. Opitz, S. Kowarik, **submitted**

11. *Identification of an organic semiconductor superlattice structure of pentacene and perfluoro-pentacene through resonant and non-resonant X-ray scattering.*
    S. Kowarik, A. Hinderhofer, C. Wang, **C. Weber**, A. Gerlach, S.R. Leone, A. Hexemer, F. Schreiber, **submitted**

Conference talks:

1. **8'th Autumn School on X-ray Scattering from Surfaces and Thin Layers, Smolenice 2011:** Energy-Dispersive Real-Time and In Situ X-Ray Investigations of Organic Thin Film Growth.

2. **Frühjahrstagung der Deutschen Physikalischen Gesellschaft, Dresden 2014:** Reversible light-induced changes in spin-coated thin films of Azobenzene-polymers.

3. **Frühjahrstagung der Deutschen Physikalischen Gesellschaft, Berlin 2015:** Light-Controlled Molecular Zippers based on Azobenzene Main Chain Polymers.

4. **Spring Meeting of the Material Research Society, San Francisco 2015:** Light-Controlled Molecular Zippers based on Azobenzene Polymers.

Poster presentations:

1. **Frühjahrstagung der Deutschen Physikalischen Gesellschaft, Dresden 2011:** Real-Time Growth Studies of Organic-Inorganic Semiconductor Hybrid-Structures.

2. **Frühjahrstagung der Deutschen Physikalischen Gesellschaft, Berlin 2012:** In Situ Growth Studies of n-Alkanes on Silica with Real-Time X-Ray Methods.

3. **Frühjahrstagung der Deutschen Physikalischen Gesellschaft, Regensburg 2013:** Epitaxial order of self-assembled monolayers with attached molecular switches on Si(111) investigated using X-ray diffraction.

4. **International Symposium on Photochromism, Berlin 2013:** Self-assembled monolayers with molecular switches on Si(111), investigated by grazing incidence x-ray diffraction and x-ray reflectivity.

10 List of Acronyms

2D	2-Dimensional
3D	3-Dimensional
AFM	Atomic Force Microscopy
BESSY	Berliner Elektronenspeicherring-Gesellschaft fÃijr Synchrotronstrahlung
DRS	Differential Reflectance Spectroscopy
GIXD	Grazing Incidence X-Ray Diffraction
LC	Liquid Crystal
LCN	Liquid Crystal Network
LED	Light Emitting Diode
ML	Monolayer
OBMD	Organic Molecular Beam Deposition
PET	Polyethylene
PSI	Paul Scherrer Institut
RMS	Root Mean Square
SAM	Self-Assembled Monolayer
SLS	Swiss Light Source
STM	Scanning Tunneling Microscopy
UHV	Ultra High Vacuum
UV	Ultraviolet
XRR	X-Ray Reflectivity
XRD	X-Ray Diffraction

List of Figures

Bibliography

[1] T. Quirk, "There's plenty of room at the bottom," in *Australasian Biotechnology*, vol. 16, p. 36, 2006.

[2] H. Dürr and H. Bouas-Laurent, eds., *Photochromism. Molecules and Systems.* Amsterdam: Elsevier, 2003.

[3] M. Peplow, "The tiniest Lego: a tale of nanoscale motors, rotors, switches and pumps," *Nature*, vol. 525, pp. 18–21, 2015.

[4] Z. F. Liu, K. Hashimoto, and A. Fujishima, "Photoelectrochemical information storage using an azobenzene derivative," *Nature*, vol. 347, pp. 658–660, 1990.

[5] Y. Amamoto, J. Kamada, H. Otsuka, A. Takahara, and K. Matyjaszewski, "Repeatable Photoinduced Self-Healing of Covalently Cross-Linked Polymers through Reshuffling of Trithiocarbonate Units," *Angewandte Chemie International Edition*, vol. 123, pp. 1698–1701, 2011.

[6] P. M. Beaujuge and J. M. J. Fréchet, "Molecular design and ordering effects in π-functional materials for transistor and solar cell applications.," *Journal of the American Chemical Society*, vol. 133, pp. 20009–29, 2011.

[7] T. J. Kucharski, N. Ferralis, A. M. Kolpak, J. O. Zheng, D. G. Nocera, and J. C. Grossman, "Templated assembly of photoswitches significantly increases the energy-storage capacity of solar thermal fuels.," *Nature chemistry*, vol. 6, pp. 441–7, 2014.

[8] W. R. Browne and B. L. Feringa, "Making molecular machines work.," *Nature nanotechnology*, vol. 1, pp. 25–35, 2006.

[9] T. Muraoka, K. Kinbara, Y. Kobayashi, and T. Aida, "Light-driven open-close motion of chiral molecular scissors.," *Journal of the American Chemical Society*, vol. 125, pp. 5612–3, 2003.

[10] T. Mirfakhrai, J. D. Madden, and R. H. Baughman, "Polymer artificial muscles," *Materials Today*, vol. 10, pp. 30–38, 2007.

[11] M. Camacho-Lopez, H. Finkelmann, P. Palffy-Muhoray, and M. Shelley, "Fast liquid-crystal elastomer swims into the dark.," *Nature materials*, vol. 3, pp. 307–10, 2004.

[12] C. L. van Oosten, C. W. M. Bastiaansen, and D. J. Broer, "Printed artificial cilia from liquid-crystal network actuators modularly driven by light.," *Nature materials*, vol. 8, pp. 677–82, 2009.

[13] B. L. Feringa and W. R. Browne, eds., *Molecular Switches*, vol. 51. Weinheim, Germany: Wiley-VCH Verlag GmbH & Co. KGaA, 2. edition ed., 2011.

[14] Z. Sekkat and W. Knoll, *Photoreactive Organic thin Films in the Light of Bound Electromagnetic Waves*. Academic Press, 2002.

[15] F. Krollpfeiffer, C. Mühlhausen, and G. Wolf, "Zur Kenntnis der Lichtempfindlichkeit von Aryl-ß-naphtylamin - azofarbstoffen," *Justus Liebigs annalen der Chemie*, vol. 508, pp. 39–51, 1934.

[16] M.-M. Russew and S. Hecht, "Photoswitches: from molecules to materials.," *Advanced materials*, vol. 22, pp. 3348–60, 2010.

[17] S. C. Warren, O. Guney-Altay, and B. A. Grzybowski, "Responsive and Nonequilibrium Nanomaterials," *The Journal of Physical Chemistry Letters*, vol. 3, pp. 2103–2111, 2012.

[18] A. Coskun, M. Banaszak, R. D. Astumian, J. F. Stoddart, and B. A. Grzybowski, "Great expectations: can artificial molecular machines deliver on their promise?," *Chemical Society Reviews*, vol. 41, p. 19, 2012.

[19] L. Persano, A. Camposeo, and D. Pisignano, "Active polymer nanofibers for photonics, electronics, energy generation and micromechanics," *Progress in Polymer Science*, vol. 43, pp. 48–95, 2014.

[20] P. S. Weiss, "Functional molecules and assemblies in controlled environments: Formation and measurements," *Accounts of Chemical Research*, vol. 41, pp. 1772–1781, 2008.

[21] J. M. Abendroth, O. S. Bushuyev, P. S. Weiss, and C. J. Barrett, "Controlling Motion at the Nanoscale: Rise of the Molecular Machines," *ACS Nano*, 2015.

[22] G. Pace, V. Ferri, C. Grave, M. Elbing, C. V. Hänisch, M. Zharnikov, M. Mayor, M. A. Rampi, and P. Samori, "Cooperative light-induced molecular movements of highly ordered azobenzene self-assembled monolayers," *Proceedings of the National Academy of Sciences of the United States of America*, vol. 104, pp. 9937–9942, 2007.

[23] Y. B. Zheng, B. K. Pathem, J. N. Hohman, J. C. Thomas, M. Kim, and P. S. Weiss, "Photoresponsive molecules in well-defined nanoscale environments.," *Advanced materials*, vol. 25, pp. 302–12, 2013.

[24] C. Gahl, R. Schmidt, D. Brete, E. R. McNellis, W. Freyer, R. Carley, K. Reuter, and M. Weinelt, "Structure and excitonic coupling in self-assembled monolayers of azobenzene-functionalized alkanethiols.," *Journal of the American Chemical Society*, vol. 132, pp. 1831–8, 2010.

[25] M. Utecht, T. Klamroth, and P. Saalfrank, "Optical absorption and excitonic coupling in azobenzenes forming self-assembled monolayers: a study based on density functional theory," *Physical Chemistry Chemical Physics*, vol. 13, p. 21608, 2011.

[26] B. K. Juluri, A. S. Kumar, Y. Liu, T. Ye, Y.-W. Yang, A. H. Flood, L. Fang, J. F. Stoddart, P. S. Weiss, and T. J. Huang, "A Mechanical Actuator Driven Electrochemically by Artificial Molecular Muscles," *ACS Nano*, vol. 3, pp. 291–300, 2009.

[27] S. Pramanik, S. De, and M. Schmittel, "A trio of nanoswitches in redox-potential controlled communication," *Chem. Commun.*, vol. 50, pp. 13254–13257, 2014.

[28] S. Pramanik, S. De, and M. Schmittel, "Bidirectional chemical communication between nanomechanical switches," *Angewandte Chemie International Edition*, pp. 4709–4713, 2014.

[29] D. Ray, J. T. Foy, R. P. Hughes, and I. Aprahamian, "A switching cascade of hydrazone-based rotary switches through coordination-coupled proton relays," *Nature Chemistry*, vol. 4, pp. 757–762, 2012.

[30] A. Whitty, "Cooperativity and biological complexity.," *Nature chemical biology*, vol. 4, pp. 435–439, 2008.

[31] Z. Yu and S. Hecht, "Cooperative switching events in azobenzene foldamer denaturation.," *Chemistry*, vol. 18, pp. 10519–24, 2012.

[32] "Wikipedia." `https://en.wikipedia.org/wiki/Polyethylene`. Accessed: 2015-08-18.

[33] W. Knoll and R. C. Advincula, *Functional Polymer Films*, vol. 1-2. Weinheim, Germany: Wiley-VCH Verlag GmbH & Co. KGaA, 2011.

[34] C. D. Dimitrakopoulos and P. R. L. Malenfant, "Organic thin film transistors for large area electronics," *Advanced Materials*, vol. 14, pp. 99–117, 2002.

[35] D. Braun, "Semiconducting polymer LEDs," *Materials Today*, vol. 5, pp. 32–39, 2002.

[36] R. H. Friend, R. W. Gymer, A. B. Holmes, J. H. Burroughes, R. Marks, C. Taliani, D. D. C. Bradley, D. A. Dos Santos, J. L. Bredas, M. Logdlund, and W. R. Salaneck, "Electroluminescence in conjugated polymers," *Nature*, vol. 397, pp. 121–128, 1999.

[37] N. Robertson, "Organic Photovoltaics. Mechanisms, Materials and Devices. Edited by Sam-Shajing Sun and Niyazi Serdar Sariciftci.," *Angewandte Chemie International Edition*, vol. 45, pp. 7321–7321, 2006.

[38] V. Balzani, A. Credi, and M. Venturi, *Molecular Devices and Machines*. Weinheim, Germany: Wiley-VCH Verlag GmbH & Co. KGaA, Feb. 2008.

[39] G. Zimmerman, L.-Y. Chow, and U.-J. Paik, "The Photochemical Isomerization of Azobenzene," *Journal of the American Chemical Society*, vol. 80, pp. 3528–3531, 1958.

[40] E. Bergmann and A. Weizmann, "Dipole Moments as a Tool in the Determination of Structure.," *Chemical Reviews*, vol. 29, pp. 553–592, 1941.

[41] H. Fliegl, A. Köhn, C. Hättig, and R. Ahlrichs, "Ab initio calculation of the vibrational and electronic spectra of trans- and cis-azobenzene," *Journal of the American Chemical Society*, vol. 125, pp. 9821–9827, 2003.

[42] M. B. Robin, R. R. Hart, and N. A. Kuebler, "Electronic States of the Azoalkanes," *Journal of the American Chemical Society*, vol. 89, pp. 1564–1572, 1967.

[43] M. S. Gordon and H. Fischer, "A molecular orbital study of the isomerization mechanism of diazacumulenes," *Journal of the American Chemical Society*, vol. 90, pp. 2471–2476, 1968.

[44] L. J. Schaad and H. B. Kinser, "Structure of diimide," *The Journal of Physical Chemistry*, vol. 73, pp. 1901–1911, 1969.

[45] N. W. Winter and R. M. Pitzer, "Theoretical description of the diimide molecule," *The Journal of Chemical Physics*, vol. 62, p. 1269, 1975.

[46] J. M. Howell and L. J. Kirschenbaum, "Substituent effects and the cis-trans isomerization of diazenes," *Journal of the American Chemical Society*, vol. 98, pp. 877–885, 1976.

[47] R. N. Camp, I. R. Epstein, and C. Steel, "Theoretical studies of the photochemistry of acyclic azoalkanes," *Journal of the American Chemical Society*, vol. 99, pp. 2453–2459, 1977.

[48] G. Olbrich, "INDO-SCF and CI calculations on the trans-cis isomerization of azomethane in the ground state and in excited states," *Chemical Physics*, vol. 27, pp. 117–125, 1978.

[49] H. Rau and E. Lüddecke, "On the Rotation-Inversion Controversy on Photoisomerization of Azobenzenes. Experimental Proof of Inversion," *Journal of the American Chemical Society*, vol. 104, pp. 1616–1620, 1982.

[50] H. Rau, "Further evidence for rotation in the Pi,Pi* and inversion in the n,Pi* photoisomerization of azobenzenes," *Journal of Photochemistry*, vol. 26, pp. 221–225, 1984.

[51] E. W. G. Diau, "A New Trans-to-Cis Photoisomerization Mechanism of Azobenzene on the S 1(n,Pi*) Surface," *Journal of Physical Chemistry A*, vol. 108, pp. 950–956, 2004.

[52] M. L. Tiago, S. Ismail-Beigi, and S. G. Louie, "Photoisomerization of azobenzene from first-principles constrained density-functional calculations.," *The Journal of chemical physics*, vol. 122, p. 094311, 2005.

[53] C. Ciminelli, G. Granucci, and M. Persico, "Are azobenzenophanes rotation-restricted?," *The Journal of chemical physics*, vol. 123, p. 174317, 2005.

[54] C. R. Crecca and A. E. Roitberg, "Theoretical study of the isomerization mechanism of azobenzene and disubstituted azobenzene derivatives.," *The journal of physical chemistry. A*, vol. 110, pp. 8188–203, 2006.

[55] Y.-W. Hao, H.-Y. Wang, Y.-J. Huang, B.-R. Gao, Q.-D. Chen, L.-B. Li, and H.-B. Sun, "Evidence of concerted inversion for the photon-induced molecular switching of azobenzene using rotation-free azobenzene derivatives," *Journal of Materials Chemistry C*, vol. 1, p. 5244, 2013.

[56] E. M. M. Tan, S. Amirjalayer, S. Smolarek, A. Vdovin, F. Zerbetto, and W. J. Buma, "Fast photodynamics of azobenzene probed by scanning excited-state potential energy surfaces using slow spectroscopy," *Nature Communications*, vol. 6, p. 5860, 2015.

[57] C. G. Morgante and W. S. Struve, "S2-S0 fluorescence in trans-azobenzene," *Chemical Physics Letters*, vol. 68, pp. 267–271, 1979.

[58] H. M. D. Bandara, T. R. Friss, M. M. Enriquez, W. Isley, C. Incarvito, H. A. Frank, J. Gascon, and S. C. Burdette, "Proof for the concerted inversion mechanism in the trans–>cis isomerization of azobenzene using hydrogen bonding to induce isomer locking.," *The Journal of organic chemistry*, vol. 75, pp. 4817–27, 2010.

[59] G. Tiberio, L. Muccioli, R. Berardi, and C. Zannoni, "How does the trans-cis photoisomerization of azobenzene take place in organic solvents?," *ChemPhysChem*, vol. 11, pp. 1018–1028, 2010.

[60] R. J. Maurer and K. Reuter, "Assessing computationally efficient isomerization dynamics: sCF density-functional theory study of azobenzene molecular switching," *Journal of Chemical Physics*, vol. 135, 2011.

[61] L. Schweighauser, D. Häussinger, M. Neuburger, and H. A. Wegner, "Symmetry as a new element to control molecular switches.," *Organic & biomolecular chemistry*, vol. 12, pp. 3371–9, 2014.

[62] S. Hagen, P. Kate, F. Leyssner, D. Nandi, M. Wolf, and P. Tegeder, "Excitation mechanism in the photoisomerization of a surface-bound azobenzene derivative: Role of the metallic substrate," *Journal of Chemical Physics*, vol. 129, 2008.

[63] J. Dokić, M. Gothe, J. Wirth, M. V. Peters, J. Schwarz, S. Hecht, and P. Saalfrank, "Quantum chemical investigation of thermal cis-to-trans isomerization of azobenzene derivatives: substituent effects, solvent effects, and comparison to experimental data.," *The journal of physical chemistry. A*, vol. 113, pp. 6763–73, 2009.

[64] H. Rau, "Photoisomerization of Azobenzenes," in *Photochemistry and Photophysics* (J. F. Rabek, ed.), pp. 119–142, Boca Raton, FL, USA: CRC Press, 2 ed., 1990.

[65] C. S. Paik Sung, L. Lamarre, and M. K. Tse, "Molecular Motion of Polymer Main Chains in the Solid State as Studied by Photoisomerization," *Macromolecules*, vol. 12, pp. 666–669, 1979.

[66] I. Mita, K. Horie, and K. Hirao, "Photochemistry in Polymer Solids. 9. Photoisomerization of Azobenzene in a Polycarbonate Film," *Macromolecules*, vol. 22, pp. 558–563, 1989.

[67] G. Kumar and D. Neckers, "Photochemistry of azobenzene-containing polymers," *Chemical Reviews*, pp. 1915–1925, 1989.

[68] T. Naito, K. Horie, and I. Mita, "Photochemistry in Polymer Solids. 11. The Effects of the Size of Reaction Groups and the Mode of Photoisomerization on Photochromic Reactions in Polycarbonate Film," *Macromolecules*, vol. 24, pp. 2907–2911, 1991.

[69] Y.-Q. Shen and H. Rau, "The environmentally controlled photoisomerization of probe molecules containing azobenzene moieties in solid poly(methylmethacrylate)," *Makromolekulare Chemie*, vol. 192, pp. 945–957, 1991.

[70] K. G. Yager and C. J. Barrett, "Novel photo-switching using azobenzene functional materials," *Journal of Photochemistry and Photobiology A: Chemistry*, vol. 182, pp. 250–261, 2006.

[71] Z. Mahimwalla, K. G. Yager, J.-I. Mamiya, A. Shishido, A. Priimagi, and C. J. Barrett, *Azobenzene photomechanics: prospects and potential applications*, vol. 69. Springer, 2012.

[72] M. Eich, J. H. Wendorff, D. Kunststoff-institut, D. Darmstadt, B. Reck, and H. Ringsdorf, "Reversible digital and holographic optical storage in polymeric liquid crystals," *Macromolecular Rapid Communications*, vol. 63, pp. 59–63, 1987.

[73] D. Y. Kim, S. K. Tripathy, L. Li, and J. Kumar, "Laser-induced holographic surface relief gratings on nonlinear optical polymer films," *Applied Physics Letters*, vol. 66, p. 1166, 1995.

[74] D. Y. Kim, L. Li, X. L. Jiang, V. Shivshankar, J. Kumar, and S. K. Tripathy, "Polarized Laser Induced Holographic Surface Relief Gratings on Polymer Films," *Macromolecules*, vol. 28, pp. 8835–8839, 1995.

[75] C. J. Barrett, A. L. Natansohn, and P. L. Rochon, "Mechanism of Optically Inscribed High-Efficiency Diffraction Gratings in Azo Polymer Films," *Journal of Physics Chemistry*, pp. 8836–8842, 1996.

[76] J. Kumar, L. Li, X. L. Jiang, D.-Y. Kim, T. S. Lee, and S. Tripathy, "Gradient force: The mechanism for surface relief grating formation in azobenzene functionalized polymers," *Applied Physics Letters*, vol. 72, p. 2096, 1998.

[77] N. K. Viswanathan, D. Y. Kim, S. Bian, J. Williams, W. Liu, L. Li, L. Samuelson, J. Kumar, and S. K. Tripathy, "Surface relief structures on azo polymer films," *Journal of Materials Chemistry*, vol. 9, pp. 1941–1955, 1999.

[78] S. Bian, J. M. Williams, D. Y. Kim, L. Li, S. Balasubramanian, J. Kumar, and S. Tripathy, "Photoinduced surface deformations on azobenzene polymer films," *Journal of Applied Physics*, vol. 86, p. 4498, 1999.

[79] A. Natansohn and P. Rochon, "Photoinduced motions in azo-containing polymers," *Chemical Reviews*, vol. 102, pp. 4139–4175, 2002.

[80] N. Mechau, D. Neher, V. Börger, H. Menzel, and K. Urayama, "Optically driven diffusion and mechanical softening in azobenzene polymer layers," *Applied Physics Letters*, vol. 81, p. 4715, 2002.

[81] M. Saphiannikova, T. M. Geue, O. Henneberg, K. Morawetz, and U. Pietsch, "Linear viscoelastic analysis of formation and relaxation of azobenzene polymer gratings.," *The Journal of chemical physics*, vol. 120, pp. 4039–45, 2004.

[82] N. Mechau, M. Saphiannikova, and D. Neher, "Dielectric and mechanical properties of azobenzene polymer layers under visible and ultraviolet irradiation," *Macromolecules*, vol. 38, pp. 3894–3902, 2005.

[83] K. G. Yager and C. J. Barrett, "Photomechanical Surface Patterning in Azo-Polymer Materials," *Macromolecules*, vol. 39, pp. 9320–9326, 2006.

[84] M. Saphiannikova, V. Toshchevikov, and J. Ilnytskyi, "Photoinduced Deformations in Azobenzene Polymer Films," *Nonlinear Optics and Quantum Optics*, vol. 41, pp. 27–57, 2010.

[85] Y. Yu, M. Nakano, and T. Ikeda, "Photomechanics: directed bending of a polymer film by light.," *Nature*, vol. 425, p. 145, 2003.

[86] M. Yamada, M. Kondo, J.-i. Mamiya, Y. Yu, M. Kinoshita, C. J. Barrett, and T. Ikeda, "Photomobile polymer materials: towards light-driven plastic motors.," *Angewandte Chemie International Edition*, vol. 47, pp. 4986–8, 2008.

[87] M. Yamada, M. Kondo, R. Miyasato, Y. Naka, J.-i. Mamiya, M. Kinoshita, A. Shishido, Y. Yu, C. J. Barrett, and T. Ikeda, "Photomobile polymer materials - various three-dimensional movements," *Journal of Materials Chemistry*, vol. 19, p. 60, 2009.

[88] J.-A. Lv, W. Wang, J. Xu, T. Ikeda, and Y. Yu, "Photoinduced Bending Behavior of Cross-linked Azobenzene Liquid-Crystalline Polymer Films with a Poly(oxyethylene) Backbone.," *Macromolecular Rapid Communications*, vol. 35, pp. 1266–72, 2014.

[89] G. Ragazzon, M. Baroncini, S. Silvi, M. Venturi, and A. Credi, "Light-powered autonomous and directional molecular motion of a dissipative self-assembling system," *Nature Nanotechnology*, vol. 10, pp. 70–75, 2014.

[90] S. Hagen, F. Leyssner, D. Nandi, M. Wolf, and P. Tegeder, "Reversible switching of tetra-tert-butyl-azobenzene on a Au(111) surface induced by light and thermal activation," *Chemical Physics Letters*, vol. 444, pp. 85–90, 2007.

[91] M. Alemani, S. Selvanathan, F. Ample, M. V. Peters, K. H. Rieder, F. Moresco, C. Joachim, S. Hecht, and L. Grill, "Adsorption and switching properties of azobenzene derivatives on different noble metal surfaces: Au(111), Cu(111), and Au(100)," *Journal of Physical Chemistry C*, vol. 112, pp. 10509–10514, 2008.

[92] N. Henningsen, R. Rurali, K. J. Franke, I. Fernández-Torrente, and J. I. Pascual, "Trans to cis isomerization of an azobenzene derivative on a Cu(100) surface," *Applied Physics A: Materials Science and Processing*, vol. 93, pp. 241–246, 2008.

[93] M. Piantek, J. Miguel, A. Krüger, C. Navío, M. Bernien, D. K. Ball, K. Hermann, and W. Kuch, "Temperature, surface, and coverage-induced conformational changes of azobenzene derivatives on Cu(001)," *Journal of Physical Chemistry C*, vol. 113, pp. 20307–20315, 2009.

[94] E. McNellis, J. Meyer, A. Baghi, and K. Reuter, "Stabilizing a molecular switch at solid surfaces: A density functional theory study of azobenzene on Cu(111), Ag(111), and Au(111)," *Physical Review B*, vol. 80, p. 035414, 2009.

[95] F. Leyssner, S. Hagen, L. Óvári, J. Dokić, P. Saalfrank, M. V. Peters, S. Hecht, T. Klamroth, and P. Tegeder, "Photoisomerization ability of molecular switches

adsorbed on Au(111): Comparison between azobenzene and stilbene derivatives," *Journal of Physical Chemistry C*, vol. 114, pp. 1231–1239, 2010.

[96] G. Mercurio, E. R. McNellis, I. Martin, S. Hagen, F. Leyssner, S. Soubatch, J. Meyer, M. Wolf, P. Tegeder, F. S. Tautz, and K. Reuter, "Structure and energetics of azobenzene on Ag(111): Benchmarking semiempirical dispersion correction approaches," *Physical Review Letters*, vol. 104, pp. 1–4, 2010.

[97] R. Schmidt, S. Hagen, D. Brete, R. Carley, C. Gahl, J. Dokić, P. Saalfrank, S. Hecht, P. Tegeder, and M. Weinelt, "On the electronic and geometrical structure of the trans- and cis-isomer of tetra-tert-butyl-azobenzene on Au(111).," *Physical Chemistry Chemical Physics*, vol. 12, pp. 4488–4497, 2010.

[98] J. Mielke, S. Selvanathan, M. Peters, J. Schwarz, S. Hecht, and L. Grill, "Molecules with multiple switching units on a Au(111) surface: self-organization and single-molecule manipulation," *Journal of Physics: Condensed Matter*, vol. 24, p. 394013, 2012.

[99] C. Bronner, M. Schulze, S. Hagen, and P. Tegeder, "The influence of the electronic structure of adsorbate-substrate complexes on photoisomerization ability," *New Journal of Physics*, vol. 14, 2012.

[100] C. Lotze, Y. Luo, M. Corso, K. J. Franke, R. Haag, and J. I. Pascual, "Isomerization Mediated By Intermolecular Interactions," *Journal of Physics: Condensed Matter*, vol. 24, p. 394016, 2012.

[101] G. Floß, G. Granucci, and P. Saalfrank, "Surface hopping dynamics of direct trans-cis photoswitching of an azobenzene derivative in constrained adsorbate geometries," *Journal of Chemical Physics*, vol. 137, 2012.

[102] C. Bronner, B. Priewisch, K. Rück-Braun, and P. Tegeder, "Photoisomerization of an azobenzene on the Bi(111) surface," *Journal of Physical Chemistry C*, vol. 117, pp. 27031–27038, 2013.

[103] C. Bronner and P. Tegeder, "Photo-induced and thermal reactions in thin films of an azobenzene derivative on Bi(111)," *New Journal of Physics*, vol. 16, 2014.

[104] S. D. Evans, S. R. Johnson, H. Ringsdorf, L. M. Williams, and H. Wolf, "Photoswitching of Azobenzene Derivatives Formed on Planar and Colloidal Gold Surfaces," *Langmuir : the ACS journal of surfaces and colloids*, vol. 14, pp. 6436–6440, 1998.

[105] R. Schmidt, E. McNellis, W. Freyer, D. Brete, T. Gieß el, C. Gahl, K. Reuter, and M. Weinelt, "Azobenzene-functionalized alkanethiols in self-assembled monolayers on gold," *Applied Physics A: Materials Science and Processing*, vol. 93, pp. 267–275, 2008.

[106] W. Freyer, D. Brete, R. Schmidt, C. Gahl, R. Carley, and M. Weinelt, "Switching behavior and optical absorbance of azobenzene-functionalized alkanethiols in different environments," *Journal of Photochemistry and Photobiology A: Chemistry*, vol. 204, pp. 102–109, 2009.

[107] E. R. McNellis, G. Mercurio, S. Hagen, F. Leyssner, J. Meyer, S. Soubatch, M. Wolf, K. Reuter, P. Tegeder, and F. S. Tautz, "Bulky spacer groups - A valid strategy to control the coupling of functional molecules to surfaces?," *Chemical Physics Letters*, vol. 499, pp. 247–249, 2010.

[108] E. R. McNellis, C. Bronner, J. Meyer, M. Weinelt, P. Tegeder, and K. Reuter, "Azobenzene versus 3,3',5,5'-tetra-tert-butyl-azobenzene (TBA) at Au(111): characterizing the role of spacer groups.," *Physical Chemistry Chemical Physics*, vol. 12, pp. 6404–6412, 2010.

[109] M. J. Comstock, N. Levy, A. Kirakosian, J. Cho, F. Lauterwasser, J. H. Harvey, D. a. Strubbe, J. M. J. Fréchet, D. Trauner, S. G. Louie, and M. F. Crommie, "Reversible photomechanical switching of individual engineered molecules at a metallic surface," *Physical Review Letters*, vol. 99, pp. 1–4, 2007.

[110] M. Wolf and P. Tegeder, "Reversible molecular switching at a metal surface: A case study of tetra-tert-butyl-azobenzene on Au(111)," *Surface Science*, vol. 603, pp. 1506–1517, 2009.

[111] D. Bléger, A. Ciesielski, P. Samorì, and S. Hecht, "Photoswitching vertically oriented azobenzene self-assembled monolayers at the solid-liquid interface," *Chemistry - A European Journal*, vol. 16, pp. 14256–14260, 2010.

[112] B. Baisch, D. Raffa, U. Jung, O. M. Magnussen, C. Nicolas, J. Lacour, J. Kubitschke, and R. Herges, "Mounting freestanding molecular functions onto surfaces: The platform approach," *Journal of the American Chemical Society*, vol. 131, pp. 442–443, 2009.

[113] U. Jung, C. Schütt, O. Filinova, J. Kubitschke, R. Herges, and O. Magnussen, "Photoswitching of azobenzene-functionalized molecular platforms on Au surfaces," *Journal of Physical Chemistry C*, vol. 116, pp. 25943–25948, 2012.

[114] U. Jung, J. Kubitschke, R. Herges, and O. Magnussen, "Studies of the molecular switching of azobenzene-functionalized platform adlayers on Au(1 1 1) by chronoamperometry," *Electrochimica Acta*, vol. 112, pp. 869–880, 2013.

[115] H. Jacob, S. Ulrich, U. Jung, S. Lemke, T. Rusch, C. Schütt, F. Petersen, T. Strunskus, O. Magnussen, R. Herges, and F. Tuczek, "Monitoring the reversible photoisomerization of an azobenzene-functionalized molecular triazatriangulene platform on Au(111) by IRRAS," *Phys. Chem. Chem. Phys.*, vol. 16, pp. 22643–22650, 2014.

[116] S. Wagner, F. Leyssner, C. Kördel, S. Zarwell, R. Schmidt, M. Weinelt, K. Rück-Braun, M. Wolf, and P. Tegeder, "Reversible photoisomerization of an azobenzene-functionalized self-assembled monolayer probed by sum-frequency generation vibrational spectroscopy.," *Physical Chemistry Chemical Physics*, vol. 11, pp. 6242–6248, 2009.

[117] U. Jung, O. Filinova, S. Kuhn, D. Zargarani, C. Bornholdt, R. Herges, and O. Magnussen, "Photoswitching behavior of azobenzene-containing alkanethiol self-assembled monolayers on Au surfaces.," *Langmuir : the ACS journal of surfaces and colloids*, vol. 26, pp. 13913–23, 2010.

[118] D. Brete, D. Przyrembel, C. Eickhoff, R. Carley, W. Freyer, K. Reuter, C. Gahl, and M. Weinelt, "Mixed self-assembled monolayers of azobenzene photoswitches with trifluoromethyl and cyano end groups.," *Journal of physics. Condensed matter*, vol. 24, p. 394015, 2012.

[119] T. Moldt, D. Brete, D. Przyrembel, S. Das, J. R. Goldman, P. K. Kundu, C. Gahl, R. Klajn, and M. Weinelt, "Tailoring the Properties of Surface-Immobilized Azobenzenes by Monolayer Dilution and Surface Curvature," *Langmuir*, vol. 31, pp. 1048–1057, 2015.

[120] R. Klajn, "Immobilized azobenzenes for the construction of photoresponsive materials," *Pure and Applied Chemistry*, vol. 82, pp. 2247–2279, 2010.

[121] Z. Yu, S. Weidner, T. Risse, and S. Hecht, "The role of statistics and microenvironment for the photoresponse in multi-switch architectures: The case of photoswitchable oligoazobenzene foldamers," *Chemical Science*, vol. 4, p. 4156, 2013.

[122] G. Floß and P. Saalfrank, "The Photoinduced E-Z Isomerization of Bisazobenzenes: A Surface Hopping Molecular Dynamics Study," *The Journal of Physical Chemistry A*, vol. 119, pp. 5026–5037, 2015.

[123] T. Hugel, N. B. Holland, A. Cattani, L. Moroder, M. Seitz, and H. E. Gaub, "Single-molecule optomechanical cycle.," *Science*, vol. 296, pp. 1103–6, 2002.

[124] N. B. Holland, T. Hugel, G. Neuert, A. Cattani-Scholz, C. Renner, D. Oesterhelt, L. Moroder, M. Seitz, and H. E. Gaub, "Single Molecule Force Spectroscopy of Azobenzene Polymers:Âă Switching Elasticity of Single Photochromic Macromolecules," *Macromolecules*, vol. 36, pp. 2015–2023, 2003.

[125] G. Neuert, T. Hugel, R. R. Netz, and H. E. Gaub, "Elasticity of poly(azobenzene-peptides)," *Macromolecules*, vol. 39, pp. 789–797, 2006.

[126] D. Bléger, J. Dokić, M. V. Peters, L. Grubert, P. Saalfrank, and S. Hecht, "Electronic decoupling approach to quantitative photoswitching in linear multiazobenzene architectures.," *The journal of physical chemistry. B*, vol. 115, pp. 9930–40, 2011.

[127] D. Bléger, T. Liebig, R. Thiermann, M. Maskos, J. P. Rabe, and S. Hecht, "Light-orchestrated macromolecular "accordions": reversible photoinduced shrinking of rigid-rod polymers.," *Angewandte Chemie International Edition*, vol. 50, pp. 12559–63, 2011.

[128] D. Bléger, Z. Yu, and S. Hecht, "Toward optomechanics: maximizing the photodeformation of individual molecules.," *Chemical communications*, vol. 47, pp. 12260–6, 2011.

[129] G. Ungar, "Structure of Rotator Phases in n-Alkanes," *The Journal of Physical Chemistry*, vol. 197, pp. 689–695, 1983.

[130] N. Wentzel and S. T. Milner, "Crystal and rotator phases of n-alkanes: A molecular dynamics study.," *The Journal of chemical physics*, vol. 132, p. 044901, 2010.

[131] F. Tao and S. L. Bernasek, "Understanding odd-even effects in organic self-assembled monolayers.," *Chemical reviews*, vol. 107, pp. 1408–53, 2007.

[132] M. Atkinson and M. Richardson, "Phase Behaviour of n-Alkanes and Polyethylene," *Transactions of the Faraday Society*, vol. 65, pp. 1749–1763, 1968.

[133] M. Beiner and H. Huth, "Nanophase separation and hindered glass transition in side-chain polymers.," *Nature materials*, vol. 2, pp. 595–9, 2003.

[134] R. Kline, M. McGehee, E. Kadnikova, J. Liu, and J. Fréchet, "Controlling the Field-Effect Mobility of Regioregular Polythiophene by Changing the Molecular Weight," *Advanced Materials*, vol. 15, pp. 1519–1522, 2003.

[135] P. Keg, A. Lohani, D. Fichou, Y. M. Lam, Y. Wu, B. S. Ong, and S. G. Mhaisalkar, "Direct Observation of Alkyl Chain Interdigitation in Conjugated Polyquarterthiophene Self-Organized on Graphite Surfaces," *Macromolecular Rapid Communications*, vol. 29, pp. 1197–1202, 2008.

[136] H. N. Tsao and K. Müllen, "Improving polymer transistor performance via morphology control.," *Chemical Society reviews*, vol. 39, pp. 2372–86, 2010.

[137] V. Alsten, S. Langmuir, and D. L. Dorset, "Chain Length and the Cosolubility of n-Paraffins in the Solid State," *Macromolecules*, vol. 23, pp. 623–633, 1990.

[138] P. Fenter, P. Eisenberger, and K. S. Liang, "Chain-Length Dependence of the Structures and Phases of CH3(CH2)n-1SH Self-Assembled on Au(111)," *Physical Review Letters*, vol. 70, pp. 2447–2450, 1993.

[139] S. R. Craig, G. P. Hastie, K. J. Roberts, and J. N. Sherwood, "Investigation into the structures of some normal alkanes within the homologous series C13H28 to C60H122 using high-resolution synchrotron X-ray powder diffraction," *Journal of Materials Chemistry*, vol. 4, p. 977, 1994.

[140] N. Camillone III, T. Y. B. Leung, P. Schwartz, P. Eisenberger, and G. Scoles, "Chain Length Dependence of the Striped Phases of Alkanethiol Monolayers Self-Assembled on Au (111): An Atomic Beam Diffraction Study," *Langmuir*, vol. 12, pp. 2737–2746, 1996.

[141] T. Ishizaki, N. Saito, L. SunHyung, K. Ishida, and O. Takai, "Study of alkyl organic monolayers with different molecular chain lengths directly attached to silicon.," *Langmuir : the ACS journal of surfaces and colloids*, vol. 22, pp. 9962–6, 2006.

[142] S. Pechook and B. Pokroy, "Bioinspired hierarchical superhydrophobic structures formed by n-paraffin waxes of varying chain lengths," *Soft Matter*, vol. 9, p. 5710, 2013.

[143] J. Min, Y. N. Luponosov, N. Gasparini, M. Richter, A. V. Bakirov, M. A. Shcherbina, S. N. Chvalun, L. Grodd, S. Grigorian, T. Ameri, S. A. Ponomarenko, and C. J. Brabec, "Effects of Alkyl Terminal Chains on Morphology, Charge Generation, Transport, and Recombination Mechanisms in Solution-Processed Small Molecule Bulk Heterojunction Solar Cells," *Advanced Energy Materials*, pp. n/a–n/a, 2015.

[144] D. Fu, J. Li, J. Wei, and J. Guo, "Effects of terminal chain length in hydrogen-bonded chiral switches on phototunable behavior of chiral nematic liquid crystals: helicity inversion and phase transition," *Soft Matter*, vol. 11, pp. 3034–3045, 2015.

[145] W. De Poel, S. Pintea, J. Drnec, F. Carla, R. Felici, P. Mulder, J. A. A. W. Elemans, W. J. P. Van Enckevort, A. E. Rowan, and E. Vlieg, "Muscovite mica: Flatter than a pancake," *Surface Science*, vol. 619, pp. 19–24, 2014.

[146] F. Ostendorf, C. Schmitz, S. Hirth, a. Kühnle, J. J. Kolodziej, and M. Reichling, "How flat is an air-cleaved mica surface?," *Nanotechnology*, vol. 19, p. 305705, 2008.

[147] G. Binnig and C. F. Quate, "Atomic Force Microscope," *Physical Review Letters*, vol. 56, pp. 930–933, 1986.

[148] "Wikipedia." `https://de.wikipedia.org/wiki/Rasterkraftmikroskop`. Accessed: 2015-08-18.

[149] "Wikipedia." `https://en.wikipedia.org/wiki/Synchrotron_light_source` by EPSIM 3D/JF Santarelli, Synchrotron Soleil. Accessed: 2015-08-18.

[150] J. Als-Nielsen and D. McMorrow, *Elements of Modern X-ray Physics: Second Edition*. New York: Wiley, 2011.

[151] L. G. Parratt, "Surface Studies of Solids by Total Reflection of X-Rays," *Physical Review*, vol. 95, pp. 359–369, 1954.

[152] P. R. Willmott, D. Meister, S. J. Leake, M. Lange, A. Bergamaschi, M. Böge, M. Calvi, C. Cancellieri, N. Casati, A. Cervellino, Q. Chen, C. David, U. Flechsig, F. Gozzo, B. Henrich, S. Jäggi-Spielmann, B. Jakob, I. Kalichava, P. Karvinen, J. Krempasky, A. Lüdeke, R. Lüscher, S. Maag, C. Quitmann, M. L. Reinle-Schmitt, T. Schmidt, B. Schmitt, A. Streun, I. Vartiainen, M. Vitins, X. Wang, and R. Wullschleger, "The Materials Science beamline upgrade at the Swiss Light Source.," *Journal of synchrotron radiation*, vol. 20, pp. 667–82, 2013.

[153] J. McIntyre and D. Aspnes, "Differential reflection spectroscopy of very thin surface films," *Surface Science*, vol. 24, pp. 417–434, 1971.

[154] G. Paasch, "J. Lekner. Theory of reflection of electromagnetic and particle waves. Developments in Electromagnetic Theory and Application; 3. Martinus Nijhoff Publishers, Dordrecht/Boston/Lancaster, 1987, 279 S. Dfl. 175.00, US $ 78.50, ISBN 90-247-3418-5," *Crystal Research and Technology*, vol. 22, pp. 1536–1536, 1987.

[155] C. Hilsum, "Flat-panel electronic displays: a triumph of physics, chemistry and engineering.," *Philosophical transactions. Series A, Mathematical, physical, and engineering sciences*, vol. 368, pp. 1027–1082, 2010.

[156] C. J. Lawrence, "The mechanics of spin coating of polymer films," *Physics of Fluids*, vol. 31, p. 2786, 1988.

[157] D. B. Hall, P. Underhill, and J. M. Torkelson, "Spin Coating of Thin and Ultrathin Polymer Films," *Polymer Engineering and Science*, vol. 38, pp. 2039–2045, 1998.

[158] A. P. Bisson, F. J. Carver, C. A. Hunter, and J. P. Waltho, "Molecular Zippers," *Journal of the American Chemical Society*, vol. 116, pp. 10292–10293, 1994.

[159] R. Bhosale, A. Perez-Velasco, V. Ravikumar, R. S. K. Kishore, O. Kel, A. Gomez-Casado, P. Jonkheijm, J. Huskens, P. Maroni, M. Borkovec, T. Sawada, E. Vauthey, N. Sakai, and S. Matile, "Topologically matching supramolecular n/p-heterojunction architectures.," *Angewandte Chemie International Edition*, vol. 48, pp. 6461–4, 2009.

[160] H. Finkelmann, E. Nishikawa, G. Pereira, and M. Warner, "A New Opto-Mechanical Effect in Solids," *Physical Review Letters*, vol. 87, p. 015501, 2001.

[161] V. V. Tsukruk, I. Luzinov, K. Larson, S. Li, and D. V. Mcgrath, "Intralayer reorganization of photochromic molecular films," *Journal of Materials Science Letters*, vol. 20, pp. 873–876, 2001.

[162] D. M. Junge and D. V. McGrath, "Photoresponsive Azobenzene-Containing Dendrimers with Multiple Discrete States," *Journal of the American Chemical Society*, vol. 121, pp. 4912–4913, 1999.

[163] Y. Zhao and T. Ikeda, eds., *Smart Light-Responsive Materials*. Hoboken, NJ, USA: John Wiley & Sons, Inc., 2009.

[164] K. G. Yager and C. J. Barrett, "Novel photo-switching using azobenzene functional materials," *Journal of Photochemistry and Photobiology A: Chemistry*, vol. 182, pp. 250–261, 2006.

[165] H.-K. Kim, X.-S. Wang, Y. Fujita, A. Sudo, H. Nishida, M. Fujii, and T. Endo, "Photomechanical Switching Behavior of Semi-Interpenetrating Polymer Network Consisting of Azobenzene-Carrying Crosslinked Poly(vinyl ether) and Polycarbonate," *Macromolecular Rapid Communications*, vol. 26, pp. 1032–1036, 2005.

[166] P. Karageorgiev, D. Neher, B. Schulz, B. Stiller, U. Pietsch, M. Giersig, and L. Brehmer, "From anisotropic photo-fluidity towards nanomanipulation in the optical near-field.," *Nature materials*, vol. 4, pp. 699–703, 2005.

[167] N. Lomadze, A. Kopyshev, J. Rühe, and S. Santer, "Light-Induced Chain Scission in Photosensitive Polymer Brushes," *Macromolecules*, vol. 44, pp. 7372–7377, 2011.

[168] T. Ikeda and T. Ube, "Photomobile polymer materials: from nano to macro," *Materials Today*, vol. 14, pp. 480–487, 2011.

[169] M. Irie, Y. Hirano, S. Hashimoto, and K. Hayashi, "Photoresponsive polymers. 2. Reversible solution viscosity change of polyamides having azobenzene residues in the main chain," *Macromolecules*, vol. 14, pp. 262–267, 1981.

[170] M. Irie and W. Schnabel, "Photoresponsive polymers. Dynamics of conformational changes of polyamides with backbone azobenzene groups," *Macromolecules*, vol. 14, pp. 1246–1249, 1981.

[171] B. Sapich, A. B. E. Vix, J. P. Rabe, and J. Stumpe, "Photoinduced Self-Organization and Photoorientation of a LC Main-Chain Polyester Containing Azobenzene Moieties," *Macromolecules*, vol. 38, pp. 10480–10486, 2005.

[172] N. Hosono, M. Yoshikawa, H. Furukawa, K. Totani, K. Yamada, T. Watanabe, and K. Horie, "Photoinduced Deformation of Rigid Azobenzene-Containing Polymer Networks," *Macromolecules*, vol. 46, pp. 1017–1026, 2013.

[173] M. R. Shankar, M. L. Smith, V. P. Tondiglia, K. M. Lee, M. E. McConney, D. H. Wang, L.-S. Tan, and T. J. White, "Contactless, photoinitiated snap-through in azobenzene-functionalized polymers.," *Proceedings of the National Academy of Sciences of the United States of America*, vol. 110, pp. 18792–7, 2013.

[174] D. H. Wang, J. J. Wie, K. M. Lee, T. J. White, and L.-S. Tan, "Impact of Backbone Rigidity on the Photomechanical Response of Glassy, Azobenzene-Functionalized Polyimides," *Macromolecules*, vol. 47, pp. 659–667, 2014.

[175] J. J. Wie, D. H. Wang, K. M. Lee, L.-S. Tan, and T. J. White, "Molecular Engineering of Azobenzene-Functionalized Polyimides To Enhance Both Photomechanical Work and Motion," *Chemistry of Materials*, vol. 26, pp. 5223–5230, 2014.

[176] D. Bléger, T. Liebig, R. Thiermann, M. Maskos, J. P. Rabe, and S. Hecht, "Light-orchestrated macromolecular "accordions": reversible photoinduced shrinking of rigid-rod polymers.," *Angewandte Chemie International Edition*, vol. 50, pp. 12559–63, 2011.

[177] C.-l. Lee, T. Liebig, S. Hecht, D. Bléger, and J. P. Rabe, "Light-Induced Contraction and Extension of Single Macromolecules on a Modified Graphite Surface.," *ACS nano*, pp. 0–6, 2014.

[178] M. Hoshino, E. Uchida, Y. Norikane, R. Azumi, S. Nozawa, A. Tomita, T. Sato, S.-i. Adachi, and S.-y. Koshihara, "Crystal melting by light: X-ray crystal structure analysis of an azo crystal showing photoinduced crystal-melt transition.," *Journal of the American Chemical Society*, vol. 136, pp. 9158–64, 2014.

[179] D. de Loera, A. Stopin, and M. A. Garcia-Garibay, "Photoinduced and thermal denitrogenation of bulky triazoline crystals: insights into solid-to-solid transformation.," *Journal of the American Chemical Society*, vol. 135, pp. 6626–32, 2013.

[180] H. Koshima, N. Ojima, and H. Uchimoto, "Mechanical motion of azobenzene crystals upon photoirradiation.," *Journal of the American Chemical Society*, vol. 131, pp. 6890–1, 2009.

[181] M. Ballauff, "Stiff-Chain Polymers-Structure, Phase Behavior, and Properties," *Angewandte Chemie International Edition in English*, vol. 28, pp. 253–267, 1989.

[182] J.-P. Gorce, S. J. Spells, X.-b. Zeng, and G. Ungar, "Infrared Active Methyl Group Vibrations in Tetratetracontane: A Probe for Chain End Organization and Crystal Structure," *The Journal of Physical Chemistry B*, vol. 108, pp. 3130–3139, 2004.

[183] C. Weber, C. Frank, S. Bommel, T. Rukat, W. Leitenberger, P. Schäfer, F. Schreiber, and S. Kowarik, "Chain-length dependent growth dynamics of n-alkanes on silica investigated by energy-dispersive x-ray reflectivity in situ and in real-time.," *The Journal of chemical physics*, vol. 136, p. 204709, 2012.

[184] R. J. Kline, D. M. DeLongchamp, D. A. Fischer, E. K. Lin, L. J. Richter, M. L. Chabinyc, M. F. Toney, M. Heeney, and I. McCulloch, "Critical Role of Side-Chain Attachment Density on the Order and Device Performance of Polythiophenes," *Macromolecules*, vol. 40, pp. 7960–7965, 2007.

[185] M. Ballauff, *Integration of Fundamental Polymer Science and Technology.* Dordrecht: Springer Netherlands, 1988.

[186] P. Rochon, E. Batalla, and A. Natansohn, "Optically induced surface gratings on azoaromatic polymer films," *Applied Physics Letters*, vol. 66, p. 136, 1995.

[187] O. M. Tanchak and C. J. Barrett, "Light-Induced Reversible Volume Changes in Thin Films of Azo Polymers: The Photomechanical Effect," *Macromolecules*, vol. 38, pp. 10566–10570, 2005.

[188] D. Lippits, S. Rastogi, and G. Höhne, "Melting Kinetics in Polymers," *Physical Review Letters*, vol. 96, p. 218303, 2006.

[189] F. J. Meyer zu Heringdorf, M. C. Reuter, and R. M. Tromp, "Growth dynamics of pentacene thin films.," *Nature*, vol. 412, pp. 517–20, 2001.

[190] S. Kowarik, A. Gerlach, S. Sellner, F. Schreiber, L. Cavalcanti, and O. Konovalov, "Real-Time Observation of Structural and Orientational Transitions during Growth of Organic Thin Films," *Physical Review Letters*, vol. 96, p. 125504, 2006.

[191] F. Schreiber, "Organic molecular beam deposition: Growth studies beyond the first monolayer," *Physica Status Solidi (a)*, vol. 201, pp. 1037–1054, 2004.

[192] H. Koshima, K. Takechi, H. Uchimoto, M. Shiro, and D. Hashizume, "Photomechanical bending of salicylideneaniline crystals.," *Chemical communications*, vol. 47, pp. 11423–5, 2011.

[193] H. Koshima, H. Nakaya, H. Uchimoto, and N. Ojima, "Photomechanical Motion of Furylfulgide Crystals," *Chemistry Letters*, vol. 41, pp. 107–109, 2012.

[194] H. Koshima and N. Ojima, "Photomechanical bending of 4-aminoazobenzene crystals," *Dyes and Pigments*, vol. 92, pp. 798–801, 2012.

[195] S. Ohshima, M. Morimoto, and M. Irie, "Light-driven bending of diarylethene mixed crystals," *Chem. Sci.*, vol. 00, pp. 1–7, 2015.

[196] E. Uchida, R. Azumi, and Y. Norikane, "Light-induced crawling of crystals on a glass surface," *Nature Communications*, vol. 6, p. 7310, 2015.

[197] O. S. Bushuyev, T. A. Singleton, and C. J. Barrett, "Fast, reversible, and general photomechanical motion in single crystals of various azo compounds using visible light.," *Advanced materials*, vol. 25, pp. 1796–800, 2013.

[198] O. S. Bushuyev, A. Tomberg, T. Fris, and C. J. Barrett, "Shaping Crystals with Light: Crystal-to-Crystal Isomerization and Photomechanical Effect in Fluorinated Azobenzenes," *Journal of the American Chemical Society*, vol. 135, pp. 12556–12559, 2013.

[199] E. R. Kay, D. a. Leigh, and F. Zerbetto, *Synthetic molecular motors and mechanical machines*, vol. 46. Wiley-VCH Verlag GmbH & Co. KGaA, 2007.

[200] R. Kopelman, "Racing with nature: Artificial nanomachines that keep running on light, both left and right," *ACS Nano*, vol. 6, pp. 7553–7555, 2012.

[201] M. Natali and S. Giordani, "Molecular switches as photocontrollable "smart" receptors," *Chemical Society Reviews*, vol. 41, p. 4010, 2012.

[202] T. J. Kucharski, Y. Tian, S. Akbulatov, and R. Boulatov, "Chemical solutions for the closed-cycle storage of solar energy," *Energy & Environmental Science*, vol. 4, p. 4449, 2011.

[203] B. K. Pathem, S. A. Claridge, Y. B. Zheng, and P. S. Weiss, "Molecular Switches and Motors on Surfaces," *Annual Review of Physical Chemistry*, vol. 64, pp. 605–630, 2013.

[204] E. Jahnke, N. Severin, P. Kreutzkamp, J. P. Rabe, and H. Frauenrath, "Molecular level control over hierarchical structure formation and polymerization of oligopeptide-polymer conjugates," *Advanced Materials*, vol. 20, pp. 409–414, 2008.

[205] U. Lauter, W. Meyer, and G. Wegner, "Molecular composites from rigid-rod poly (p-phenylene) s with oligo (oxyethylene) side chains as novel polymer electrolytes," *Macromolecules*, vol. 9297, pp. 2092–2101, 1997.

[206] G. F. Burkhard, E. T. Hoke, and M. D. McGehee, "Accounting for interference, scattering, and electrode absorption to make accurate internal quantum efficiency measurements in organic and other thin solar cells," *Advanced Materials*, vol. 22, pp. 3293–3297, 2010.

[207] C. Weber, T. Liebig, M. Gensler, L. Pithan, S. Bommel, D. Bléger, J. P. Rabe, S. Hecht, and S. Kowarik, "Light-Controlled 'Molecular Zippers' Based on Azobenzene Main Chain Polymers," *Macromolecules*, vol. 48, pp. 1531–1537, 2015.

[208] D. Gegiou, K. A. Muszkat, and E. Fischer, "Temperature dependence of photoisomerization. V. Effect of substituents on the photoisomerization of stilbenes and azobenzenes," *Journal of the American Chemical Society*, vol. 90, pp. 3907–3918, 1968.

[209] D. Gegiou, K. A. Muszkat, and E. Fischer, "Temperature dependence of photoisomerization. VI. Viscosity effect," *Journal of the American Chemical Society*, vol. 90, pp. 12–18, 1968.

[210] Q.-Z. Yang, Z. Huang, T. J. Kucharski, D. Khvostichenko, J. Chen, and R. Boulatov, "A molecular force probe.," *Nature nanotechnology*, vol. 4, pp. 302–306, 2009.

[211] N. Tamaoki, K. Koseki, and T. Yamaoka, "[2.2](4,4')Azobenzenophane," *Angewandte Chemie International Edition*, vol. 29, pp. 105–106, 1990.

[212] R. Turanský, M. Konôpka, N. L. Doltsinis, I. Stich, and D. Marx, "Switching of functionalized azobenzene suspended between gold tips by mechanochemical, photochemical, and opto-mechanical means.," *Physical Chemistry Chemical Physics*, vol. 12, pp. 13922–13932, 2010.

[213] R. Turanský, M. Konôpka, N. L. Doltsinis, I. Štich, and D. Marx, "Optical, mechanical, and opto-mechanical switching of anchored dithioazobenzene bridges," *ChemPhysChem*, vol. 11, pp. 345–348, 2010.

[214] S. Serra, S. Iarlori, E. Tosatti, S. Scandolo, and G. Santoro, "Dynamical and thermal properties of polyethylene by ab initio simulation," *Chemical Physics Letters*, vol. 331, pp. 339–345, 2000.

[215] K. Rück-Braun, M. A. Petersen, F. Michalik, A. Hebert, D. Przyrembel, C. Weber, S. a. Ahmed, S. Kowarik, and M. Weinelt, "Formation of carboxy- and amide-terminated alkyl monolayers on Silicon(111) investigated by ATR-FTIR, XPS, and X-ray scattering: construction of photoswitchable surfaces.," *Langmuir : the ACS journal of surfaces and colloids*, vol. 29, pp. 11758–69, 2013.

[216] A. Opitz, M. Horlet, M. Kiwull, J. Wagner, M. Kraus, and W. Brütting, "Bipolar charge transport in organic field-effect transistors: Enabling high mobilities and transport of photo-generated charge carriers by a molecular passivation layer," *Organic Electronics: physics, materials, applications*, vol. 13, pp. 1614–1622, 2012.

[217] N. G. Almarza, E. Enciso, and F. J. Bermejo, "Monte Carlo simulation of liquid n-alkanes. I. Intramolecular structure and thermodynamics," *The Journal of Chemical Physics*, vol. 96, pp. 4625–32, 1992.

[218] M. Mondello, G. S. Grest, E. B. Webb, and P. Peczak, "Dynamics of n-alkanes: Comparison to Rouse model," *The Journal of Chemical Physics*, vol. 109, pp. 798–805, 1998.

[219] R. L. Schwoebel and E. J. Shipsey, "Step Motion on Crystal Surfaces," *Journal of Applied Physics*, vol. 37, pp. 3682–3686, 1966.

[220] G. Hlawacek, P. Puschnig, P. Frank, A. Winkler, C. Ambrosch-Draxl, and C. Teichert, "Characterization of step-edge barriers in organic thin-film growth.," *Science (New York, N.Y.)*, vol. 321, pp. 108–11, 2008.

[221] J. E. Goose, E. L. First, and P. Clancy, "Nature of step-edge barriers for small organic molecules," *Physical Review B*, vol. 81, pp. 10–12, 2010.

[222] B. Krause, A. C. Dürr, F. Schreiber, H. Dosch, and O. H. Seeck, "Thermal stability and partial dewetting of crystalline organic thin films: 3,4,9,10-perylenetetracarboxylic dianhydride on Ag(111)," *The Journal of Chemical Physics*, vol. 119, pp. 3429–35, 2003.

[223] H. Proehl, R. Nitsche, T. Dienel, K. Leo, and T. Fritz, "In situ differential reflectance spectroscopy of thin crystalline films of PTCDA on different substrates," *Physical Review B*, vol. 71, pp. 1–14, 2005.

[224] U. Heinemeyer, K. Broch, A. Hinderhofer, M. Kytka, R. Scholz, A. Gerlach, and F. Schreiber, "Real-Time Changes in the Optical Spectrum of Organic Semiconducting Films and Their Thickness Regimes during Growth," *Physical Review Letters*, vol. 104, pp. 1–4, 2010.

[225] T. Hosokai, A. Gerlach, A. Hinderhofer, C. Frank, G. Ligorio, U. Heinemeyer, A. Vorobiev, and F. Schreiber, "Simultaneous in situ measurements of x-ray reflectivity and optical spectroscopy during organic semiconductor thin film growth," *Applied Physics Letters*, vol. 97, p. 063301, 2010.

[226] M. Hanke, V. M. Kaganer, O. Bierwagen, M. Niehle, and A. Trampert, "Delayed crystallization of ultrathin Gd2O3 layers on Si(111) observed by in situ X-ray diffraction.," *Nanoscale research letters*, vol. 7, p. 203, 2012.

[227] S. Kowarik, A. Gerlach, M. W. Skoda, S. Sellner, and F. Schreiber, "Real-time studies of thin film growth: Measurement and analysis of X-ray growth oscillations beyond the anti-Bragg point," *The European Physical Journal Special Topics*, vol. 167, pp. 11–18, 2009.

[228] B. Macdonald, R. Cole, and V. Koutsos, "The formation of dewetting structures after evaporation of n-dodecane on graphite studied by atomic force microscopy," *Surface Science*, vol. 548, pp. 41–50, 2004.

[229] S. Kowarik, A. Gerlach, and F. Schreiber, "Organic Molecular Beam Deposition : Fundamentals , Growth Dynamics , and In-Situ Studies," *Journal of physics. Condensed matter*, vol. 20, p. 184005, 2008.

[230] W. Huang, B. Li, and J. Zuo, "Diffusion-limited submonolayer pentacene thin film growth on hydrogen-passivated Si(111) substrates," *Surface Science*, vol. 595, pp. 157–164, 2005.

[231] S. Kowarik, A. Gerlach, A. Hinderhofer, S. Milita, F. Borgatti, F. Zontone, T. Suzuki, F. Biscarini, and F. Schreiber, "Structure, morphology, and growth dynamics of perfluoro-pentacene thin films," *physica status solidi (RRL) - Rapid Research Letters*, vol. 2, pp. 120–122, 2008.

[232] K. A. Ritley, B. Krause, F. Schreiber, and H. Dosch, "A portable ultrahigh vacuum organic molecular beam deposition system for in situ x-ray diffraction measurements," *Review of Scientific Instruments*, vol. 72, pp. 1453–1457, 2001.

[233] F. Neissendorfer, U. Pietsch, and G. Brezesinski, "The energy-dispersive reflectometer / diffractometer at BESSY-I," *Measurement Science and Technology*, vol. 10, pp. 354–361, 1999.

[234] U. Pietsch, J. Grenzer, T. Geue, F. Neissendorfer, G. Brezsesinski, C. Symietz, H. Möhwald, and W. Gudat, "The energy-dispersive reflectometer at BESSY II: a challenge for thin film analysis," *Nuclear Instruments and Methods in Physics Research Section A: Accelerators, Spectrometers, Detectors and Associated Equipment*, vol. 467-468, pp. 1077–1080, 2001.

[235] S. Kowarik, A. Gerlach, W. Leitenberger, J. Hu, G. Witte, C. Wöll, U. Pietsch, and F. Schreiber, "Energy-dispersive X-ray reflectivity and GID for real-time growth studies of pentacene thin films," *Thin Solid Films*, vol. 515, pp. 5606–5610, 2007.

[236] P. W. Teare, "The crystal structure of orthorhombic hexatriacontane, C 36 H 74," *Acta Crystallographica*, vol. 12, pp. 294–300, 1959.

[237] K. Nozaki, R. Saihara, K. Ishikawa, and T. Yamamoto, "Structure of Normal Alkane Evaporated Films : Molecular Orientation," *Japanese Journal of Applied Physics Part 1*, vol. 46, pp. 761–769, 2007.

[238] T. Yamamoto, K. Nozaki, A. Yamaguchi, and N. Urakami, "Molecular simulation of crystallization in n-alkane ultrathin films: effects of film thickness and substrate attraction.," *The Journal of chemical physics*, vol. 127, p. 154704, 2007.

[239] B. Krause, F. Schreiber, H. Dosch, A. Pimpinelli, and O. H. Seeck, "Temperature dependence of the 2D-3D transition in the growth of PTCDA on Ag(111): A real-time X-ray and kinetic Monte Carlo study," *Europhysics Letters (EPL)*, vol. 65, pp. 372–378, 2004.

[240] A. Hinderhofer, A. Gerlach, S. Kowarik, F. Zontone, J. Krug, and F. Schreiber, "Smoothing and coherent structure formation in organic-organic heterostructure growth," *Europhysics Letters (EPL)*, vol. 91, p. 56002, 2010.

[241] A. Gerlach, S. Sellner, S. Kowarik, and F. Schreiber, "In-situ X-ray scattering studies of OFET interfaces," *Physica Status Solidi (a)*, vol. 205, pp. 461–474, 2008.

[242] A. Mayer, R. Ruiz, H. Zhou, R. Headrick, A. Kazimirov, and G. Malliaras, "Growth dynamics of pentacene thin films: Real-time synchrotron x-ray scattering study," *Physical Review B*, vol. 73, pp. 1–5, 2006.

[243] P. Cohen, G. Petrich, P. Pukite, and G. Whaley, "BIRTH-DEATH MODELS OF EPITAXY," *Surface Science*, vol. 216, pp. 222–248, 1989.

[244] W. Braun, B. Jenichen, V. M. Kaganer, A. G. Shtukenberg, L. Däweritz, and K. H. Ploog, "Layer-by-layer growth of GaAs(001) studied by in situ synchrotron X-ray diffraction," *Surface Science*, vol. 525, pp. 126–136, 2003.

[245] V. I. Trofimov, V. G. Mokerov, and A. G. Shumyankov, "Kinetic model for molecular beam epitaxial growth on a singular surface," *Thin Solid Films*, vol. 306, pp. 105–111, 1997.

[246] V. I. Trofimov and V. G. Mokerov, "barrier : comparative analysis of different models," *Materials Science and Engineering B*, vol. 89, pp. 420–425, 2002.

[247] V. I. Trofimov, "Morphology evolution in a growing film," *Thin Solid Films*, vol. 428, pp. 56–65, 2003.

[248] A. R. Woll, T. V. Desai, and J. R. Engstrom, "Quantitative modeling of in situ x-ray reflectivity during organic molecule hin film growth," *Physical Review B*, vol. 84, pp. 1–16, 2011.

[249] A. Amassian, T. Desai, S. Kowarik, S. Hong, A. Woll, G. Malliaras, F. Schreiber, and J. Engstrom, "Coverage dependent adsorption dynamics in hyperthermal organic thin film growth.," *The Journal of Chemical Physics*, vol. 130, p. 124701, 2009.

[250] G. Ehrlich and F. G. Hudda, "Atomic View of Surface Self-Diffusion: Tungsten on Tungsten," *The Journal of Chemical Physics*, vol. 44, pp. 1039–49, 1966.

[251] R. L. Schwoebel, "Step Motion on Crystal Surfaces. II," *Journal of Applied Physics*, vol. 40, p. 614, 1969.

Acknowledgment

This thesis would not have been possible without the help of many people, whom I would like to thank for their kind support. First and foremost, I would like to thank my supervisor, **Prof. Stefan Kowarik**, for his trust in me and for his support throughout the years. Next, I want to thank **Prof. Stefan Hecht** and **Dr. David Bléger** for their invaluable help during my thesis. Without their amazing skills in organic synthesis and their extensive knowledge about molecular switches and azobenzene in particular this thesis would not have been possible. A large part of this work would also not have been possible without the support of **Prof. Jürgen P. Rabe**, who introduced me into polymer science and AFM. In addition to that I also want to thank **Tobias Liebig** and **Manuel Gensler** who were extremely kind and helpful during my polymer projects. Next, I would like to thank several people from the SFB 658 with whom to collaborate was a great honor and pleasure. I owe a lot to **Prof. Martin Weinelt**, who helped to integrate our project into the SFB 658. Also also would like to thank **Dr. Cornelius Gahl**, **Daniel Brete**, **Daniel Przyrembel** and **Thomas Moldt** from the AG Weinelt for introducing me into the field of molecular switches and for all their support. I am also very grateful to the people from the AG Rück-Braun, **Prof. Karola Rück-Braun**, **Dr. Michael Åxman Petersen**, **Dr. Andreas Hebert** and **Christoph Barta**, who prepared excellent SAMs. I also want to thank **Dr. Peter Schäfer** for his invaluable technical support, and **Prof. Marcus Mezger** and **Dr. Binyang Hou** for giving me the opportunity to perform experiments at the high-energy x-ray diffraction beamline ID15 at ESRF. Furthermore, I would like to thank **Prof. Frank Schreiber** for giving me the opportunity to perform my first big research project at BESSY II and **Dr. Christian Frank** for helping me survive my very first synchrotron beamtime. Last but not least I want to thank my colleagues from the AG Kowarik for their great support and for being the best team one could wish for. In particular, I want to thank **Dr. Sebastian Bommel**, **Anton Zykov** and **Linus Pithan** with whom i shared offices, cars, overcrowded hotel rooms and many control hutches.

Hilfsmittel

- ChemSketch
- Gwyddion 2.3
- ImageJ
- Irfanview 4.3
- Matlab R2008a
- Mendeley
- Mercury 3.3
- Microsoft Powerpoint 2013
- OriginPro 8.6 und 9
- Parratt32
- TeXnicCenter
- Wolfram Mathematica 9

Selbstständigkeitserklärung

„Ich erkläre eidesstattlich, dass ich die Dissertation selbstständig und nur unter Verwendung der von mir gemäß §7 Abs. 3 der Promotionsordnung der Mathematisch-Naturwissenschaftlichen Fakultät, veröffentlicht im Amtlichen Mitteilungsblatt der Humboldt-Universität zu Berlin Nr. 126/2014 am 18.11.2014 angegebenen Hilfsmittel angefertigt habe. Ich habe mich nicht anderwärts um einem Doktorgrad im Promotionsfach Physik beworben und besitze keinen Doktorgrad im Promotionsfach Physik. Die Promotionsordnung der Mathematisch-Naturwissenschaftlichen Fakultät, veröffentlicht im Amtlichen Mitteilungsblatt der Humboldt-Universität zu Berlin Nr. 126/2014 am 18.11.2014 habe ich zur Kenntnis genommen."

Christopher Weber
December 15, 2015